

In the field of cancer treatment, particle therapy has recently raised the interest of the community due to the high relative biological effectiveness of charged particles. In particular they prove to be more effective for targeting radio resistant or inoperable tumours. Nevertheless different sources of error can worsen the dose delivery profile, such as patient mis positioning, evolution of the tumour/morphology of the patient and imprecision in the treatment plannings, due to fragmentation of the incident beam and range uncertainties. As a consequence a three-dimensional non invasive imaging technique for ion beam therapy monitoring is required. The attention of the community is thus focused on positron emission tomography (PET).

In particular developments in the field of particle detectors push for the use of time of flight information, that allows to improve the sensitivity by improving the signal to noise ratio (SNR). In order to benefit from a significative reduction of the SNR, the target is less than 100 ps FWHM coincidence time resolution for the two detectors. The standard solution for future PET scanners is to make use of heavy scintillating crystals coupled to Silicon PhotoMultipliers.

This thesis is devoted to the full characterization of the parameters that influence time resolution in a scintillator/photodetector setup, with particular attention focused on the impact of time profiles of heavy scintillators on the performance.

The first part of the presented work has the objective of describing the fundamental model that governs light production and collection in a PET-like setup. To this purpose a model based on multi-exponential time profiles has been implemented on an existing framework, widening the scope of usage by evaluating the role of Cerenkov photons produced by low energy radiation.

Moreover in order to properly characterized the operational parameters of a scintillator setup, a comparative analysis of ray tracing softwares has been conducted, namely two packages SLitrani and Geant4. The latter has been chosen to build the simulation framework that allowed to disentangle the various source of resolution degradation.

Finally the work focused on the measurements and evaluation of rise time. Non zero rise time in scintillating systems is given by the different processes characterizing energy deposition inside a crystalline lattice, with utmost relevance of the latest stage of electron hole thermalization. The time scale of this phenomenon is  $\sim 100$  ps and until now has proven to be difficult to estimate due to the intrinsic limitations of detection setups. Samples of different crystalline species such as CeF<sub>3</sub>, LSO:Ce, LuAG:Ce, LuAG:Pr with different doping concentration are the subject of a time resolved analysis. Data taking has been performed in two different conditions: excitation at low energy (36 eV) and a PET-like setup (511 KeV).

The first set of measurements has been performed at the VUV beamline at Celia, Bordeaux, with an excitation energy of 36 eV. The data show results broadly separable in to two main groups: crystals in the LuAG group, with rise times  $>100$  ps, and crystals belonging to the LSO group with rise times  $<50$  ps. This is due to the different energy transfer mechanism.

The samples were then measured with a positron source (<sup>22</sup>Na) on a experimental bench composed by a MCP-PMT stop detector and a tagging crystal readout by an amplified SiPM. Rise time order of magnitude proved to be accessible, though maintaining large uncertainties due to the limited resolution and the long accumulation times. Nonetheless we showed that Cerenkov photons and deep volume excitations introduce a non negligible contribution to the measured rise time. In particular the samples, excited above the Cerenkov threshold and in the deep volume of the crystal due to the energy of the excitation, showed slower rise times, above 100 ps. Moreover the influence of Teflon diffusive wrapping have been investigated, showing that opening the extraction cone of the crystals leads to higher rise times due to coupling of multiple reflection modes.

# Contents

i

<b>List of Figures</b>	<b>ix</b>
<b>1 Motivations</b>	<b>1</b>
1.1 Particle therapy . . . . .	2
1.1.1 Ion beam therapy . . . . .	2
1.1.2 Beam delivery . . . . .	4
1.1.3 Monitoring of the beam . . . . .	5
1.2 Positron Emission Tomography . . . . .	6
1.2.1 Principles . . . . .	6
1.2.2 Image reconstruction . . . . .	8
1.2.3 Sources of noise and sensitivity . . . . .	9
1.2.4 Time-Of-Flight PET . . . . .	11
1.3 Outline of the thesis . . . . .	12
1.3.1 From high energy physics to medical applications . . . . .	12
1.3.2 Study of time profiles . . . . .	13
<b>2 Scintillating detectors</b>	<b>15</b>
2.1 Interaction of radiation with matter . . . . .	15
2.1.1 Photoelectric effect . . . . .	16
2.1.2 Compton scattering . . . . .	17
2.1.3 Pair production . . . . .	17

2.2	The scintillation mechanism . . . . .	19
2.2.1	Creation of electron hole pairs . . . . .	20
2.2.2	Intrinsic luminescence . . . . .	21
2.2.3	Core to valence transitions . . . . .	22
2.2.4	Extrinsic luminescence . . . . .	22
2.2.5	Quenching phenomena . . . . .	23
2.3	Operational parameters . . . . .	23
2.3.1	Light yield . . . . .	23
2.3.2	Optical properties and light transport . . . . .	24
2.3.3	Energy resolution and nonproportionality . . . . .	24
2.3.4	Cerenkov effect . . . . .	25
2.4	Most common scintillation processes . . . . .	28
<b>3</b>	<b>Photo detectors</b>	<b>31</b>
3.1	Photo multiplier tubes . . . . .	32
3.1.1	Properties of PMT . . . . .	32
3.2	Micro Channel Plate-PMT . . . . .	34
3.2.1	Properties of MCP . . . . .	35
3.3	Silicon photo multipliers . . . . .	36
3.3.1	Analog SiPM . . . . .	38
3.3.2	Properties of SiPM . . . . .	38
3.3.3	The NINO chip . . . . .	40
<b>4</b>	<b>A model for scintillation counting</b>	<b>43</b>
4.1	Signal formation . . . . .	43
4.1.1	Scintillation pulse . . . . .	43
4.1.2	Cerenkov pulse . . . . .	44
4.2	The Cramer-Rao lower bound . . . . .	45

4.3	The order statistics . . . . .	48
4.4	Intrinsic time resolution . . . . .	48
4.5	Effects on signal extraction . . . . .	50
<b>5</b>	<b>MonteCarlo simulation tools</b>	<b>53</b>
5.1	Ray tracing . . . . .	53
5.1.1	Rayleigh scattering . . . . .	54
5.1.2	Model for surface interactions . . . . .	54
5.2	Geant4 . . . . .	55
5.2.1	Physics . . . . .	56
5.3	SLitrani . . . . .	57
5.3.1	Physics . . . . .	58
5.4	A comparison for timing simulation . . . . .	59
5.4.1	Cerenkov photons for low energy excitation . . . . .	60
5.4.2	Rise time model . . . . .	63
5.4.3	Absorption and surface treatment . . . . .	64
5.5	Simulation input parameters . . . . .	68
5.5.1	Fluorescence spectrum . . . . .	68
5.5.2	Optical transmission . . . . .	71
5.5.3	Light yield . . . . .	72
<b>6</b>	<b>Methods</b>	<b>77</b>
6.1	Time Correlated Single Photon couting . . . . .	77
6.1.1	Excitation . . . . .	78
6.1.2	Detection . . . . .	80
6.1.3	Stop rate and bias . . . . .	81
6.1.4	Statistics and accumulation times . . . . .	82
6.2	Data analysis techniques . . . . .	82

6.2.1	Iterative reconvolution . . . . .	82
6.2.2	Sources of error . . . . .	84
6.3	Simulations . . . . .	84
<b>7</b>	<b>VUV measurement</b>	<b>85</b>
7.1	High Harmonic Generation . . . . .	86
7.2	Experimental setup . . . . .	87
7.2.1	Laser beamline . . . . .	87
7.2.2	VUV line . . . . .	88
7.2.3	Detection system . . . . .	89
7.3	Preliminaries . . . . .	89
7.3.1	VUV spectrum . . . . .	90
7.3.2	IRF measurement . . . . .	90
7.3.3	Control of the bias fraction . . . . .	92
7.4	Data analysis . . . . .	93
7.5	Fit procedure . . . . .	94
7.6	Results . . . . .	96
7.6.1	Data . . . . .	96
7.6.2	Limitations . . . . .	101
7.6.3	Discussion . . . . .	102
7.6.4	Perspectives . . . . .	103
<b>8</b>	<b>Na-22 measurement</b>	<b>105</b>
8.1	Phenomenology . . . . .	105
8.2	Experimental setup . . . . .	106
8.3	Preliminaries . . . . .	108
8.3.1	Characteristics of the start signal . . . . .	109
8.3.2	Characteristics of the stop signal . . . . .	110

8.3.3	IRF measurements . . . . .	113
8.3.4	Control of the bias fraction . . . . .	116
8.3.5	Background . . . . .	116
8.4	Data analysis . . . . .	118
8.4.1	Cuts and background estimation . . . . .	118
8.4.2	Fit procedure . . . . .	119
8.4.3	Results . . . . .	119
8.4.4	Summary . . . . .	119
<b>9</b>	<b>Conclusions</b>	<b>121</b>
	<b>Bibliography</b>	<b>123</b>



# List of Figures

1.1	X-ray and proton irradiation	2
1.2	Depth dose comparison	3
1.3	RBE comparison	4
1.4	Peak spread for Carbon	5
1.5	PET scanner	7
1.6	Image reconstruction in PET	8
1.7	Coincidences in PET exam	10
1.8	TOF-PET schematics	11
1.9	Improvement of TOF-PET	12
2.1	Photo electric effect	16
2.2	Compton scattering	18
2.3	$\gamma$ cross section	18
2.4	Energy deposition in scintillator	19
2.5	Electron hole recombination	21
2.6	Core to valence luminescence	23
2.7	Cerenkov effect	26
2.8	Cerenkov emission cone	27
3.1	PMT schematics	32
3.2	MCP principle	34
3.3	MCP schematics	35

3.4	I-V plot Silicon detectors . . . . .	37
3.5	Example of SiPM . . . . .	38
3.6	SiPM layer structure . . . . .	39
3.7	NINO chip . . . . .	40
3.8	Time-over-threshold . . . . .	41
4.1	Cerenkov production . . . . .	45
4.2	Model functions . . . . .	47
4.3	Cramer Rao evolution - rise time . . . . .	49
4.4	Cramer Rao evolution - Cerenkov . . . . .	50
4.5	Threshold crossing example . . . . .	50
4.6	Photon rank RMS . . . . .	51
4.7	Rank variance - rise time . . . . .	51
4.8	Rank variance - Cerenkov . . . . .	52
5.1	RMS comparison . . . . .	60
5.2	Electron path in lattice . . . . .	60
5.3	LSO photoelectric and Cerenko production . . . . .	61
5.4	Photopeak selection for Cerenkov simulation . . . . .	63
5.5	Scintillation/Cerenkov ratio in the first 100 ps . . . . .	63
5.6	Simulated time profiles for LSO . . . . .	64
5.7	Geant4 SLitrani absorption and reflection . . . . .	65
5.8	Geant4 SLitrani specular and diffusive reflection . . . . .	66
5.9	Geant4 SLitrani size ratio variation . . . . .	66
5.10	Geant4 SLitrani gain profiles . . . . .	67
5.11	Spectro fluorimeter . . . . .	69
5.12	Sipat - LuAG excitation/emission . . . . .	70
5.13	CeF <sub>3</sub> - LuAG excitation/emission . . . . .	70

5.14	BGO excitation/emission . . . . .	70
5.15	Spectro photometer . . . . .	71
5.16	Transmission curve for LuAG and LSO . . . . .	72
5.17	Transmission curve for LuAG CeF <sub>3</sub> . . . . .	72
5.18	Light Yield setup . . . . .	73
5.19	Single electron and LSO <sup>137</sup> Cs spectrum . . . . .	75
5.20	QE of R2059 PMT . . . . .	75
6.1	TCSPC technique . . . . .	78
7.1	HHG phenomenology . . . . .	86
7.2	VUV line . . . . .	88
7.3	VUV DAQ . . . . .	90
7.4	VUV spectrum . . . . .	91
7.5	VUV setup IRF . . . . .	92
7.6	. . . . .	93
7.7	Range influence on toy model parameters . . . . .	96
7.8	Influence of statistics on likelihod . . . . .	97
7.9	Likelihood for Sipat LYSO . . . . .	97
7.10	LYSO Sipat and Proteus profile . . . . .	98
7.11	LSO CTI and LSO:Ce,Ca profile . . . . .	99
7.12	LGSO and CeF <sub>3</sub> profile . . . . .	99
7.13	BGO profile . . . . .	99
7.14	LuAG:Ce (0.08%) profile . . . . .	100
7.15	LuAG:Ce (0.5%) and LuAG:Ce (0.44%) profile . . . . .	100
7.16	LuAG:Ce (0.13%) and LuAG:Pr profile . . . . .	101
8.1	Na <sup>22</sup> decay scheme . . . . .	106
8.2	. . . . .	107

8.3	NINO signal sample . . . . .	107
8.4	MCP signal sample . . . . .	108
8.5	Start characteristics . . . . .	109
8.6	Laser trigger . . . . .	110
8.7	. . . . .	111
8.8	MCP corrected response (laser trigger) . . . . .	112
8.9	Corrected IRF . . . . .	113
8.10	. . . . .	114
8.11	. . . . .	115
8.12	. . . . .	115

# 1

## Motivations

Cancer is considered to be the second biggest killer after cardiovascular diseases: there were an estimated 14.1 million cancer cases around the world in 2012, of these 7.4 million cases were in men and 6.7 million in women. This number is expected to increase to 24 million by 2035 Ferlay (2012).

Although surgery remains the most diffuse and successful treatment, radiotherapy is an important and effective option used for curative and palliative management of malignant tumors. In approximately the 50% of clinical cases, radiation therapy is a part of the initial treatment and it is usually conducted by means of high-energy X-rays Durante (2010).

Results of radiotherapy are improved when a high dose of radiation with high biological effectiveness is delivered to the tumour with the least possible dose to the surrounding tissues, especially in the case of critical organs Linz (2012). In order to increase the conformity of the dose delivered to the tumour, diverse technologies have been considered and used. Traditional forms of radiotherapy, X-ray tubes (energy  $\sim$  100 keV) or radioactive isotopes, have been replaced by linear accelerator delivering ( $\sim$  10 MeV) from different directions (e.g. Intensity Modulated Radio Therapy). Although being widely used as a standard in radiation therapy, the effectiveness of conventional electromagnetic radiation is limited by the intrinsic characteristics of interaction with matter. With respect to this, the

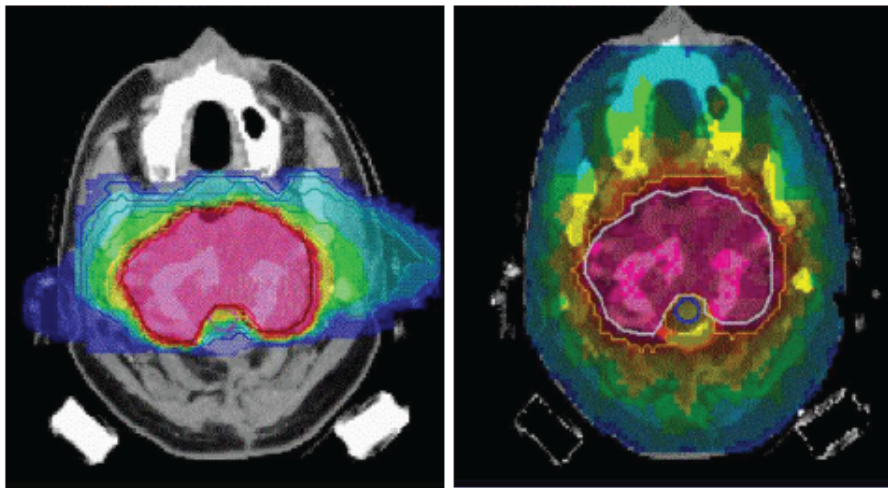


FIGURE 1.1: Comparison of treatment plans for a large target volume in the base of the skull. Plan for carbon ions (left) and IMRT (right) Durante (2010).

scientific community is directing his attention towards possible improvements of ion beam therapy Amaldi (2011). In particular two aspects disfavours the usability of electromagnetic radiation with respect to ion for tumour targeting: the depth dose profile, which does not allow for an optimal dose deposition to the tumour sparing vital organs, and the inferior biological effectiveness, which is the limiting factor in case of radio resistant tumours. Heavier charged particles, like protons and ions (He-Ca) have the potentiality to overcome the limits of conventional therapy. As explained in the next section, ion beam therapy is more effective for targeting deep lying or inoperable tumours. The issues connected to range uncertainties require the development of an effective imaging technique for beam monitoring. Since this thesis is focused on the operational parameters of one of these techniques, Time-Of-Flight Positron Emission Tomography, a brief introduction of ion beam techniques and in-vivo monitoring is given in this chapter.

## 1.1 Particle therapy

### 1.1.1 *Ion beam therapy*

The first proposition of ion beam therapy was presented in 1946 by R. Wilson Wilson (1946). The original idea was to exploit the physical properties of ion interaction in matter

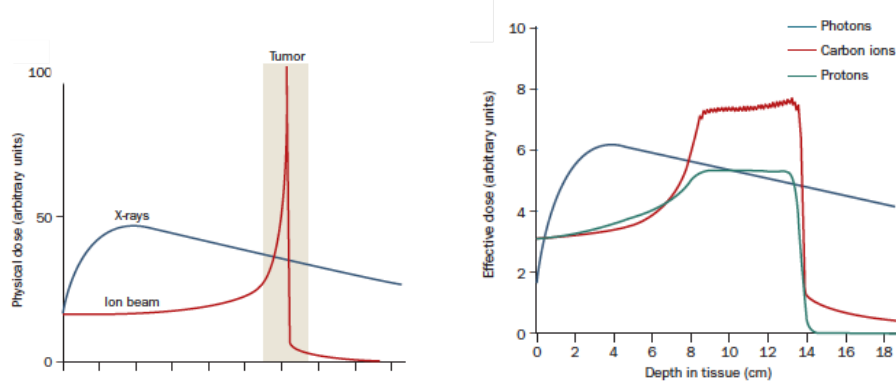


FIGURE 1.2: Comparison of the depth-dose relationships for X-rays and high-energy charged particles. In treatment of large tumors, the Bragg peak must be broadened by use of overlapping beams with different energies Durante (2010).

to improve the precision in radiotherapy treatments. Making use of the so called Bragg peak, that is using the fact that protons and ions in general deposit a maximum of energy at the end of their trajectory, the treatment could save the surrounding tissue from radiation overdose.

The dose deposited by photons, considered as the gold standard for tumour treatment, is maximum close to the beginning of the trajectory in the body and is characterized by an exponential decrease. As a consequence, an undesired radiation dose is delivered to healthy tissues around the targeted tumour.

The recent therapeutic interest of ions in the field of radiotherapy relies mainly on their high relative biological effectiveness. LET (linear energy transfer) has long been viewed as the main parameter to discern the biological effect of different kinds of radiation. It is a measure for the energy deposited by a charged particle traveling through matter. LET is closely related to stopping power and is not a constant value, since it changes along the particle's path (es 10 KeV/ $\mu$ m for photons, 100 KeV/ $\mu$ m for protons, 1000 KeV/ $\mu$ m for ions). When considering ions of different atomic number LET becomes a limited parameter to evaluate the biological effect.

In this sense the relative biological effectiveness (RBE) is considered the most accurate quantity, since it is defined as the biological effect of one type of ionizing radiation relative

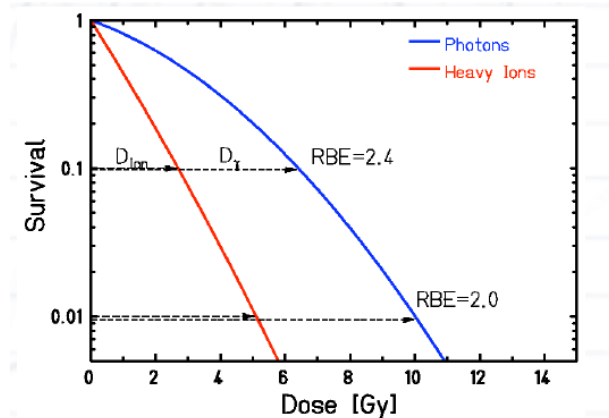


FIGURE 1.3: Comparative plot of RBE for photons and heavy ions.

to another, given the same amount of absorbed energy. As the charge of the incident ions increases, so does the probability of severe DNA damage. An elevate RBE in the Bragg peak region has clearly been demonstrated for ions heavier than Helium Linz (2012). As a consequence they prove to be more effective for targeting radio resistant or inoperable tumours.

### 1.1.2 Beam delivery

Ion beams are delivered by either cyclotrons or synchrotrons. In the first case the beam has a fixed energy which is tuned by means of degraders in order to deliver the correct dose profile. In the case of synchrotron the beam is delivered in spills and the energy is varied between spills. In the case of Carbon only synchrotrons can be used. To deliver the dose to the planned target volume (PTV) different energies are superimposed in order to obtain the so-called spread-out Bragg peak (SOBP). The beam is usually delivered in a passive beam shaping setup or a scanning system.

Different sources of error can worsen the dose delivery profile, such as patient mis positioning and evolution of the tumour/morphology of the patient. In addition the complex physics of ion interaction leads to imprecisions in the treatment plannings, due to fragmentation of the incident beam and range uncertainties.

Usually treatment planning systems cope with these problems by irradiating a volume

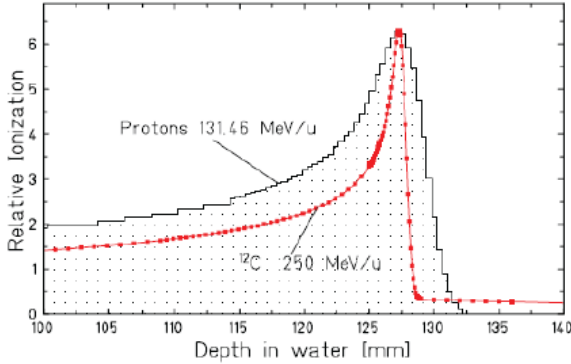


FIGURE 1.4: Bragg curves of proton and C-ions having the same mean range (water phantom and ionization chamber) Schardt (2007).

larger than the tumour itself, called planning target volume (PTV) which contains the clinical target volume (CTV). Complex compensating systems, including x-ray imaging techniques and patient positioning systems, allow to reduce errors in the dose profiles delivered. Treatment plannings of ion therapy rely for example on accurate values of particle range in tissue obtained from Hounsfield unit of computed tomograms, leading to uncertainties of 1 – 3% in range calculations Enghardt (2004).

The dose delivered by a ion beam system is much more sensitive to these deviations than the one delivered by a photon beam. Due to the high biological effectiveness of ion beams, wrong ranges could lead to dramatic under dosage to the tumour or over dosage to organ at risk surrounding. As a consequence a three-dimensional non invasive imaging technique for ion beam therapy monitoring is required. Since ions, unlike photons, are stopped completely in the patient volume, technology like portal imaging are not suitable. The attention of the community is thus focused on positron emission tomography (PET), which relies on the peculiar characteristics of  $\beta^+$  decay.

### 1.1.3 Monitoring of the beam

Several attempts have already been undertaken to systematically assess the benefit of the PET method for beam monitoring, the principal one being the set up installed at the experimental carbon ion therapy unit at the Gesellschaft fur Schwerionenforschung

Darmstadt (GSI) Parodi (2004). Two alternatives can be considered: the use of positron radioactive ions as projectiles for dose delivery or the detection of  $\beta^+$  activity given by nuclei fragmentation. As an example of the first approach it is interesting to consider the effort made at the Heavy Ion Accelerator in Chiba (Japan), where radioactive beams of  $^{11}C - ^{10}C$  ions deliver an activity of  $10^3 - 10^5 \text{ Bq Gy}^{-1} \text{ cm}^{-3}$  within the irradiated volume. Due to the low production rate of secondary radioactive ions, this approach has been only partially successful.

Another possibility is to make use of the  $\beta^+$  activation given by the fragmentation of stable ions interacting with the tissue. The radioactivity is a direct product of the irradiation and, although the activity density is rather low (around  $600 \text{ Bq Gy}^{-1} \text{ cm}^{-3}$  for protons), this method provides a rather cheaper and feasible solution Enghardt (2004). The activity slides very fast under a reasonable threshold for detectability and the most effective solution is an in-beam scanner. In-beam PET is currently the main method implemented clinically for *in situ* monitoring of charged hadron radiotherapy Crespo (2007).

## 1.2 Positron Emission Tomography

### 1.2.1 Principles

Positron Emission Tomography (PET) has been introduced as a nuclear medicine imaging technique which measures the distribution of a positron-emitting radionuclide (tracer), which is injected into the body on a biologically active molecule. In the case of in-beam PET the activity is present in the body of the patient due to the activation induced by proton interaction.

After the injection, or during the dose delivery, the subject of a PET study is placed within the field of view (FOV) of a number of detectors capable of registering incident  $\gamma$  rays. The radionuclide in the radio tracer decays and the resulting positrons subsequently annihilate with electrons after travelling a short distance ( $\sim 1 \text{ mm}$ ) within the body.

Each annihilation produces two 511 keV photons travelling in opposite directions and these photons may be interact with detectors surrounding the subject. The detector elec-

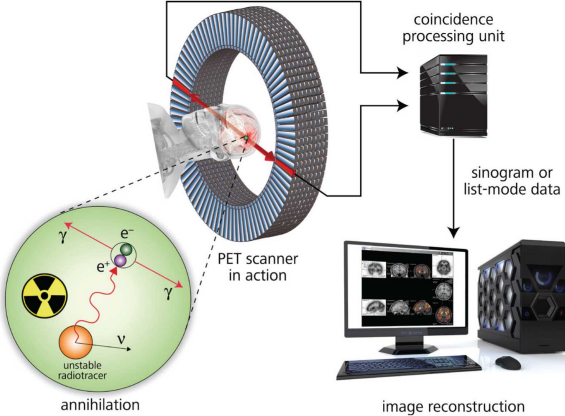


FIGURE 1.5: Schematic view of PET scanner.

tronics are linked so that two detection events unambiguously occurring within a certain time window may be called coincident and thus be determined to have come from the same annihilation. These events can be stored in arrays corresponding to projections through the patient and reconstructed using standard tomographic techniques. The resulting images show the tracer distribution throughout the body of the subject. The scheme of a PET scanner is shown in figure 1.5.

As already mentioned, positron emission tomography relies on the  $\beta^+$  decay of a radionuclide. The nucleus of the radionuclide can convert a proton into a neutron

$$p \rightarrow n + e^+ + \nu_e$$

As positrons travel through human tissue, they give up their kinetic energy principally by Coulomb interactions with electrons. As the rest mass of the positron is the same as that of the electron, the positrons may undergo large deviations in direction with each Coulomb interaction, and they follow a tortuous path through the tissue as they give up their kinetic energy.

When the positrons reach thermal energies, they start to interact with electrons either by annihilation, which produces two 511 keV anti-parallel photons, or by the formation of a hydrogen-like orbiting couple called positronium. In its ground-state, positronium has two forms: ortho-positronium, where the spins of the electron and positron are parallel,

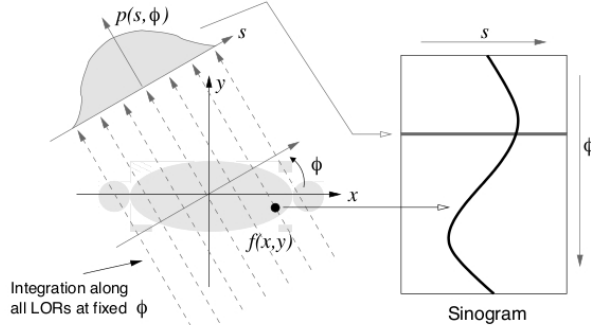


FIGURE 1.6: Extraction of a sinogram from a 2D acquisition.

and para-positronium, where the spins are anti-parallel. Para-positronium again decays by self-annihilation, generating two anti-parallel 511 keV photons. Ortho-positronium self-annihilates by the emission of three photons. Both forms are susceptible to the pick-off process, where the positron annihilates with another electron. Free annihilation and the pick-off process are responsible for over 80% of the decay events.

### 1.2.2 Image reconstruction

After all corrections have been applied to the data acquired, the number of counts assigned to a LOR joining a pair of crystals is proportional to a line integral of the activity along that LOR. Parallel sets of such line integrals are known as projections. For image reconstruction, the most commonly used algorithms are the analytical method called filtered back projection and iterative reconstruction schemes. In particular iterative methods are often preferred over analytical approaches because they can account more effectively for the noise structure and can use a more realistic model of the system. Moreover advances in computation speed and faster algorithms allowed iterative methods to receive growing clinical acceptance. An iterative method has five basic components.

- A model for the image, that is a discretization of the image domain into pixels (2-D) or voxels (3-D) or other exotic models.
- A system model that relates the image to the data. A system model  $M$  is characterized by elements  $M_{ij}$  related to the image system that represent the probability that an

emission from voxel j is detected in projection i

- A model for the data which describes the statistical relation between the value obtained and the value expected
- A governing principle that defines the parameters of a "best" image, often expressed as a cost function (e.g. Maximum likelihood)
- An algorithm that optimizes the cost function.

This last issue has been implemented in several ways, ranging from gradient-based algorithms to the commonly used Expectation Maximization (EM) algorithm and its variations (OSEM).

### *1.2.3 Sources of noise and sensitivity*

In a PET scanner, each detector generates a timed pulse when it registers an incident photon. These pulses are then combined in coincidence circuitry, and if the pulses fall within a short time-window, they are deemed to be coincident. A coincidence event is assigned to a line of response (LOR) joining the two relevant detectors. In this way, positional information is gained from the detected radiation without the need of a physical collimator. This is known as electronic collimation. When a physical collimator is used, directional information is gained by preventing photons which are not normal or nearly normal to the collimator face from falling on the detector. In electronic collimation, these photons may be detected and used as signal. Coincidence events in PET fall into four categories: true, scattered, random and multiple, as shown in figure 1.7.

True coincidences occur when both photons from an annihilation event are detected by detectors in coincidence, neither photon undergoes any form of interaction prior to detection, and no other event is detected within the coincidence time-window.

A scattered coincidence is one in which at least one of the detected photons has undergone at least one Compton scattering event prior to detection. Since the direction of the photon is changed during the Compton scattering process, it is highly likely that the

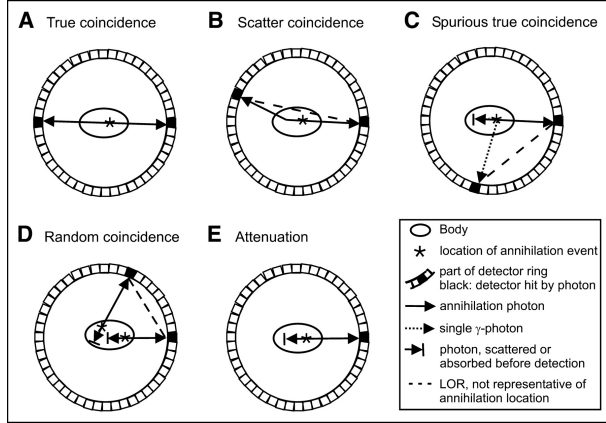


FIGURE 1.7: Phenomenology of PET examination. The cases b, c, d lead to loss of resolution.

resulting coincidence event will be assigned to a wrong LOR. Scattered coincidences add background to the true coincidence distribution which changes slowly with position, decreasing contrast and causing the isotope concentrations to be overestimated. They also add statistical noise to the signal. The number of scattered events detected depends on the volume and attenuation characteristics of the object being imaged, and on the geometry of the PET scanner.

Random coincidences occur when two photons not arising from the same annihilation event are incident on the detectors within the coincidence time window of the system. The number of random coincidences in a given LOR is closely linked to the rate of single events measured by the detectors joined by that LOR and the rate of random coincidences increase roughly with the square of the activity in the FOV. As with scattered events, the number of random coincidences detected also depends on the volume and attenuation characteristics of the object being imaged, and on the geometry of the scanner. The distribution of random coincidences is fairly uniform across the FOV, and will cause isotope concentrations to be overestimated if not corrected for. Random coincidences also add statistical noise to the data.

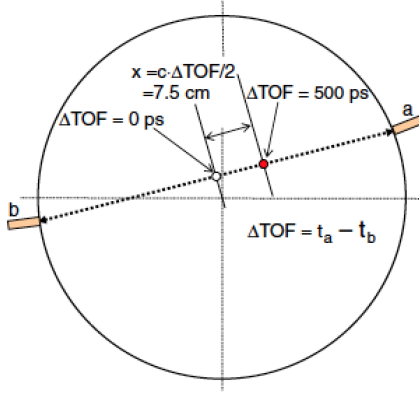


FIGURE 1.8: Example of time of flight information usage in PET examination.

#### 1.2.4 Time-Of-Flight PET

It has been shown that in-beam PET could not provide definitive information to the oncologist when medium to large tumors are involved Fiedler (2006). This is due to the operative parameters of scanners available on the market, with relatively slow scintillators and tomographs covering small solid angles. A decisive improvement could be given by time-of-flight PET (TOF-PET).

Recent developments in scintillator technology and read out electronics allow to build detectors able to detect the time difference between the moment of detection of the opposed  $\gamma$  rays in coincidence. If we define a LOR between two detectors A and B, the distance between the center of the LOR and the annihilation point is given by

$$x = (t_b - t_a) \cdot c/2 \quad (1.1)$$

where  $c$  is the speed of light. Thus the spatial resolution is proportional to the coincidence time resolution (CTR) of the system. Scanners available on the market today could deliver a 600 pico seconds time resolution, that translates to a positional uncertainty of 9 cm (FWHM) on the LOR. The quality of the tomographic image largely benefits from the timing information of a TOF-PET scanner, since it reduces considerably the contribution of Compton scattered photons and from photons from outside the field-of-view (FOV). As a consequence the background from scattered and random coincidence is largely suppressed.

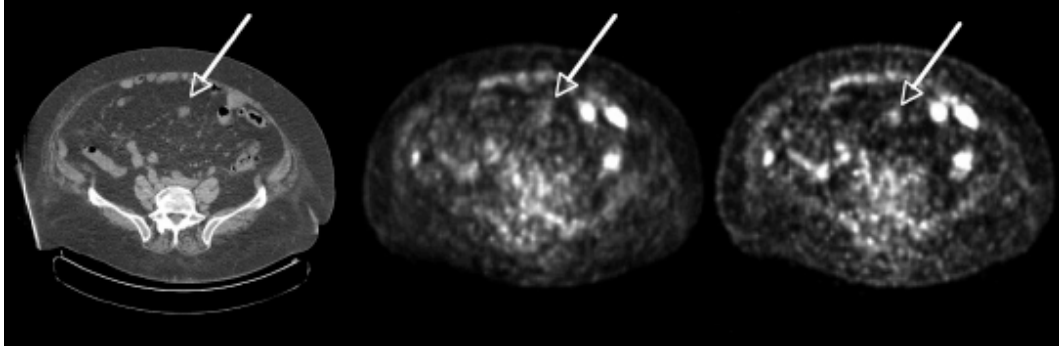


FIGURE 1.9: Representative transverse sections: low dose CT (left), non-TOF ML-EM (middle), and TOF ML-EM (right). The patient with colon cancer (119 kg, BMI = 46.5) shows a lesion in the abdomen seen in CT much more clearly in the TOF image than in the non-TOF image Karp (2008).

The signal to noise ratio (SNR) is thus dramatically improved Karp (2008). In the case of in-beam PET this is relevant, since it has been shown Fiedler (2006) that during particle irradiation a considerable amount of activity is transported outside the FOV by metabolic processes. Moreover a high background signal is typical of carbon ion beams Enghardt (2004). A useful and practical estimation of the gain in signal to noise can be formalized as follows

$$G = \frac{SNR_{TOF}}{SNR_{nonTOF}} = \sqrt{\frac{2 \cdot D}{c \cdot CTR}}$$

where D is the diameter of the volume under examination, c is the speed of light and CTR is the coincidence time resolution. Thus a CTR of 100 ps FWHM translates into a 1.5 cm resolution on the position and a SNR gain of 5 (corresponding to a sensitivity gain of about a factor 25) compared to non TOF systems.

### 1.3 Outline of the thesis

#### 1.3.1 From high energy physics to medical applications

The work outlined in these pages have been sponsored by *The European training network in digital medical imaging for radiotherapy* (ENTERVISION) at the *European Center of Nuclear Research* (CERN). ENTERVISION was established in February 2011 in response to the critical need for reinforcing research in online 3D digital imaging in order to deliver

some of the key elements and building blocks for realizing the vision for early detection and more precise treatment of tumours. The present work was hosted by CERN, the European Organisation of Nuclear Research, based in Geneva, Switzerland. CERN was established by a formal act in Paris, on 1st of July 1953, as an organisation that *shall provide for collaboration among European States in nuclear research of a pure scientific and fundamental character, and in research essentially related thereto*. Thourought its history, CERN provided experimental and theoretical tools to study and understand the fundamental forces governing our universe, in a continous effort to improve our understanding of elementary physics.

The ECAL detector at the CMS exeriment at the LHC was build with the fundamental contribution of the collaboration hosting this thesis: the Crystal Clear Collaboration. It was founded in 1990 as an international academic network of laboratories and industrial partners for the development of scintillating crystal detectors as well as their applications. It comprises experts in crystallography and solid state physics as well as in radiation detection and instrumentation. Its first goal was the development of a radiation-hard crystal for the ECAL detector, leading to the development of PbWO<sub>4</sub> (PWO) as the material selected for CMS calorimeter. More recently the group has been focusing on the study of new materials for hadronic and electromagnetic calorimeters for future particle accelerators. In parallel, the collaboration engaged in a effort of technology transfer to other domains exploiting the expertise developed in scintillating detectors. It is quite natural to focus the attention to medical physics, with particular respect to nuclear medicine since the requirements for detectors used in medical physics and detectors for high energy experiments are similar.

### 1.3.2 Study of time profiles

This thesis is devoted to the full characterization of the parameters that influence time resolution in a scintillator/photodetector setup, with particular attention focused on the impact of time profiles of heavy scintillators on the performance.

The first part of the presented work has the objective of describing the fundamental model that governs light production and collection in a PET-like setup. To this purpose a model based on multi-exponential time profiles has been implemented on an existing framework, widening the scope of usage by evaluating the role of Cerenkov photons produced by low energy radiation.

Moreover in order to properly characterized the operational parameters of a scintillator setup, a comparative analysis of ray tracing softwares has been conducted, namely the two packages SLitrani and Geant4. The latter has been chosen to build the simulation framework that allowed to disentangle the various source of resolution degradation.

Finally the work focused on the measurements and evaluation of rise time. Non zero rise time in scintillating systems is given by the different processes characterizing energy deposition inside a crystalline lattice, with utmost relevance of the latest stage of electron hole thermalization. The time scale of this phenomenon is  $\sim 100$  ps and until now has proven to be difficult to estimate due to the intrinsic limitations of detection setups.

Thus a time resolved study of different species of crystals is proposed in the last two chapters of this thesis. Namely the excitation is varied from the 36 eV of a VUV femto second source to the 511 KeV of a  $\gamma$  source.

# 2

## Scintillating detectors

In the field of medical applications, the energies of the  $\gamma$  photons to be detected are usually of the order of hundreds of keV. In the case of PET scanners the energy of the two back to back photons is 511 KeV. A simple approach to estimate the parameters of the incoming radiation is to make use of a fluorescent sample coupled to a photo detector. A standard setup would include a heavy scintillator crystal which converts the incoming radiation into visible photons. The following steps of the detection process involve transportation to the entrance window of the photodetector, conversion of the photons into an electric signal and subsequent manipulation of the signal by readout electronics.

### 2.1 Interaction of radiation with matter

In this work we are mainly concerned with the interaction of  $\gamma$  radiation with matter, thus focusing our attention on the three existing mechanisms: photo electric interaction, Compton interaction and pair production. Moreover electrons produced by ionizing interactions can polarize the medium, giving origin to the Cerenkov effect and producing visible photons, which can be of foremost importance in the case of timing application.

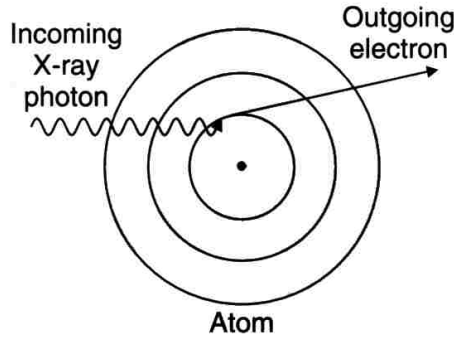


FIGURE 2.1: Phenomenology of the photo electric effect

### 2.1.1 Photoelectric effect

In the case of the photoelectric effect an electron from an atom is freed upon absorption of the incoming photon:



Due to conservation of momentum and energy this phenomenon does not occur with free electrons. The gamma energy transferred to the electron equals the binding energy of the electron itself minus its resulting kinetic energy  $E_{e^-}$

$$E_{e^-} = E_\gamma - E_b \quad (2.2)$$

The photoelectric effect is predominant at low energies ( $E \geq 100$  KeV) and favours tightly bound K-shell electrons. An approximation of the photo electric cross section is given by

$$\sigma_{pe} \propto \frac{Zn}{E_\gamma^{3.5}} \quad (2.3)$$

The vacancy created can be filled through capture of bound or free electrons, eventually generating characteristics X-rays.

### 2.1.2 Compton scattering

Compton scattering is the inelastic scattering of the incoming photon with a weakly bound electron in the material:

$$\gamma + \text{atom} \rightarrow (\gamma') + e^- + \text{atom}^* \quad (2.4)$$

Contrary to the photoelectric effect, this only concerns quasi-free electrons of the material. The photon transfers part of its energy to the electron, which is freed from its shell. Applying conservation of energy and momentum it is possible to derive the energy of the scattered gamma as well as the direction and energy of the freed electron.

$$E_{\gamma'} = \frac{E_\gamma}{1 + \frac{E_\gamma}{m_e c^2} (1 - \cos\theta)} \quad (2.5)$$

The angular distribution can be described by the Klein-Nishina formula. It can be noted that forward scattering direction are favoured as the incoming photon energy increases

$$\frac{d\sigma_{cpt}}{d\omega} = Z \cdot \frac{e^2}{4\pi\epsilon_0 m_e c^2} \cdot \frac{1}{2} \cdot \frac{E'_\gamma}{E_\gamma} \left( 1 - \frac{E'_\gamma}{E_\gamma} \cdot \sin^2\theta + \left[ \frac{E'_\gamma}{E_\gamma} \right]^2 \right) \quad (2.6)$$

The total cross section can be computed by integrating the differential cross section over the angle, with  $\epsilon = h\nu/mc^2$  and  $r_e = h/mc$ .

$$\sigma_{KN} = 2\pi r_e^2 \frac{1+\epsilon}{\epsilon^2} \left[ \frac{2(1+\epsilon)}{1+2\epsilon} - \frac{\ln(1+2\epsilon)}{\epsilon} \right] + \frac{\ln(1+2\epsilon)}{2\epsilon} - \frac{1+3\epsilon}{(1+2\epsilon)^2} \quad (2.7)$$

### 2.1.3 Pair production

If the energy of the gamma exceeds  $2m_e c^2 = 1.02$  MeV, the impinging photons can also be converted into an electron-positron pair. The cross-section of the pair production is given at low energies (thus low screening) by

$$\sigma_{pair} = 4\alpha r_e^2 Z^2 \left( \frac{7}{9} \ln 2 \frac{E}{m_e c^2} - \frac{109}{54} \right) \quad (2.8)$$

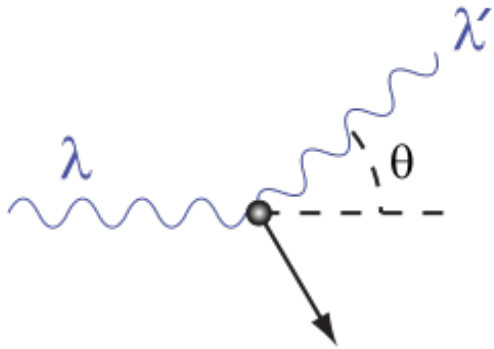


FIGURE 2.2: Phenomenology of Compton scattering

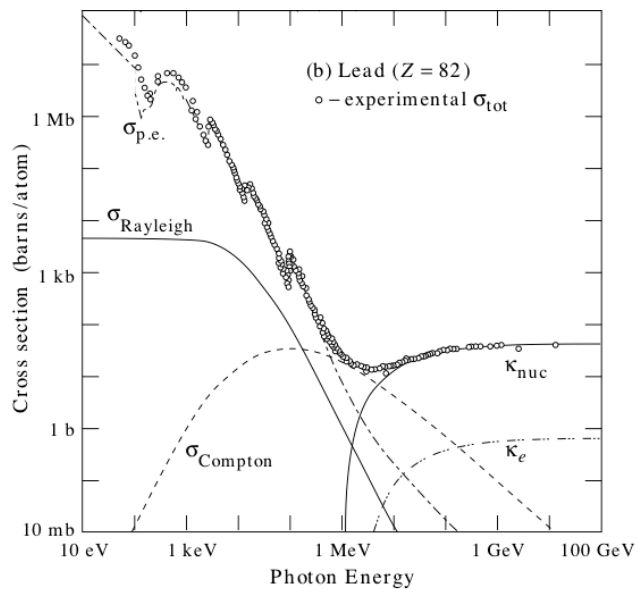


FIGURE 2.3: Cross section for the different processes in lead

The cross section is very low compared to that of photoelectric and Compton effect until the energy of the  $\gamma$  approaches several electron Volts. Thus for the energies involved in medical applications pair production can be neglected.

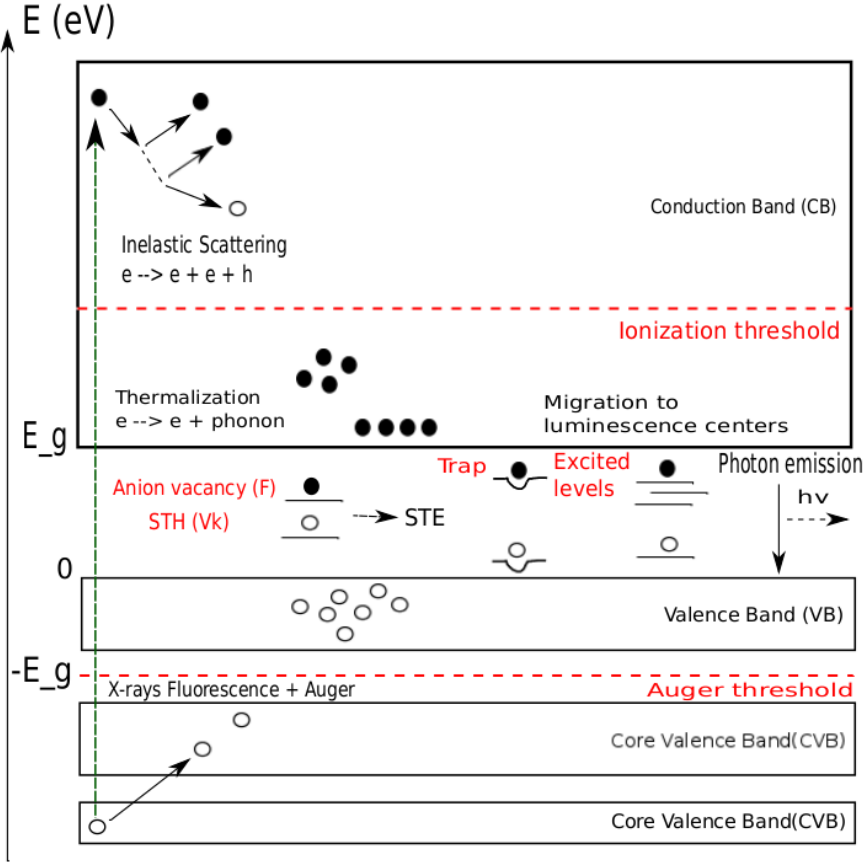


FIGURE 2.4: Chain of energy deposition processes in crystals

## 2.2 The scintillation mechanism

As a general idea the scintillation process can be considered as the conversion of the energy of an incident  $\gamma$  quantum or particle into a certain number of low energy photons Rodnyi (1997). In a way it can be therefore defined as a wavelength shifting process Lecoq (2006).

After a ionization event, generated by the mechanisms presented above in the case of a  $\gamma$  interaction, the scintillator relaxes towards a new equilibrium. This process is characterized by a multitude of sub processes, that can be depicted by band diagrams as the one in figure 2.4. As long as the energy of the particles is high enough, it is transferred to secondary particles of low energy, creating an electromagnetic cascade. A crystal though is an ordered ensemble of atoms, so the electrons in the KeV range start to couple with electrons and

atoms of the lattice. As a result of their interaction with electronic states of the material, couples of electrons and relative vacancies are created. The electron hole pairs migrate in the lattice above and below the ionization threshold until they are trapped by a defect or recombine on a luminescent center. Alternatively they cool down by coupling to the lattice vibrations until they reach the top of the valence band (hole) or the bottom of the conduction band (electron). They can also form loosely bound structures called exciton, with en energy slightly smaller than the bandgap energy. The scintillator itself must contain luminescent centers, either intrinsic or extrinsic (doping ions). These molecular systems in the lattice present characteristic transitions between excited states. Recombination brings the release of optical photons, at characteristic wavelengths.

### 2.2.1 Creation of electron hole pairs

To analyze more in depth the mechanisms of the scintillation, we can consider an intermediate energy  $\gamma$  ray ( $\sim 500$  KeV) interacting with the scintillator material. In this case the photoelectric effect is dominant. Thus it will produce a hole in a inner shell (usually K shell) and a free or quasifree electron.



The energy of the primary electron will be  $h\nu - E_k$  where  $E_k$  is the K level energy. The relaxation then happens differently for electrons and holes.

The ionized atom ( $A^+$ ) can relax either radiatively, thus emitting a photon, or nonradiatively, generating a secondary electron. This is know as the Auger effect. Thereafter a cascade of both radiative and nonradiative processes takes place. The Auger electron and the primary electron begin a proces of electron-electron scattering or phonon emission. In the case of a radiative emission, the soft x-ray photon emitted may be absorbed producing a new deep hole and free electron.

The electron on the other hand will ionize an atom



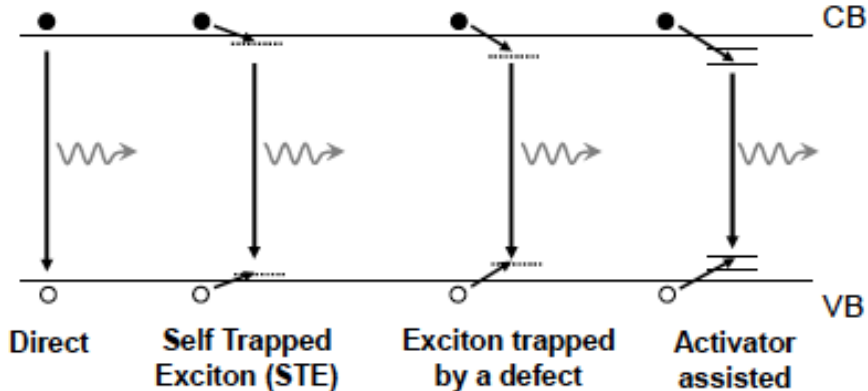


FIGURE 2.5: Different processes for electron hole recombination

The two undistinguishable electrons will undergo a number of other ionization processes, resulting in an avalanche of secondary electrons and holes. At some point the secondary products of these processes are not able to ionize the medium anymore. A fast electron can in principle interact also with valence electrons of the medium, producing collective oscillations known as plasmons. Plasmons behave as quasiparticles, with an energy of  $\sim 10$  eV and can decay into e-h pairs.

This ensemble of avalanche processes continues until the generated secondaries are not able to create further ionization. At this point electrons and holes start to interact with the vibrations of the lattice in a stage called thermalization, via different mechanisms of electron-phonon interaction. As a consequence, at the end of this chain of de-excitation processes, low energy electronic excitations are present: electrons in the conduction band, holes in the valence band, valence excitons, core excitons.

### 2.2.2 Intrinsic luminescence

Electron and holes have several ways to recombine after thermalization and give rise to scintillation photons. The simplest emission process is direct recombination

$$e + h \rightarrow h\nu \quad (2.11)$$

Recombination can more effectively take place when the energy of the electron and hole has decreased, so that they form an exciton. However the various impurities and lattice

defects play a very important role in the scintillation process. Thermalized carriers can be bound in some places of the lattice where atom or defects are localized. For example many ionic crystals shows phenomena of localization of the valence hole in the lattice, known as self-trapping. This structure appears when a thermalized hole localizes an anion, polarizing the environment. As a result the hole can be shared between two neighbouring ions forming a  $V_k$  center, and the hole is defined as self-trapped hole. For high energy excitation direct creation of valence exciton is unlikely, so  $V_k$  centers usually capture free electrons. From subsequent de excitation they can emit photons, thus giving rise to the excitonic luminescence.



### 2.2.3 Core to valence transitions

If the core bands of the scintillator lie below the Auger threshold, the most favoured transitions involve holes in the valence band and electron in the conduction band. Some systems though present the so-called cross luminescence. This phenomenon implies a direct core to valence transition, due to the fact that holes in uppermost core bands can not be excited non radiatively Lecoq (2006).

A notable example of core to valence transition is  $BaF_2$ . In this system a  $Ba^{2+} 5p$  core hole is above the Auger threshold and hence Auger effect does not occur. They can recombine directly with electrons from the valence band, in most of the cases radiatively. This leads to a very fast luminescence given by recombination of the core hole, while the primary electron de excitation is more complex thus leading to a slower component.

### 2.2.4 Extrinsic luminescence

Most of the scintillator samples used in this work are extrinsic, that is doped with activation centers that can enhance the intrinsic scintillation properties presented above by favouring direct recombination. Rare earth ions doping, for example, is largely used in scintillator technology because of the parity and spin-allowed transition  $4f^{n-1}5d \rightarrow 4f^n$ . Extrinsic

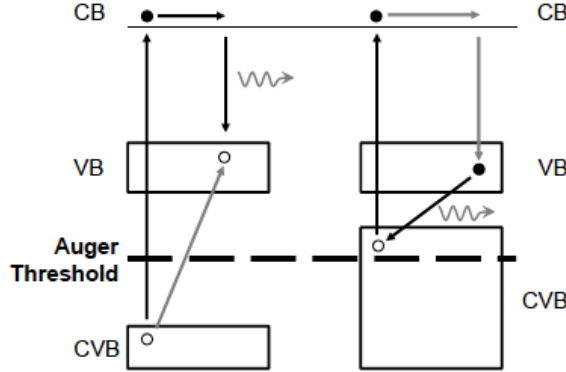


FIGURE 2.6: Direct luminescence (left) versus cross to valence luminescence (right)

scintillators usually present different luminescent mechanisms driven by activated sites Lecoq (2006):

- $e + h + A \rightarrow ex + A \rightarrow A^* \rightarrow A + h\nu$
- $e + h + A \rightarrow A^{1+} + e \rightarrow A^* \rightarrow A + h\nu$
- $e + h + A \rightarrow (A^{1-})^* + h \rightarrow A + h\nu$
- $A \rightarrow A^* \rightarrow A + h\nu$

In the first case the insertion of dopants is able to sufficiently quench the exciton luminescence so that excitation of radiative centers results from a transfer from excited matrix states. A competing process is the direct capture of free thermalized carriers by luminescent center, in the case of electrons or holes. In heavily doped or self-activated crystals ( $CeF_3$ ) direct excitation by ionizing radiation is possible.

### 2.2.5 Quenching phenomena

TO DO

## 2.3 Operational parameters

### 2.3.1 Light yield

One of the features commonly required of a scintillator is to have a high light yield, that is to be an efficient converter of radiation to visible light. In this case the relative light

output of the scintillator,  $L_R$ , can be considered the significant quantity. It is defined as the number of emitted photons per unit of absorbed energy Rodnyi (1997)

$$L_R = \frac{N_{ph}}{E_\gamma} \quad (2.13)$$

The number of produced e-h pairs  $N_{eh}$  depends on the average energy needed for the creation of a low energy e-h pair,  $\chi_{eh}$ . This value depends on the type of lattice and band gap of the material, with a numerical coefficient  $\beta$

$$\chi_{eh} = \beta \cdot E_g \quad (2.14)$$

If  $\alpha$  is the average number of scintillation photons produced by a single e-h pair, the light output is

$$L_r = \frac{\alpha \cdot N_{eh}}{E_\gamma} = \frac{\alpha}{\chi_{eh}} = \frac{\alpha}{\beta \cdot E_g} \quad (2.15)$$

The coefficient  $\alpha$  depends on the transport efficiency of the e-h pairs to the luminescence center and the conversion efficiency of the center itself.

### 2.3.2 Optical properties and light transport

TO DO

### 2.3.3 Energy resolution and nonproportionality

In the case of  $\gamma$  spectroscopy it is necessary to discriminate quanta with different energy. For scintillation detector this fundamental property is characterized by the energy resolution  $R$ , defined as  $\Delta E/E$  (in %) where  $\Delta E$  is the full width at half maximum (FWHM) at pulse height  $E$ . It depends on the characteristics of the scintillator, i.e. materials, size and defects as well as the coupling with the photo detector and the parameters of the photo detectors itself. Statistical fluctuations at any step of the detector chain, from dynode multiplication to photo cathode efficiency in the case of a PMT can worsen the resolution at the peak. Thus energy resolution can be defined as Rodnyi (1997)

$$R^2 = R_S^2 + R_{PM}^2 = R_S^2 + \frac{\delta}{E_\gamma} \quad (2.16)$$

where  $R_S$  and  $R_{PM}$  are, respectively, the scintillator and photomultiplier contributions and  $\delta$  includes photo electron statistics. It is possible to further decompose the scintillator resolution  $R_S$  to take into account the factors depending on the type of scintillator used. In particular it is useful to introduce a term for the transfer efficiency of the optical photons  $R_S$ , a term for inhomogeneity  $R_i$  and a term for nonproportionality  $R_n$

$$R_S^2 = R_t^2 + R_i^2 + R_n^2 \quad (2.17)$$

The interest lies in the fact that the two terms, for inhomogeneity and nonproportionality, account for the intrinsic resolution of the crystal. Inhomogeneity arise from possible imperfections of the scintillator, such as local variations in the concentration of the dopant or optical defects.

Non proportionality arise when scintillators show deviation from stability of excitation spectrum, that is when linearity between energy of the excitation and relative light output is not preserved. This is particularly important for low energy excitation, since scintillation phenomena occur mainly on the surface. Non proportionality is caused by the statistical nature of the creation of secondary electrons and photons and contribute to worsen the resolution.

#### 2.3.4 Cerenkov effect

Cerenkov radiation brings important information both in high energy physics and time resolved PET. Cerenkov radiation occurs when a charged particle passes through a dielectric medium at a speed greater than the phase velocity of light in that medium. The phase velocity of light in a medium of refractive index  $n > 1$  is

$$v_p = \frac{c}{n} \quad (2.18)$$

A charged particle can travel faster than the speed of light if, given its velocity  $v_p$

$$\frac{c}{n} < v_p < c \quad (2.19)$$

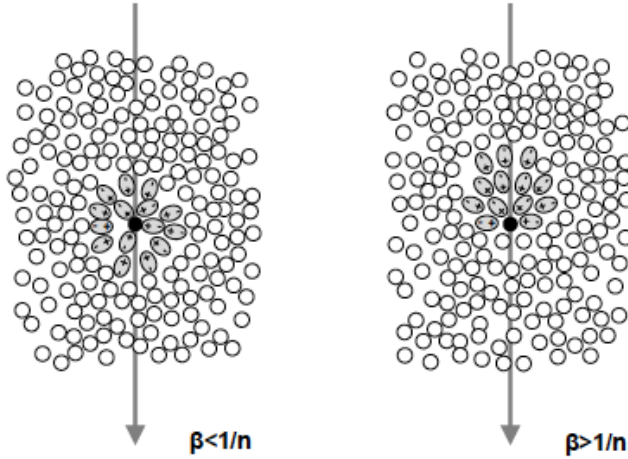


FIGURE 2.7: Phenomenology of Cerenkov effect

This translates to the following condition for the  $\beta$  coefficient of the particle

$$\beta = \frac{v_p}{c} > \frac{1}{n} \quad (2.20)$$

For a particle of a given mass thus the energy threshold is

$$K_{thr} = mc^2 \left( \frac{\sqrt{n^2 - 1}}{n} - 1 \right) \quad (2.21)$$

The phenomenology of Cerenkov effect can be explained considering the polarization of the medium caused by a charged particle traversing it. Below the Cerenkov threshold the dipoles surrounding are symmetrically arranged around the path. As the particle crosses the threshold it travels faster than the speed at which it interacts with the dipoles. This symmetry breaking leads to a non-vanishing dipole moment and thus to the formation of a wave front.

Cerenkov photons are emitted at a characteristic angle in the forward direction, obtained via simple geometrical considerations. The distance traveled by the charged particle in a time  $t$  is  $t \cdot \beta \cdot c$  whereas the distance along which the photon propagates is  $t \cdot c/n$  as shown in figure 2.8. Therefore the characteristic angle at which photons are emitted can be calculated as

$$\cos(\theta_C) = \frac{tc/n}{t\beta c} = \frac{1}{n\beta} \quad (2.22)$$

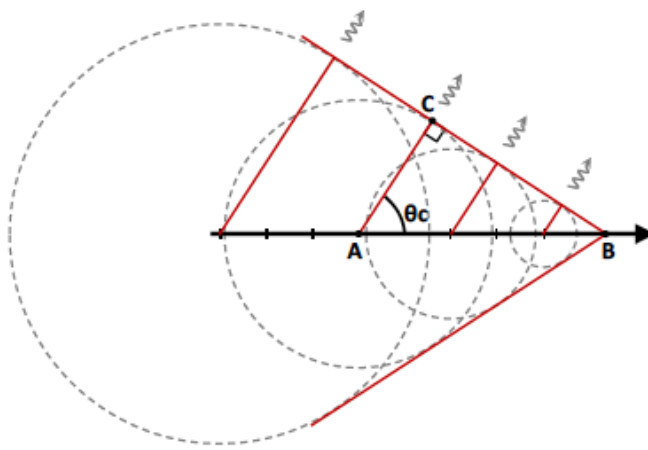


FIGURE 2.8: Sketch of the Cerenkov emission cone

As will be shown in the next chapter, the direction of emission retains a primary interest in the field of particle identification, while it has a negligible impact on timing measurement in PET scanners. It is worth to be noted though that the Cerenkov photons are emitted promptly, taking a relevant share of the first incoming photons. It is useful to consider the number of emitted photons per unit length by a charged particle as a function of the wavelength

$$\frac{dN}{d\lambda dx} = \frac{2\pi z^2 \alpha}{\lambda^2} \left(1 - \frac{1}{\beta^2 n^2(\lambda)}\right) \quad (2.23)$$

Neglecting dispersion in the medium, and integrating over an appropriate interval of wavelengths we obtain that the photons are emitted mostly in the UV range.

$$\frac{dN}{dx} = 2\pi z^2 \alpha \left(1 - \frac{1}{\beta^2 n^2(\lambda)}\right) \int_{\lambda_1}^{\lambda_2} \frac{d\lambda}{\lambda^2} = 2\pi z^2 \alpha \sin^2 \theta_C \left(\frac{1}{\lambda_1} - \frac{1}{\lambda_2}\right) \quad (2.24)$$

A simple calculation shows that, even at the low energies that characterize a PET exam (511 KeV), a non negligible number of Cerenkov photons is produced. As an example, it is interesting to consider the case of the most popular crystal for PET detectors, Lu<sub>2</sub>SiO<sub>5</sub>:Ce (LSO) with a density  $\rho_{LSO} = 7.48 \text{ g/cm}^3$  and a refractive index of 1.82 Jellison (2012). Given the K-shell binding energy of the electron (63 KeV Thompson (2009)), we can estimate, with the help of formula 2.21, the energy threshold for Cerenkov production for

electrons at 448 KeV. If we then consider a freed electron from the K-shell and its average range in LSO (265  $\mu\text{m}$  Berger (2005)), we can make use of formula 2.24, given that

$$\sin^2(\theta_c) = 1 - \frac{1}{n^2\beta^2} = 0.58 \quad (2.25)$$

The number of optical photons produced in the wavelength range 180 - 800 nm is  $\sim 40$ .

## 2.4 Most common scintillation processes

The main crystal species used in this study will be briefly presented in this section, in particular with respect to the scintillation mechanism. Light yield and time profiles will be more deeply analyzed in the next chapters.

- **Lutetium Oxiorthosilicate:** Lutetium oxyorthosilicate (LSO) is a widely used crystal for PET detection and high energy physics. The crystal structure of Lu<sub>2</sub>Si<sub>0</sub><sub>5</sub>:Ce the Lu atoms occupy two equally-populated, crystallographically independent sites, and the Cerium doping atom is assumed to substitute for the Lutetium atom ?. The 5d level is split by the crystal field of the host lattice into 3 sublevels, and the 4f ground state is split by the spin-orbit interaction into two levels. The luminescence of LSO is due to parity-allowed electric dipole transitions from the lowest 5d sublevel to the split 4f ground state, with emission band at 410 nm. Due to the high density (7.4 g/cm<sup>3</sup>), very fast emission ( 40 ns) and high light yield (>40000 photons/MeV) is considered to be on the most important crystals for calorimetry.
- **Lutetium Aluminum Garnet:** Lutetium Aluminum Garnet (Al<sub>5</sub>Lu<sub>3</sub>O<sub>12</sub>) has been recently proposed as a candidate for future calorimetry experiment?, for the high density (6.73 g/cm<sup>3</sup>) and fast emission profile of the main components (< 60 ps). LuAG crystals present relevant intrinsic and extrinsic scintillator characteristics. The intrinsic scintillation of LuAG comes from processes related to self trapped exciton de excitation. Indeed in case of strong electron hole coupling to the lattice a carrier can be trapped in its own field. STEs in LuAG lead to absorption band at 7.1 and

7.3 eV and emission upon recombination at 5 eV. STEs may also localise around  $\text{Lu}_{\text{Al}}^{3+}$  defects and give rise to emission at 3.3 eV. This recombination mechanisms are very slow, usually  $2 \mu\text{s}$  and for this reason the LuAG lattice is often doped, as the case of LSO with a rare earth activator (Yb, Pr, Ce). In particular we will consider the case of Cerium and Praseodymium doping. The case of Cerium doping is similar to the LSO case, with an emission band peaking at 520 nm that corresponds to the  $\text{Ce}^{3+} 5d \rightarrow 4f$  transitions. In the case pf Praseodymium doping, apart from the excitonic luminescence, two bands are present, corresponding to the  $\text{Pr}^{3+} 4f5d \rightarrow 4f^2$  and  $4f^2 \rightarrow 4f^2$  contained respectively in the 285-450 nm band and 450-880 nm band ?. For calorimetry application only the first is relevant.

- **Cerium Fluoride:**

- **Bismuth Germanate:** Bismuth Germanate ( $\text{Bi}_4\text{Ge}_3\text{O}_{12}$ ), or BGO, is been considered for many years the gold standard for radiation detection, in nuclear medicine and high energy physics, because of its high density ( $7.13 \text{ g/cm}^3$ ), high scintillation output ( $>20000 \text{ photons/MeV}$ ) and relatively fast emission (two components, main one 300 ns). BGO is an intrinsic scintillator, that is no dopant is added. The observed fluorescence is assigned to  ${}^3\text{P}_1 \rightarrow {}^1\text{S}_0$  transitions of  $\text{Bi}^{3+}$ , with broad emission band at 490 nm ?.



# 3

## Photo detectors

After the scintillation phase in the crystal, visible photons are generated and coupled to a photodetector. At this stage the photodetector generates an electric signal related to the photon rate, by generating free electrons in vacuum or electron-hole pairs in a semiconductor.

As they are used as fundamental components of the experimental apparatus, the vacuum photodetector technology and the solid state technology will be presented. Vacuum photodetectors are characterized by the production of free electrons in an external photocathode by photoelectric interaction. The produced electrons undergo acceleration in a focused electric field and are multiplied by secondary interaction before being transferred to the read out circuitry. Photo multiplier tubes (PMT) and micro channel plates tubes (MCP-PMT) are prominent examples of vacuum technology.

In the case of solid state photo detectors, photons interact directly in the bulk material, where electron-hole pairs are produced. The pairs are then accelerated in the electric field and multiplied by ionization in the semiconductor itself. In the work presented here, Silicon photo multipliers (SiPM) are used as representative of this kind of detector.

### 3.1 Photo multiplier tubes

Photo multiplier tubes are largely used vacuum photo detection devices and have been diffusively discussed in literature Knoll (2000). In figure 3.1 the main elements of a photo

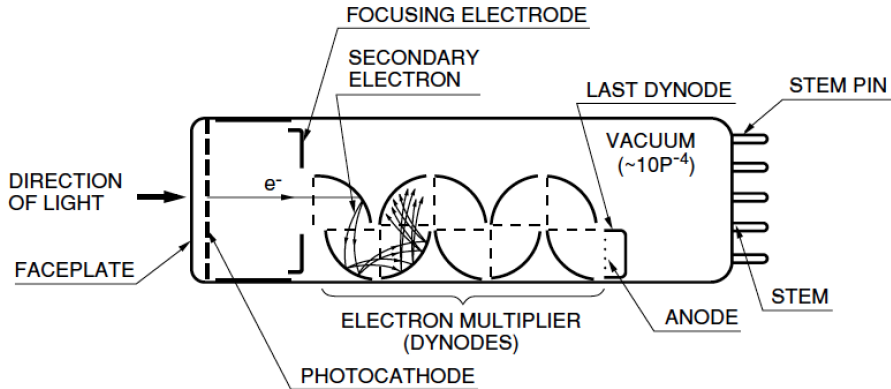


FIGURE 3.1: Schematics of a Photo-Multiplier Tube Hamamatsu (2006).

multiplier tube are sketched:

- a photocathode, which converts visible photons into an electron flux
- an electron-optical input system which focuses and accelerates the electron flux
- an electron multiplier consisting of a series of secondary emission electrodes (dynodes)
- an anode, which collects the electron flux and supplies the output signal

Photoemission is due to a fraction of the incident visible photons that transfer enough energy to the electrons of the photo cathode to extract them. Then the focusing system allows the freed electrons to reach the first dynode, i.e. the first multiplication stage. The electrons are accelerated and focused by electric field between the dynodes and the required potential gradient is usually guaranteed by a voltage divider.

#### 3.1.1 Properties of PMT

- **quantum efficiency:** photocathode are usually made of deposited photo emissive semiconductor. They can be semi transparent or opaque, depending on the place

where the emissive material is deposited with respect to the input window. The most used materials are silver-oxygen-caesium (AgOCs), antimonyum caesium (SbCs), and the bi-and trialkali compounds SbKCs, SbRbCs, and SbNa<sub>2</sub>KCs. The most important parameter to be considered is the cathode radiant sensitivity, defined as the ratio of the cathode current  $I_p$  to the incident flux  $\Phi$

$$S_k(A/W) = \frac{I_p(A)}{\Phi_e(W)} \quad (3.1)$$

The incoming photons have usually a certain spectral composition and the cathode is not uniformly sensitive in this range. With this respect the most used quantity is the quantum efficiency, that is the ratio of the number of photo electrons emitted,  $n_k$ , to the number of incident photons,  $n_i$

$$QE = \frac{n_k}{n_i} = S_{k,\lambda} \frac{h\nu}{e} \quad (3.2)$$

where  $e$  is the electron charge and  $S_{k,\lambda}$  is the monochromatic sensitivity, defined as

$$S_{k,\lambda} = \lim_{d\lambda \rightarrow 0} \frac{dI_p}{d\Phi_e} \quad (3.3)$$

- **gain:** if the number of photo electrons that reach the first dynode is  $n$ , and the gain of the dynode is  $g_1$ , the number of secondary electrons is  $n \cdot g_1$ . If  $g_i$  is the gain of the single dynodes, after  $N$  stage the number of electrons collected at the anode are

$$n_a = n \prod_{i=1}^N g_i \quad (3.4)$$

It is possible to define the gain of the photo multiplier as the ratio  $I_a/I_p$  where  $I_a$  is the anode current given by a photo current  $I_p$ . If we define a collection efficiency for each dynode, depending of geometrical parameters,  $\eta_i$ , then the gain  $G$  is

$$G = \eta \prod_{i=1}^N \delta_i \eta_i = \eta \prod_{i=1}^N g_i \quad (3.5)$$

- **transit time spread:** transit time spread is the transit-time fluctuation of the signal when identical light pulses hit the same part of the photo cathode. The time resolution of a tube is then often quoted as the FWHM of the probability distribution of the fluctuations. If the probability distribution of electrons arriving at the anode is assumed to be gaussian, then the response  $R_\delta(t)$  to a delta-function light pulse is

$$R_\delta(t) = \frac{1}{\sigma_R \sqrt{2\pi}} \exp\left(-\frac{(t - t_{tts})^2}{2\sigma_R^2}\right) \quad (3.6)$$

where  $t_{tts}$  is the mean transit time.

### 3.2 Micro Channel Plate-PMT

A micro channel plate is a two-dimensional array of glass capillaries mounted in parallel as shown in figure 3.2. The diameter of the channels lies in a range of 5 to 20 microns and their

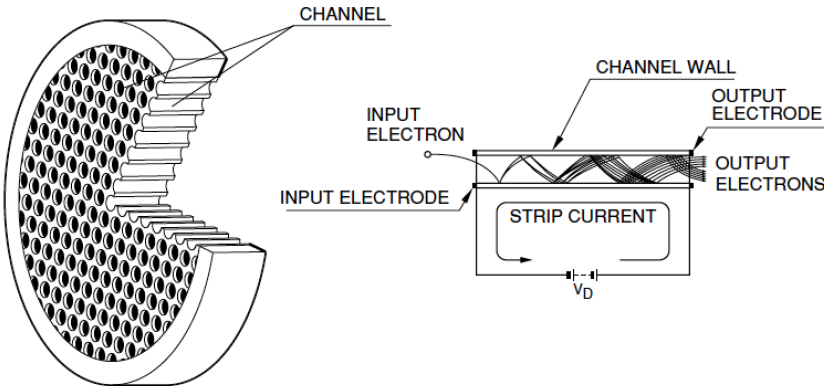


FIGURE 3.2: Work principle of a Micro Channel Plate Hamamatsu (2006).

internal walls are treated so to have a defined electrical resistance and secondary emissive properties. At both ends of the plate high voltage is applied, so that a primary electron impinging on the wall of a channel produces a multiplication chain. Since they resemble in function a structure of dynodes, microchannel plates are usually used in combination with vacuum detector technology in an assembly known as MCP-PMT.

A MCP-PMT consists of an entry window, a photo cathode, one or more micro channel plates and a collecting anode. To operate a MCP-PMT it is necessary to provide a certain

voltage to the system. To this purpose standard voltage divider circuits are usually adopted, in order to guarantee drifting spaces for electrons before and after the photocathode, and multiplication in the MCP stack Hamamatsu (2006).

### 3.2.1 Properties of MCP

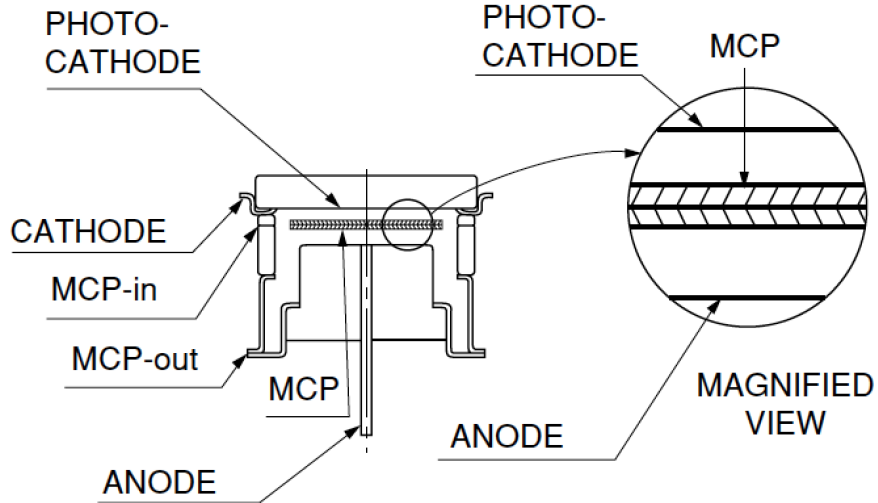


FIGURE 3.3: Schematics of a MCP-PMT Hamamatsu (2006).

- **quantum efficiency:** in terms of quantum efficiency they do not differ from standard PMTs, since they make use of the same photo cathode technology.
- **gain** The gain of an MCP-PMT depends primarily on the number of plates stacked. Geometrically is determined by the length-to-diameter ratio af a channel  $\alpha$ , as

$$G = \exp\left(\frac{\Delta \cdot L}{d}\right) = \exp(\Delta \cdot \alpha) \quad (3.7)$$

where  $\Delta$  is the gain factor and depends on the plate material,  $L$  and  $d$  are, respectively, the length and diameter of the micro tube.

- **ion feedback, electron backscattering:** strongly correlated with the characteristics of gain are the problems of ion-feedback and electron backscattering. As the

voltage, and thus the gain, increases, it is more and more likely for a photoelectron to be backscattered towards the photo cathode or for an ion to undergo the same process from the stack. Ions can be commonly stripped from residual gas in the drifting area or from interaction in the plate. This leads to the production of secondary pulses, that contribute to the worsening of the time response of the device.

Connected to this is also the issue of ageing, since ion bombardment damages the photocathode as the vacuum in the device degrades with time. Partial solution to this problem has been found by depositing an Aluminum protection layer on the plate and by modifying the inclination of the micro tubes in the so called Chevron geometry Va'vra (2004).

- **time characteristics:** the rise and fall time of a MCP-PMT are ultra-short, due to the multiplication characteristics of the device. This translated into typical signals contained in a few nanoseconds, or even less. For timing application though the most important parameter to consider is the transit time spread (TTS). The TTS is the spread in the arrival time of a bunch of photon produced by a converted electron in the photocathode. The time response of MCP-PMTs will be analyzed further in the next chapters.

### 3.3 Silicon photo multipliers

Recently solid state photo detectors have become competitive with vacuum devices, and for some applications they represent the ideal solution. Their advantage lies in the high photon detection efficiency, their low sensitivity to high magnetic fields, their compactness and cost efficiency Dolgoshein (2003). In particular the insensitivity to high magnetic fields, given by the feature that no electrons are travelling in the vacuum between dynode and dynode, makes the solid photo detector the first choice for PET-MRI scanners or high energy experiments. With respect to the MCP-PMT, also characterized by high operability in magnetic fields, silicon devices still maintain a high photon detection efficiency, that is the

conversion efficiency of incoming photons in to electron hole pairs determining in principle a better energy and time resolution.

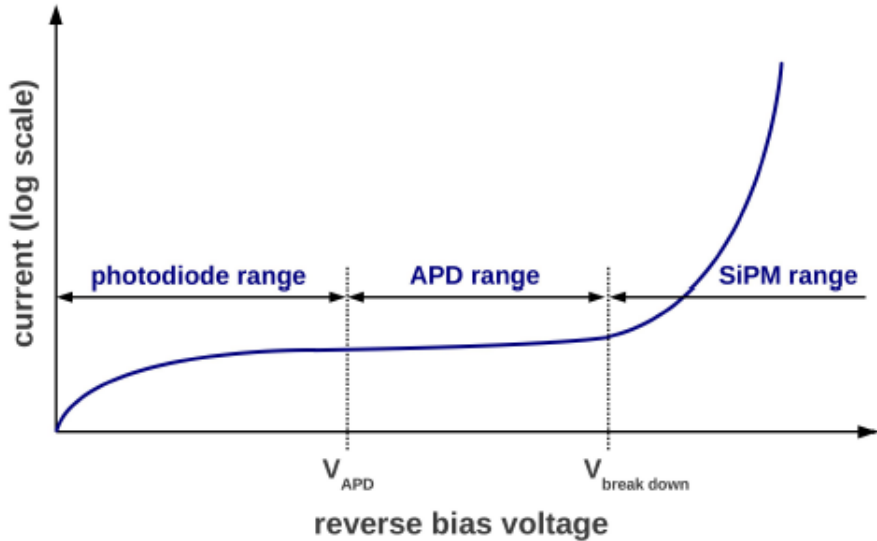


FIGURE 3.4: Voltage current plot for Silicon devices. SiPMs work in Geiger mode Gundacker (2014).

Solid state photo detectors are usually p-n junctions reversely biased and, depending on the value of the bias voltage, different operational parameters adapt to fundamentally three modes. As seen in figure 3.4 the voltage can applied can be low, as in photo diodes, leading to low currents proportional to the incoming flux. Moving towards the proportionality region the freed electrons are able to ionize further, thus determining a net gain of the device. Avalanche photodiodes (APDs) are a common device operated in this region. Finally a third region, characterized by non-proportionality is the precipitous operating segment of Geiger mode APD (G-APD). In the Geiger mode region both electrons and holes are able to futher ionize the bulk, and the device is sensible to single photo electrons. The created avalanche must be quenched either externally by a series of quenching resistors or actively. Many G-APD cells connected in parallel are the basic structure of silicon photomultipliers (SiPM) or multi pixel photon counters (MPPC).

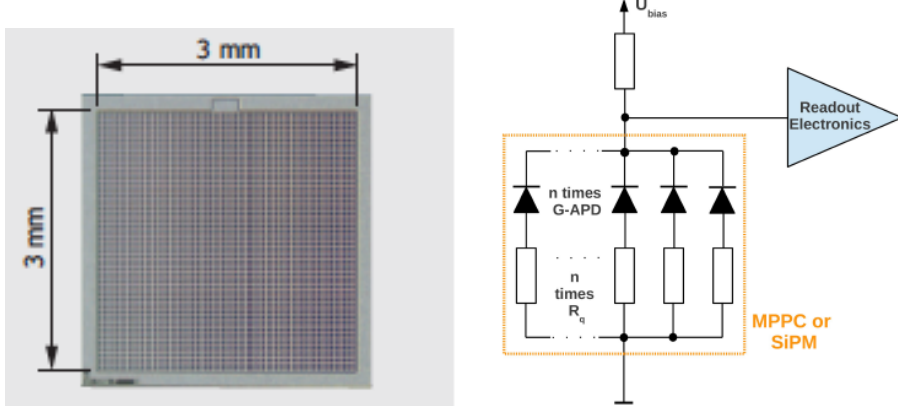


FIGURE 3.5: Example of Hamamatsu MPPC (left) and basic structure of a SiPM (right) Gundacker (2014).

### 3.3.1 Analog SiPM

The structure of an analog SiPM is composed by series of Geiger mode cells in parallel, and the self sustained avalanche is usually quenched by external resistors or active quenching circuitry. The basic schema of a standard SiPM with quenching resistors is shown in figure 3.5.

The structure of a G-APD optimized for detection of blue light is shown in figure 3.6. On top of the low resistivity bulk layer an epitaxial layer with a high dopant concentration region is located. The implantation of opposite charge constitutes the p-n junction with a very thin layer extremely doped to assure electric field uniformity. The cell and the quenching resistor are connected on the top surface. Finally a passivation layer ( $\text{SiO}_2$ ) protects the device. Due to its low index of refraction ( $n = 1.55$  in the blue) with respect to the one of Silicon ( $n = 3.5$ ) Fresnel losses can occur, usually compensated by the presence of anti-reflection coatings.

### 3.3.2 Properties of SiPM

- **photon detection efficiency:** the photon detection efficiency can be defined as

$$PDE = QE \cdot \epsilon \cdot P_{avalanche} \quad (3.8)$$

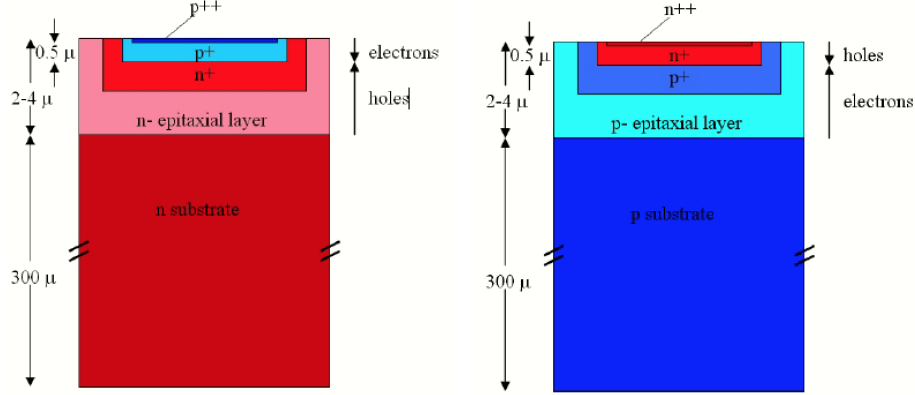


FIGURE 3.6: Layered structure of a IR (left) and UV (right) SiPM Gundacker (2014).

where  $QE$  is the quantum efficiency,  $\epsilon$  is the geometric fill factor and  $P_{avalanche}$  is the probability of triggering an avalanche. The  $QE$  has already been introduced for ordinary photo cathodes and it is comprehensive of Fresnel losses. The fill factor  $\epsilon$  is defined as the ratio of the sensitive area to the total area of the detector. Finally the  $P_{avalanche}$  is the probability of an electron or hole to cause an avalanche and it depends on the bias overvoltage.

- **gain:** the gain of an analog SiPM can be written as

$$G = \frac{C \cdot U_{ov}}{q} \quad (3.9)$$

where  $C$  is the cell capacitance,  $U_{ov}$  is the bias overvoltage and  $q$  is the charge  $q = 1.602 \cdot 10^{-19} C$ . This value is typically between  $10^5$  and  $10^7$ .

- **spurious events** a dark count is the random production of charge carriers in the depleted region which leads to a regular signal. This type of unwanted event is typically uncorrelated, provided the the dark count rate (DCR) is low enough. It strongly depends of temperature, and typical values range between 100 kHz to few MHz at 25°C.

Optical crosstalk on the other hand is determined by the trigger of an avalanche by an optical photon produced in a neighbouring cell. Indeed optical photons produced in

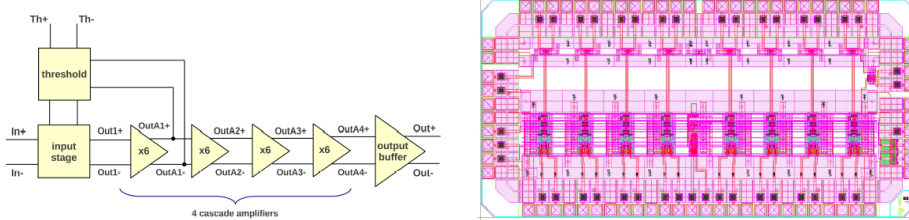


FIGURE 3.7: Structure of the cascade amplifier (left) and scheme (right) of the NINO chip Anghinolfi (2004).

avalanches can travel to other cells, causing correlated spurious pulses. These pulses can occur even after a delay of several microseconds, due to the secondary photons generating electron hole pairs.

Moreover charge carriers can be trapped in the bulk and released tens to hundreds of nanoseconds later determining afterpulsing.

- **saturation:** if SiPMs are exposed to high photon fluxes, saturation effects may occur. The detector is intrinsically limited by the number of cells: if the number of photons is small compared to the number of cells provided PDE correction, the SiPM signal is proportional to the light signal. In the opposite case, the signal is saturated.

### 3.3.3 The NINO chip

Signal generated by SiPMs are in the range of milli Volts, thus we make use of low noise electronics to read out the detector. In the study presented the ultrafast front-end preamplifier-discriminator chip called NINO, developed at CERN Anghinolfi (2004) has been used. Originally designed for the time-of-flight subdetector of the ALICE experiment, it matches the main requirements of a SiPM readout, that is speed, low noise, minimum slew rate, low input impedance. The chip has eight channels, designed for differential readout. Each channel is characterized by an amplifier with 1-ns peaking time, a discriminator with a minimum detection threshold of 10 fC and an output stage.

The input stage is a current-to-voltage converter and the subsequent signal amplification is performed with four identical cascade amplifiers that operate as a discriminator as well.

The threshold is set by a voltage difference applied on two symmetrical inputs. The NINO chip makes use of the time-over-threshold technique: a squared output pulse is produced when the leading edge is above the set threshold, encoding the timing information. The width of this signal, on the other hand, is a function of the charge collected, thus encoding the energy information.

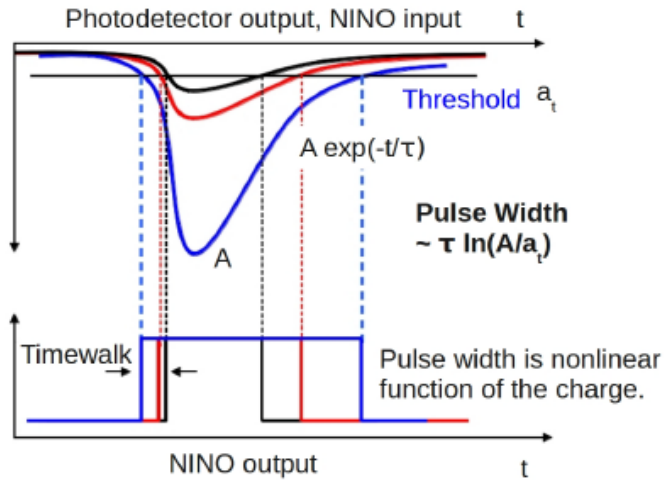


FIGURE 3.8: Principle of operation of a time-over-threshold discriminator Gundacker (2014).



# 4

## A model for scintillation counting

!!! Missing introduction !!!

### 4.1 Signal formation

!!! Missing discussion on signal formation !!!

#### 4.1.1 *Scintillation pulse*

It is customary to describe Hyman (1963) the scintillation pulse as a sum of exponentials. The processes introduced in the previous paragraph, focus the attention on the first step of recombination, and the subsequent radiative transitions. All the processes that characterize electron hole relaxation and particularly thermalization of the pairs, lead to oscillations with respect to the start of the scintillation pulse determining a non zero rise time. For all the practical purposes of this work rise time will be modeled by one or more exponential time components  $\tau_r$ . For what concerns recombination, the radiative transitions can be described by one or more exponential decay times  $\tau_d$ . In the case of LSO:Ce, for example, the transition takes place between the lowest 5d level, which lies just below the conduction band, and two 4f levels, above the valence band. The parity allowed transition accounts for very fast decay times (*sim* 40 ns).

We can consider, then, the absorption of a  $\gamma$  photon at a time  $\theta$ . For many scintillators, we can describe the probability density function for the emission times as the convolution of two exponential functions representing the energy transfer processes and the radiative decay Shao (2006):

$$p_t(t|\theta) = \int_{-\infty}^{\infty} \exp\left(-\frac{t'}{\tau_r}\right) \exp\left(-\frac{t-t'}{\tau_d}\right) \theta(t') \theta(t-t') dt' \quad (4.1)$$

In the case different processes contribute to the scintillation pulse via different energy transfer mechanisms, it may be necessary to consider them Seifert (2012)

$$p_t(t|\theta) = \begin{cases} 0, & t < \theta \\ \sum_i S_i \frac{1}{\tau_{d,i} - \tau_{r,i}} \cdot \left[ \exp\left(-\frac{t-\theta}{\tau_{d,i}}\right) - \exp\left(-\frac{t-\theta}{\tau_{r,i}}\right) \right], & t > \theta \end{cases} \quad (4.2)$$

#### 4.1.2 Cerenkov pulse

As shown in the previous chapter, a non negligible amount of Cerenkov photons can be produced by a low energy  $\gamma$  event. This is the case since in order to extract a time stamp for a certain event, we often make use of single threshold crossing, that is we mainly rely on the information carried by a single photon. Thus if the number of Cerenkov events is not negligible, photons collected at the very beginning of the pulse can come with a high probability from one of these events.

In order to define a Cerenkov pulse, the Geant4 software was used. The software package will be fully analyzed in the next chapter. For the sake of simplicity, we consider the time of production of Cerenkov photons that follow a  $\gamma$  photo electric interaction in a LSO crystal. The delay is given by the geometry of the experiment, in this case the main interest lies in the width of the distribution. In this case, as will be for this chapter, no transit time variation for the photons is considered, so that the distribution of Cerenkov photons modeled is the production one, shown in 4.1. For most practical purposes, and considering that the time scale of the physical quantity, we can safely consider the Cerenkov pulse as a Gaussian curve in time, with a  $\sigma$  in production of  $\sigma = 3$  ps. It is important to underline that, while the scintillation yield of a certain crystalline species will depend strongly on

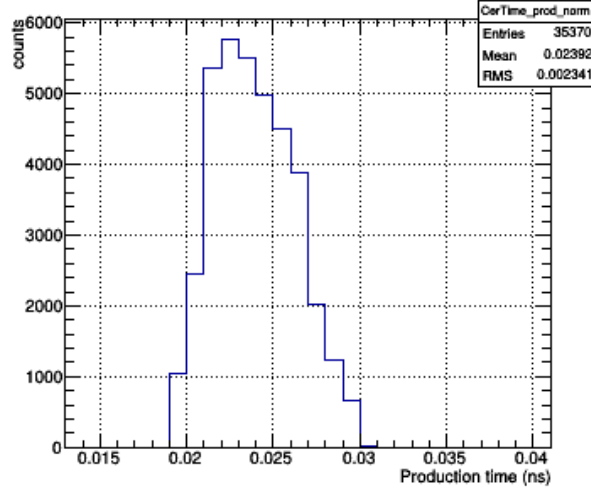


FIGURE 4.1: Cerenkov production profile in LSO by a 511 KeV photon simulated with the Geant4 software package.

the production method (doping concentration, type of dopant, etc.), the Cerenkov yield depends essentially on density and index of refraction. This means that the respective intensity of the two photon production phenomena should be scaled accordingly. In this study we relied on scintillation values measured in laboratory (see next chapter for the measurement setup) and Cerenkov values extracted from Geant4 simulations.

#### 4.2 The Cramer-Rao lower bound

In general, the emission times  $t$  of the detected  $N$  photons can be considered statistically independent and identically distributed (iid). Most photo detectors can be modeled as ideal photon counters, able to detect a time stamp for every incoming photon, a set  $T_N = \{t_1, t_2, \dots, t_N | \theta\}$ .

In order to account for the smearing introduced by the resolution of the detector on the photon time stamps, it is necessary to define its response  $p_T$ . In particular it can be modeled by a Gaussian with a variance equal to the single photon time resolution (SPTR) and a mean equal to the transit time  $t_{TT}$ . The function is truncated at  $t = 0$  not to allow

negative transit times.

$$p_T = \frac{1}{\sqrt{2\pi}\sigma_{S PTR}} \exp \left[ -\frac{(t - t_{TT})^2}{2(\sigma_{S PTR})^2} \right] \quad (4.3)$$

The corresponding pdf for the time stamps is then a convolution of the photon emission rate and the smearing of the detector.

$$p_{t_n}(t|\theta) = p_t(t|\theta) * p_T(t) = \int_{-\infty}^{\infty} p_t(t-x|\theta) \cdot p_T(x) dx = \int_0^{t-\theta} p_t(t-x|\theta) \cdot p_T(x) dx \quad (4.4)$$

And the integral gives

$$p_{t_n}(t|\theta) = A \cdot \sum_i \frac{S_i}{\tau_{d,i} - \tau_{r,i}} \cdot [a_{\tau_{d,i}}(t|\theta) - a_{\tau_{r,i}}(t|\theta)] \quad (4.5)$$

$$+ B \cdot \exp \left( -\frac{(t_{TT} + \mu_{cer} - t)^2}{2(\sigma_{cer}^2 + \sigma_{S PTR}^2)} \right) \quad (4.6)$$

$$\cdot \left[ \operatorname{erf} \left( \frac{-t_{TT}\sigma_{cer}^2 + \mu_{cer}\sigma_{S PTR}^2 - \sigma_{S PTR}^2 t + (t - \mu_{cer})(\sigma_{cer}^2 + \sigma_{S PTR}^2)}{\sqrt{2}\sigma_{S PTR}\sigma_{cer}\sqrt{\sigma_{S PTR}^2 + \sigma_{cer}^2}} \right) \right] \quad (4.7)$$

$$- \operatorname{erf} \left( \frac{-t_{TT}\sigma_{cer}^2 + \mu_{cer}\sigma_{S PTR}^2 - \sigma_{S PTR}^2 t}{\sqrt{2}\sigma_{S PTR}\sigma_{cer}\sqrt{\sigma_{S PTR}^2 + \sigma_{cer}^2}} \right) \quad (4.8)$$

where

$$a_{\tau}(t|\theta) = \frac{1}{2} \exp \left( \frac{\sigma_{S PTR}^2 - 2t\tau + 2\theta\tau + 2t_{TT}\tau}{2\tau^2} \right) \quad (4.9)$$

$$\cdot \left[ \operatorname{erf} \left( \frac{t - \theta - t_{TT} - \frac{\sigma_{S PTR}^2}{\tau}}{\sigma_{S PTR}\sqrt{2}} \right) + \operatorname{erf} \left( \frac{t_{TT} + \frac{\sigma_{S PTR}^2}{\tau}}{\sigma_{S PTR}\sqrt{2}} \right) \right] \quad (4.10)$$

$A$  is the normalization for the scintillation curve,  $B$  is the normalization for the Cerenkov curve,  $\sigma_{cer}$  is the spread of Cerenkov production and  $\mu_{cer}$  is the mean of Cerenkov production, that will be considered at  $\theta$  (we assume that the scintillation pulse and the Cerenkov pulse start at the same moment). The bi exponential model used is shown in figure 4.2,

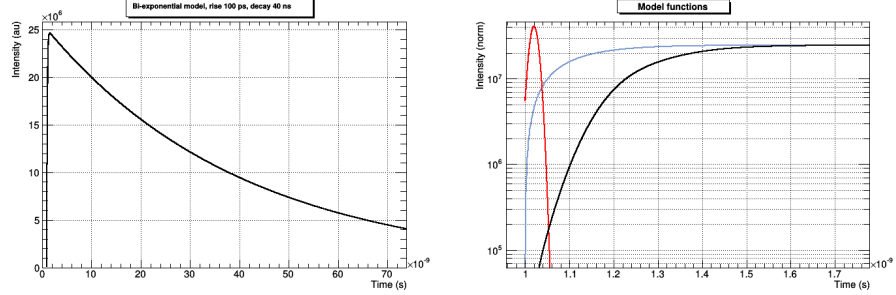


FIGURE 4.2: Bi exponential model used (left) and modification on the rise introduced by Cerenkov photons and detector smearing (right)

as well as the modification in the rise time induced by Cerenkov photons and detector smearing.

The Fisher Information  $I(\theta)$  is defined as

$$I(\theta) = \int_{-\infty}^{\infty} \left[ \frac{\partial}{\partial \theta} \ln p_{t_n}(t|\theta) \right]^2 p_{t_n}(t|\theta) dt \quad (4.11)$$

Since the samples are iid, the information is additive, so that

$$I(\theta) = N \cdot \int_{-\infty}^{\infty} \left[ \frac{\partial}{\partial \theta} p_{t_n}(t|\theta) \right]^2 \frac{1}{p_{t_n}(t|\theta)} dt \quad (4.12)$$

The Cramer Rao theorem states that the variance of any unbiased estimator  $\hat{\theta}$  of  $\theta$  is bounded by the reciprocal of the Fisher information:

$$\text{var}(\hat{\theta}) \geq \frac{1}{I(\theta)} \quad (4.13)$$

In a PET-like experiment the interest lies in the estimate of the photon time of interaction  $\theta$ . Statistically speaking the Cramer Rao theorem gives the intrinsic time resolution limit for any given scintillator with the given parameters.

### 4.3 The order statistics

If it is assumed a specific order in the set of recorder timestamps, it is evident that they are neither independent nor identically distributed. By sorting the elements in  $T_N$  we can create an ordered set  $T_{\bar{N}} = \{t_{\bar{1}} \leq t_{\bar{2}} \leq \dots \leq t_{\bar{N}}\}$ . The pdf for the nth-order statistics is given by Seifert (2012)

$$f_{n|N}(t|\theta) = \binom{N}{n} \cdot n \cdot P_{t_n}^{n-1}(t|\theta) \cdot [1 - P_{t_n}(t|\theta)]^{N-n} \cdot p_{t_n}(t|\theta) \quad (4.14)$$

In this case the set is not iid; thus considering an estimator using a unique timestamps, as the case of analog SiPMs, the Fisher information is

$$I_n(\theta) = \int_{-\infty}^{\infty} \left[ \frac{\partial}{\partial \theta} \ln f_n(t|\theta) \right]^2 f_n(t|\theta) dt \quad (4.15)$$

### 4.4 Intrinsic time resolution

We can now use the framework expanded in the previous section to infer the timing properties of a simplified setup characterized by five parameters:

- the light yield
- the Cerenkov yield
- the rise time
- the decay time
- the spread in Cerenkov emission

Thanks to the Cramer-Rao theorem it is possible to extract the lower bound in coincidence time resolution for a setup with specified parameters. This means that the entire set is used in the statistics, regardless of the method used to extract the time information: this represents a theoretical value given the information contained in the set. It is important to stress that for the moment we do not consider any spread introduced by the transport of

photons inside the volume. This will be considered in the next chapter, where Monte-Carlo simulations will allow to introduce this additional parameter.

In order to weight the importance of the various model parameters in the calculation of the time resolution of the system, we first make use of the entire statistical set, that is we find the lower bound. In a first moment the Cerenkov yield is set to zero. This is the case for crystals with very low collection efficiency or very low Cerenkov production. In the case of samples used in this study this number can be estimated to range between 2 and 10 depending on the crystal and the wrapping condition.

The first consequence of assuming iid samples is that the information is proportional to the number of photons collected. This implies inverse proportionality for the lower limit on the variance. If we assume a light yield of 5000 photons/MeV, which is shown in the next chapter to be a good approximation for LSO crystals, we can focus on the time dependence of the model.

!! Cramer-Rao plots missing !!

FIGURE 4.3: Cramer Rao lower bound as a function of rise time for different values of decay times (left) and S PTR (right)

The role of Cerenkov photons becomes somehow more obscure in this situation. As shown in figure 4.4, a small number of Cerenkov photons collected can in principle worsen the lower bound achievable. This is due to the fact that the fast emission can introduce a higher variance when combined to the bi exponential statistics. This is strongly correlated with the light yield of the crystal measured, since this effect is more and more pronounced as the light yield grows. Indeed when the scintillation photons produced are a few, we start relying mainly on Cerenkov photons. This simply states that a device which could make use of Cerenkov photons in significative number would reach a better value for time resolution since it would not depend on the time profile of the scintillation.

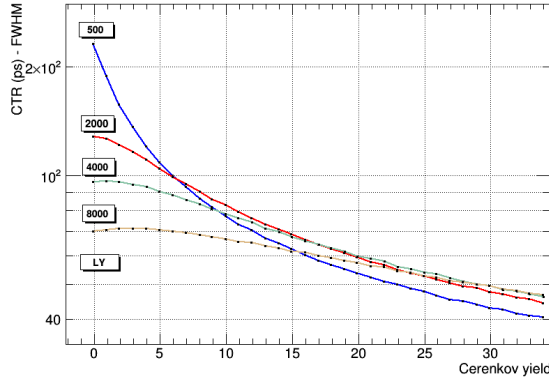


FIGURE 4.4: Cramer Rao lower bound as a function of Cerenkov photons collected

#### 4.5 Effects on signal extraction

If we consider a time pick up system similar to the one used in this study, it is necessary to extend the analysis to the order statistics in use. It is the case of SiPMs used in PET detectors, as shown in 4.5, as the signal is a build up of single cells firing. We then basically rely on the information of a threshold passing. An example of this time pick up method will be shown in chapter 7. In figure 4.6 is shown the time distribution for photon of different

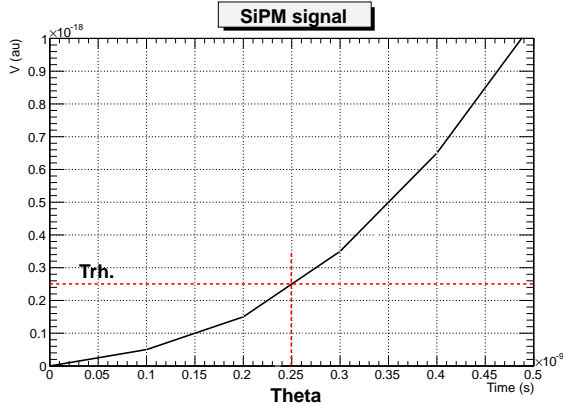


FIGURE 4.5: Example of a time pickup method based on threshold crossing. It is the method used by the NINO chip used in this work.

rank following the order statistics previously obtained, for the case with S PTR = 0 and S PTR = 70 ps. It is already clear that, in general, it is not the first order statistic that

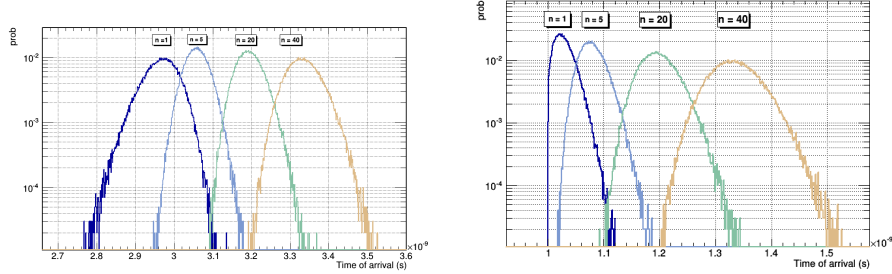


FIGURE 4.6: Time distribution for photon of different rank without (left) and with (right) detector smearing

provides the estimation with the lower variance. This is due to the smearing introduced by the detector. Indeed, a non-smeared time profile would entail a monotonous increase of the variance, as shown in figure ??, where the variance of the  $n$ -th photon collected is plotted, at different parameter values. In the same plot we can focus on the role of rise time on the shape of the curve. Indeed a faster rise time, not only is associated with lower variances for photon of the same rank, as expected, but it slides the order statistics with the smallest variance. As can be seen from a comparison of the variance curves for photons of different

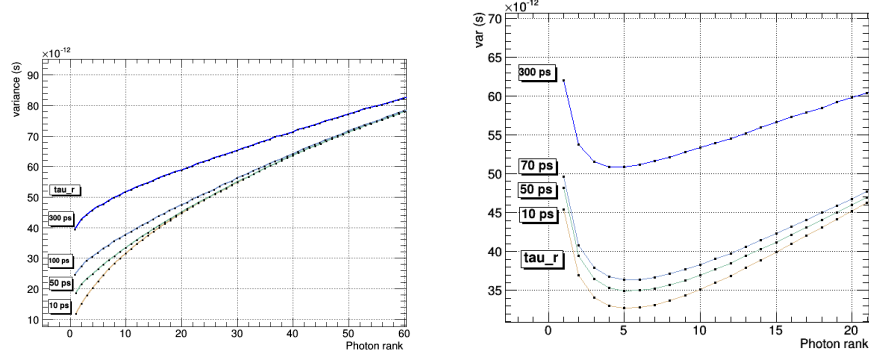


FIGURE 4.7: The evolution of the variance of the  $n$ -th rank photon for different rise time values with  $\text{S PTR} = 0$  (left) and  $\text{S PTR} = 70$  (right).

rank and lower bounds for the same parameters, a detector which makes us of a single time stamp can not reach the lower bound. Thus the late photons carry some information, which is not used in the methods used in this study. An approach to include this photons

in the analysis could make use of digital pick up techniques.

For what concerns Cerenkov photons, it is shown in figure ?? that they have a significant impact only if at least five of them can be collected. Indeed for a very small number of Cerenkov photons the CTR resolution is the same, and so the variance associated with the order statistics with the smallest variance. Things change when a higher number of Cerenkov photons are collected. In this case the ratio between scintillation photons and Cerenkov photons can be quite small, so that we start to rely mainly on the latter. This can be the case for crystal such as LuAG or PbWO<sub>4</sub>. As will be shown in the next chapter, for our purposes the Cerenkov pulse will introduce a modified rise time non negligible when extracting the absolute value.

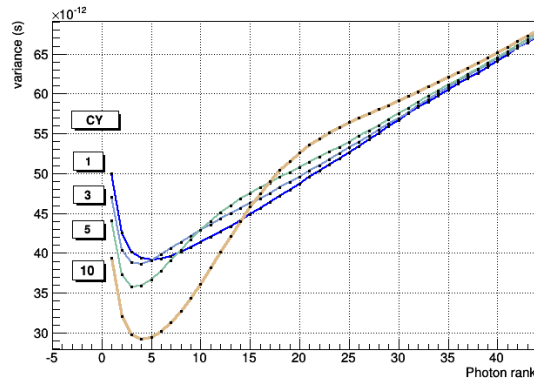


FIGURE 4.8: The evolution of the variance of the n-th rank photon for different Cerenkov yields.

# 5

## MonteCarlo simulation tools

As a second approach to the characterization of scintillating crystals in the aspects that influence timing, Monte Carlo simulation tools have been taken in to account. Indeed, the domain of application of ray tracing softwares is somewhat limited, as will be clear after the discussion in this chapter. Nonetheless it retains a certain importance for what concerns the understanding of the components of resolution loss when it comes to optical propagation of photons. Two software packages have been considered and reviewed Pizzichemi (2012): Geant4 and SLitrani.

### 5.1 Ray tracing

The softwares available and reviewed, that is Geant4 and SLitrani, broadly share the same approach in terms of ray tracing in optical materials. The photon is treated as a particle traveling inside the volume and interacting via precise processes, such as absorption in the bulk, scattering, wavelength shifting and boundary interaction. Effective models are applied when it comes to optical photon production, that is no theoretical implementation of fluorescence phenomena is implemented. In particular we can articulate the approach to ray tracing in three steps:

- the energy deposition model, that defines the voxelized map of the energy deposited

with a certain cut value for processes

- the production phase, where the energy deposition map is translated in to a number of optical photons at a certain predefined wavelength, with relative resolution spread
- the ray tracing phase, where the produced photons are tracked to the end of the volume or until absorption takes place

Before defining the different approaches of the two software packages it is necessary to briefly discuss some theoretical aspects of optical photon interaction in possible tracking volumes: Rayleigh scattering and interaction at boundaries.

### 5.1.1 *Rayleigh scattering*

The Rayleigh scattering is the elastic scattering of light or other electromagnetic radiation by particles much smaller than the wavelength in exam. It can be described in a classical way as a result of electric polarizability of particles. The particle indeed behaves as a small radiating dipole as the electric field of the light wave acts on the charge. We just here quote the Rayleigh cross section, which is

$$\sigma_{Rayleigh} = \frac{2\pi^2}{3} \frac{d^6}{\lambda^4} \left( \frac{n^2 - 1}{n^2 + 2} \right)^2 \quad (5.1)$$

where  $\lambda$  is the wavelength,  $d$  is the characteristic size of the scattering center and  $n$  is the refractive index of the medium. It is not evident to identify scattering processes inside heavy scintillator crystals as Rayleigh interactions and this is beyond the scope of this work. Nevertheless the toolkits analyzed and used in this study specify a scattering length of Rayleigh processes, and this is necessary to account for scattering inside the bulk, which, as will be seen by measurement performed, is of foremost importance.

### 5.1.2 *Model for surface interactions*

Surface interaction proved to be quite hard to model. As a photon hits a boundary, it can be absorbed, transmitted or reflected depending on the materials at the two sides of

the boundary. This involves optical properties, such as the index of refraction and the absorption coefficient as well as surface properties of the material, such as roughness or shape. Modelling these parameters, and obtaining them via measurements is quite difficult, and ray tracing softwares often implement effective models, with limited applicability. In addition, crystals may present anisotropic properties, thus requiring the implementation of wave models rather than simple particle tracking. In this study we will not consider such a property, and in the case of small pixels it can be usually neglected Cucciati (2013).

A simple solution is the definition of border surfaces as ordered pairs of physical volumes. In case of simple polished surfaces between two dielectric materials, the only relevant property is the index of refraction. In case the surface is painted or wrapped the definition may include the index of refraction of the thin layer. This allows for lambertian (diffused) or specular refraction to take place at the back of the layer. By defining combination of surface finish properties it is possible to grossly model the experimental conditions.

A more refined though incomplete solution implements the so called UNIFIED model. It is usually defined for dielectric-dielectric interfaces and it considers the surface to be made up of micro-facets with normal vectors that follow given distributions around the nominal normal for the volume at the impact point.

This models are implemented in SLitrani and Geant4, but given the limited applicability due to lack of data about surfaces, only more simple approaches have been evaluated, modeling reflection at boundaries as lambertian or specular at the expenses of accuracy.

## 5.2 Geant4

Geant4 is a toolkit for simulating the passage of particles through matter, based on C++ language. It includes a comprehensive range of features, including electromagnetic, hadronic and optical processes, a large set of long-lived particles, materials and elements from hundreds of eV to the TeV scale. An analysis of Geant4 extended capabilities is beyond the scope of this work, a review can be found in et al. (2003). For what concerns optical photons production and ray tracing a brief introduction is given below.

### 5.2.1 Physics

An optical photon is characterized by a wavelength much greater than the typical atomic spacing. In Geant4 optical photons are treated as a separate class, so to include wave-like properties into the processes. Since the description breaks down at higher energies, there is no smooth transition as a function of energy between the optical photon and  $\gamma$  particle classes. Ray tracing in Geant4 has the following characteristics:

- **Energy deposition scheme:** it implements complex models for the different particles and provides for tracking of secondaries. Many different pre defined packages are included to describe processes at different energy scales, including low energy electromagnetic phenomena. In this work the G4Livermore libraries have been used, which are optimised for precise treatment of EM showers and interactions at low energy (KeV scale). They guarantee the best accuracy until 250 eV, at the cost of a more CPU-intensive simulation. Processes implemented include polarized Compton scattering, polarized photo electric effect, ionization and bremsstrahlung for electrons. A complete review can be accessed at et al. (2002).
- **Photon production stage:** optical photons may be produced via a scintillation process or a Cerenkov process. A scintillation process may be called after energy deposition in the volume. Indeed, as a secondary goes below threshold for tracking, its energy is deposited in the bulk. Given the optical parameters specified for the material (light yield, resolution scale, time profile of the scintillation, fluorescence spectrum) photons are produced isotropically with random polarization and begin to be tracked with the optical classes. The Cerenkov process, on the other hand, is called during the simulation step of the tracking of a charged particle over threshold. Frequency and number of photons produced are sampled from the Frank-Tamm formula.

When the optical photon is produced, according to the scintillation properties specified for the material, it needs to be tracked to the end of the volume or until it is under threshold

for a cut. Polarisation effect can be considered. An optical photon is canonically tracked and can undergo four distinct processes:

- **Absorption:** absorption length must be specified at different wavelength for every material where optical tracking is required. It is a simple exponential decrease in photons transmitted.
- **Rayleigh scattering:** Rayleigh scattering length must be specified at different wavelength for every material where optical tracking is required, and implements the formulas presented before.
- **Boundary interaction:** different models are implemented to describe boundary interactions. In particular Fresnel equation are always used to determine the transmission of a single photon given its wavelength, its momentum and the refractive indices of the materials at the boundary. Moreover, the UNIFIED model is implemented for boundaries with wrapping/coatings and air/grease gap. In this case when a photon arrives at a medium boundary its behavior depends on the nature of the two materials that join at that boundary. Medium boundaries may be formed between two dielectric materials or a dielectric and a metal. Reflection and transmission probabilities are sensitive to the state of linear polarization. In the case of an interface between a dielectric and a metal, the photon can be absorbed by the metal or reflected back into the dielectric. However in this study only completely diffusive and reflective wrappings will be considered, with air gap.
- **Wavelength shifting:** the user must specify the characteristic length for WLS process, the emission process and time profile. It is not usually necessary to include it in PET like systems.

### 5.3 SLitrani

SLitrani stands for Super LIght TRansmission in ANIsotropic media. It is a general purpose Monte-Carlo program, built upon ROOT ?, simulating light propagation in any type of

set-up which may be represented by the shapes provided by the geometry of ROOT. The first motivation was the characterization of the PbWO<sub>4</sub> crystals of the ECAL detector at the CMS experiment. As more deeply discussed in Gentit (2002), this crystalline species presents high anisotropy and needs to be accounted for given the size and geometry of the experiment.

### 5.3.1 Physics

Similarly to what happens in Geant4, optical photons are treated as a separate class with respect to high energy particles, so to include wave-like properties into the processes.

- **Energy deposition scheme:** includes very basic electromagnetic models for low energy  $\gamma$ , comprehending Compton scattering and photo electric effect. Coherent scattering is not implemented. Scattered electrons are not tracked: all the energy of the scattered electron emits light at the vertex position where the Compton scattering occurred. The cross section for Compton scattering is calculated analytically from the atomic properties of the material. The photoelectric cross-section must be provided by the user. In the case of beam of particles, energy deposition is sampled from the  $dE/dx$  for the specific material.
- **Photon production stage:** scintillation occurs when a particle deposits energy in the bulk. So this is affected by the mechanisms previously outlined and the specified characteristics of the material (light yield, resolution scale, time profile of the scintillation, fluorescence spectrum). Cerenkov effect may be switched on for particle beams. In this case providing index of refraction  $n$  and thickness of material fixes all parameters affecting the generation of Cerenkov light, namely emission and number of photons emitted. They are produced with respect to the axis of the beam, without tracking of secondary particles.

As previously discussed for Geant4, an optical photon after production is tracked. In the case of SLitrani the tracking is canonical except for boundary interaction, where a wave-

like approach is implemented, based on Maxwell equations, thus accounting for anisotropy effect. In this work these effects are not taken into account, and only the case of isotropic crystals is considered. However, as shown in Cucciati (2013) the influence on light collection for small pixels is not significative.

- **Absorption:** the management of the process is similar to the one of Geant4, given the input values specified by the user
- **Rayleigh scattering:** the management of the process is similar to the one of Geant4, given the input values specified by the user
- **Boundary interaction:** SLitrani implements boundary interaction models similar to those of Geant4. There are some differences at a level of the reflection/absorption in the UNIFIED approach that will be quantified in the next section. The main difference intervenes in the case of anisotropic crystal, where the dielectric tensor is considered, thus accounting for reflections on the different optical planes.
- **Wavelength shifting:** the management of the process is similar to the one of Geant4, given the input values specified by the user

#### 5.4 A comparison for timing simulation

Since this work is more concerned with the timing implications of detection at low energies, this is the domain where the analysis will be restricted. In this case the main difference between the two software packages comes with the possibility of tracking secondary particles. In SLitrani the energy deposition models are very simple: scintillation occurs as soon as a photo electric or Compton interaction involves the  $\gamma$  quantum. In the case of Geant4 the implementation, as already seen in the previous section, is more complex. An impinging photon deposits energy in the lattice and frees an electron which is able to travel and further ionize the medium. This implicates that the energy deposited by a quantum in a Geant4 simulation will have a higher spatial spread. This is shown in figure 5.1, where

the longitudinal and transversal energy deposition of 511 KeV  $\gamma$  interacting inside a LSO scintillating crystal of  $2 \times 2 \times 20$  mm $^3$  is compared for the two softwares. Moreover, secondary electrons of non negligible energy in terms of Cerenkov threshold, can be tracked and photons tracks produced can be simulated. Giving the fact that typical values for light yield

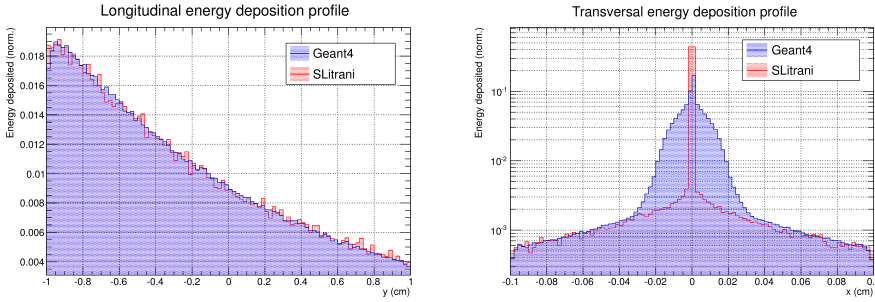


FIGURE 5.1: Comparison between energy deposition maps in SLitrani and Geant4 (longitudinal and transversal)

of heavy scintillating crystals are around a few tens of thousands photons per MeV, the smearing effect of energy deposition can often be neglected. The same goes for the small amount of Cerenkov photons produced with respect to the number of photons extracted and the subsequent resolution effect.

Nonetheless, as already discussed in the previous chapter, a small but significant impact can be found as soon as timing properties of crystals are taken into account.

#### 5.4.1 Cerenkov photons for low energy excitation

The direction of the Cerenkov photons produced can be neglected, and it retains no value, since the information is completely washed out by the typical path of a low energy electron in the crystalline lattice. As shown in figure 5.2 the path of the electron is tortuous due to the large cross section for multi scattering processes.

FIGURE 5.2: Example of path of electron in a LSO: Ce lattice according to Geant4 libraries

On the other hand the first question to be answered when evaluating the impact of

Cerenkov photons on time profiles of crystals concerns the number of photons extracted. It has been shown in chapter 2 that the number of photons produced for different crystalline spacies may be relevant. In order to estimate an order of magnitude for the number of photons collected at the exit window of the detector, a simulation was performed in Geant4 using the low energy Penelope libraries. The setup is a simple 2x2x3 mm<sup>3</sup> crystal hit by a 511 KeV  $\gamma$  particle. The choice of the sample size was based on the typical experimental conditions in our laboratory. At this stage, the condition were kept as simple as possible, thus including only Fresnel processes and absorption: the crystal is not wrapped and surrounded by air, the coupling medium to the photo detector is air.

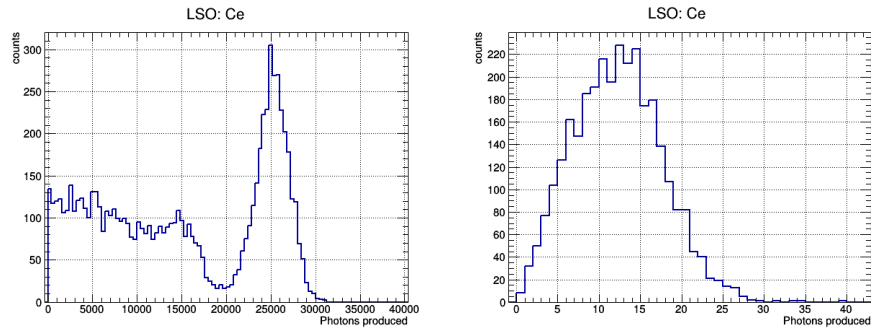


FIGURE 5.3: Photon production for scintillation processes (left) and Cerenkov production (right)

As shown in figure 5.3, the number of Cerenkov photons, which dependes essentially on the density and refractive index of the medium is in substantial agreement with the theoretical calculation, provided the statistical spread. A good deal of attention should be posed on the fact that this photons are, at the moment, produced, in the range of the scattered electron. The number of photons coupled out is substantially reduced by three factors:

- the reduced cone of extraction due to the matching of refractive indices (air-crystal)
- the transmission curve of the crystal
- the quantum efficiency of the photo detector

For what concerns the refractive indices of the materials simulated, values were taken from et al. (2009), et al. (2004a), Jellison (2012). The quantum efficiency influences selectively the photons extracted, thus influencing the ratio between scintillation and Cerenkov photons. Indeed a photo detector more efficient in the UV would collect a higher number of Cerenkov photons. For this preliminary result a standard photo cathode quantum efficiency has been considered, between 200 and 1000 nm. Finally the transmission curve allows only certain wavelengths to be transmitted due to the absorption by the luminescence centers of the crystal. The values used have been measured for samples on the crystalline species used with the method outlined in the next sections.

Crystal	Calculated	Produced	Collected
LSO: Ce	15	12.1	1.4
PbWO <sub>4</sub>	21	18	4.1
LuAG: Ce	25	20	6
CeF <sub>3</sub>			
BGO	23	25	3.2

Table 5.1: Example of Cerenkov photons calculated and simulated (produced and collected) for different crystalline species

As already said this small number can be neglected in most cases: as shown in the previous chapter their role becomes less and less relevant as the time constants of the crystal get fast. For main scintillators photons produced and collected are shown in table 5.1. This is in agreement with previous studies, such as et al. (2014).

In particular they are negligible when the ratio between Cerenkov photons collected and scintillation photons collected becomes low. In this case most of the photons collected come from a scintillation event. When dealing with PET like setups one should also take into account the fact that selection on the photopeak usually is mandatory for improving the signal to noise ratio. This changes also the ratio between Cerenkov and scintillation photons, since it is much more likely for a photoelectric event to couple out a Cerenkov photon produced by the secondaries. In the analysis run in the last chapters this will not be completely true since no selection will take place.

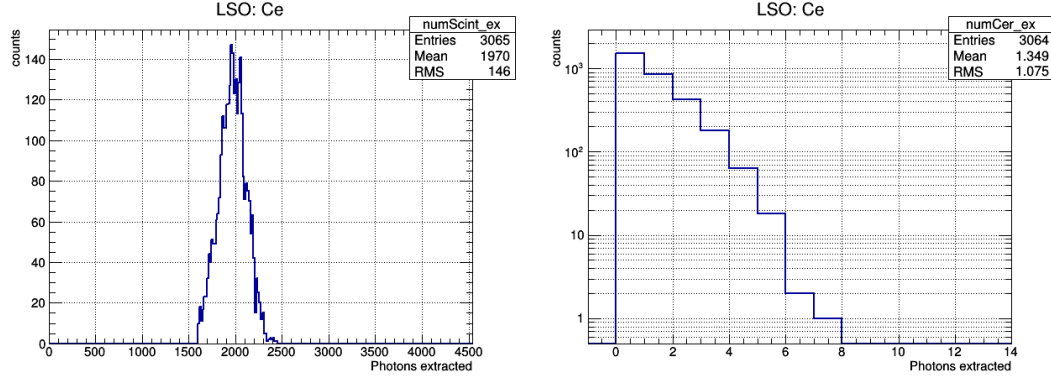


FIGURE 5.4: The spectrum is selected on the LSO photo peak (left) and the number of Cerenkov collected changes slightly (right)

As a final remark it is interesting to underline the timing characteristics of the Cerenkov spectrum. Indeed these photons are produced promptly and they can influence, albeit slightly, the time resolution. They can especially change the way we set thresholds on events. As shown in figure 5.5 in the first 100 ps a relevant part of the photons collected is taken by scintillation photons. This means that they can not be completely neglected.

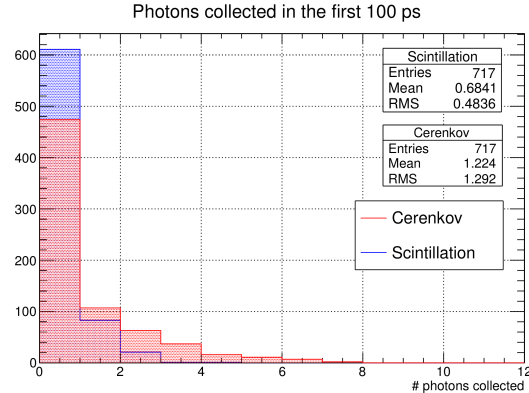


FIGURE 5.5: The Cerenkov photons collected in the first 100 ps are comparable to the scintillation collection.

#### 5.4.2 Rise time model

The rise time model implemented in Geant4 is very simple, and given the energy deposition map in the crystal volume very similar to that of SLitrani. As soon as the program calls

for energy deposition in a specific point, below the cut value set for the simulation, the scintillation process is called. At this point a bunch of isotropically distributed photons is produced, with the time profiles specified for the material. All the parameters are defined at input: light yield (photons per MeV), energy resolution scale, scattering length, absorption length, index of refraction, fluorescence spectrum.

In terms of timing, the LiverMore/Penelope libraries allow for reliable tracking down to 250 eV. This means that the time scale that divides this level of energy (tens of times higher than the band gap of heavy scintillators) to the recombination stage is included in the rise time parameters. Thus there is no model describing thermalization stage, that is all the chain of processes that leads electron hole pairs to recombine at luminescent centers. Attempts to include this stage in a simulation frame have been performed separately, see for example the work presented Vasily (????).

As a consequence, simulations allow for good modelling of processes taking place above the ionization threshold and until the lower bound of multiscattering processes in low energy electromagnetic libraries. Moreover, as soon as the production of photons takes place with the parameters plugged in for the specific material in use, photons are tracked according to the optical characteristics of the material.

This happens for the two software packages, but SLitrani does not account for Cerenkov events. As shown in figure 5.6 this events account for a large part of the rising edge of the signal, thus making Geant4 the ideal choice for simulations concerning timing.

FIGURE 5.6: Simulated time profiles for LSO in SLitrani (left) and Geant4 (right)

#### *5.4.3 Absorption and surface treatment*

Optical photons generated inside a crystal may undergo absorption processes (in the bulk or at a surface) and boundary interactions before being extracted or killed. In order to test the differences between the softwares these events were tested with specified input

parameters for absorption length and surface characteristics. For absorption lenght optical photons were generated by a monochromatic source in the center of a very extended crystal. Reflaction and refraction coefficients, on the other hand, where tested with a monochromatic beam of photons from the center of the crystal towards an interface with air.

The ratio of results obtained in SLitrani and Geant4, for LSO demonstrate perfect agreement between the two Monte Carlo software as shown in figure 5.7, both for Fresnel interaction and absorption processes. The parameters for the simulations were extracted with the procedure described in the next section.

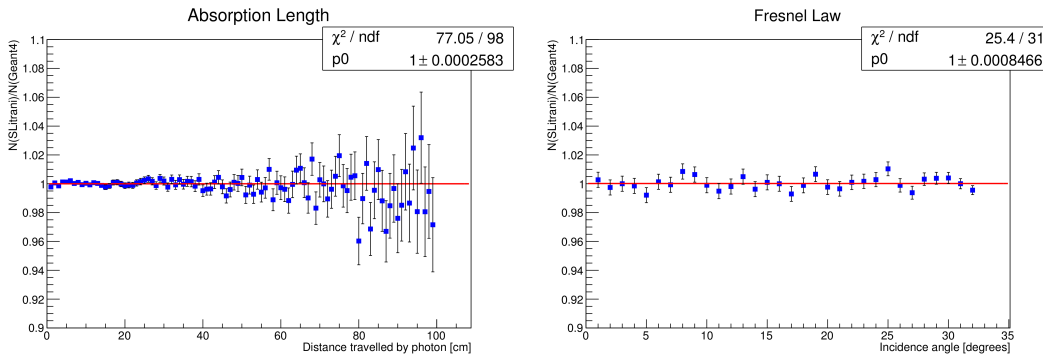


FIGURE 5.7: Ratio of photon absorbed in the simulation cnfiguration (left) and ratio of photons reflected at different angles (right).

In order to test the models for boundary interaction with wrappings or coatings, the absorption of photons at boundary interface was tested by firing a monochromatic beam of photons towards the surface boundary and varying the incidence angle. The results obtained for the two software are shown in figure 5.8. A significant difference is found for diffusive wrappings, with SLitrani showing an higher absorption rate for high incidence angles. This is due to the different modelization of the absorption at boundaries. In fact, Geant4 determines the reflection based on the extracted value of the facet before the tilting considering an average value, while SLitrani does it for every angle.

In order to evaluate the photon extraction efficiency in a realistic setup, a LSO crystal was simulated with an internal isotropic photon source, with a glass sensor placed with

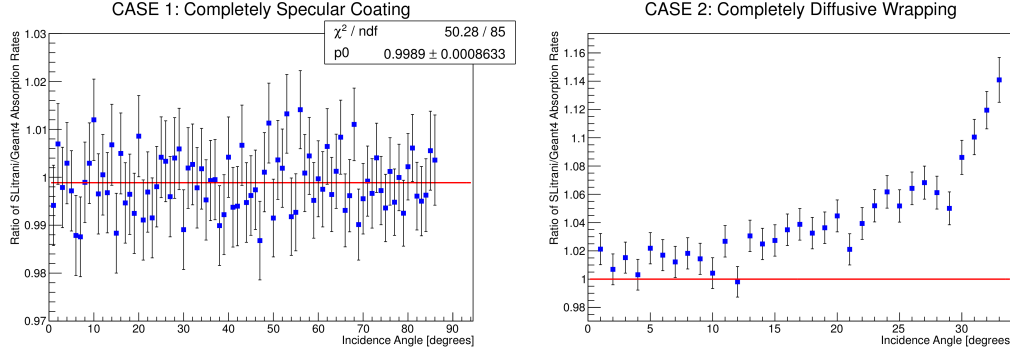


FIGURE 5.8: Ratio of photons reflected for completely specular coating (left) and completely diffusive wrapping (right)

air gap from on of the exit faces. Keeping a fixed cyrstal length (20 mm) while varying transverse section (from  $0.56 \text{ mm}^2$  to  $16 \text{ cm}^2$ ), the difference in the softwares were assessed for different surface states (wrapping, coating, depolishing) and crystal coupling to the detector (air and optical grease). The results obtained for Teflon wrapping as a completely diffusive material are shown in figure 5.9. As already inferable form the results in figure 5.8, a significative difference in photon extraction efficiency is found for small crystals. It is possible to conclude that as the crystal section decreases, more bounces on the lateral faces are necessary for extraction. As SLitrani considers a higher absorption probability on the wrapping a discrepancy is measured. This results, though, seem to back the idea

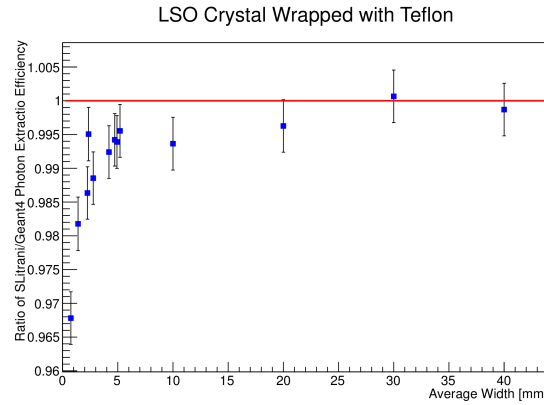


FIGURE 5.9: Ratio of photons extracted for different aspect ratio of the crystal simulated.

that a satisfying model for boundary interaction is still lacking.

In fact, as a preliminary comparison with experimental data, the values measured in the study et al. (2012) were considered, since full access to the experimental setup and materials was possible. The comparison was performed on the gain in the extraction coefficient obtained by coupling the crystal to a PMT with optical grease and by wrapping it with Teflon. The gain profile given by the grease was qualitatively reproduced, as shown in figure 5.10. The systematic difference is due to poor knowledge of the optical grease index of refraction. On the other hand, the gain profile due to the use of Teflon wrapping, is significantly different between experimental data and Monte Carlo simulations, as shown in figure 5.10. Given this poor modeling of surface interaction we relied mainly on the simplest

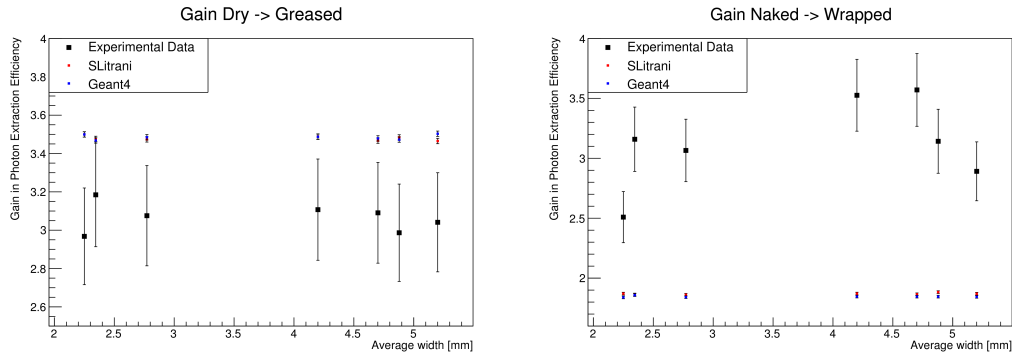


FIGURE 5.10: Gain profile for the two software with respect to the measured data for grease coupling (left) and Teflon wrapping (right).

models available for the softwares, that is polished surface and lambertian wrapping. No significative inferences can be made on light extraction, so timing simulation were tuned on parameters measured separately.

For the analysis of the measured data, we will make use of Geant4 in order to disentangle the elements contributing to signal formation in a scintillator system, since SLitrani does not offer the same processes in terms of photon production. These three stages will be considered as the main components of the rising edge: energy deposition above the ionisation threshold, thermalization phenomena, photon coupling.

## 5.5 Simulation input parameters

It has emerged from the previous discussion that the time scales involved in the de-excitation phases following a  $\gamma$  event in a crystal, become relevant at the thermalization stage. This emerges also from simulation packages at the KeV scale. After photon production optical tracking inside the volumes takes place. This stage can be more and more important as the volume of the crystal grows, because scattering and absorption in the bulk start to importantly degrade the performance of crystals in terms of light collection. In order to properly describe this chain of processes and disentangle the various contributions that lead to the spread of the inference on the time of interaction, it is thus necessary to measure the input parameters of the crystals. For what concerns refractive indices the values previously introduced from literature were considered, since no direct method was available to measure them. Four parameters were then accessible to experimental assessment: light yield, excitation spectrum, emission spectrum, transmission curve. The samples measured to obtain input parameters for Monte Carlo simulation were later characterized with  $\gamma$  excitation as explained in chapter nine

- LuAG:Ce (0.13%)
- LYSO (Sipat)
- LYSO (Proteus)
- LSO:Ce,Ca
- LSO:Ce (CTI)
- BGO
- CeF<sub>3</sub>

### 5.5.1 *Fluorescence spectrum*

In order to analyze the timing profiles of crystals measured and plug in the correct parameters for simulations, the energy levels of the samples were investigated with a spectro

fluorimeter.

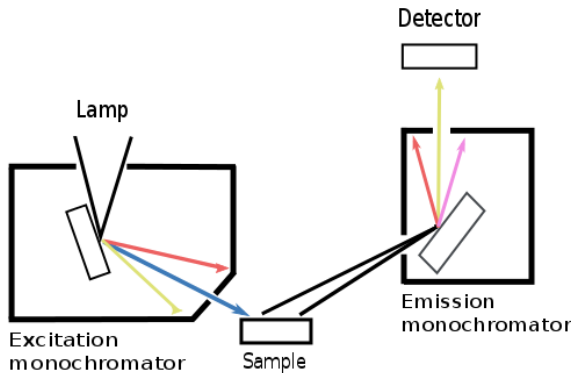


FIGURE 5.11: The setup used to measure excitation and emission spectra of the samples

As shown in figure 5.11 a light source (typically Xenon based) is used to generate photons over a certain range (200 nm - 800 nm) and two monochromators allow to select both the excitation and the emission wavelengths. Given a certain excitation wavelength it is then possible to measure the emission spectrum of the sample considered. It is also possible to select a certain wavelength of emission and measure the excitation spectrum of the same sample. Emission and excitation spectra of a LYSO (Sipat) and a LuAG:Ce crystal are shown in figure 5.12. The LSO, LGSO, LSO:Ce,Ca crystals do not qualitatively differ in terms of emission and excitation from the sample shown. The large bands are due to relevant electron-phonon coupling at higher temperatures. The excitation spectra for the Cerium doped samples show the absorption peaks at 300 nm and 350 nm, associated with the Cerium sites absorption presented in chapter 2. The  $5d \rightarrow 4f$  transition is responsible for the typical emission band of the Cerium doped LSO and LuAG crystals. In the case of LuAG:Ce only the Cerium emission is investigated since for UV emission the instrumentation is not optimised.

The LuAG:Pr. excitation and emission spectra are shown in figure 5.13. The transition responsible is the  $5d \rightarrow 4f$  for Praseodymium sites. For what concerns the CeF<sub>3</sub>...

The BGO emission and excitation spectra are shown in figure 5.14. The transition responsible is the Bi<sup>3+</sup>  $6s6p(P_1) \rightarrow 6s^2(1S_0)$ .

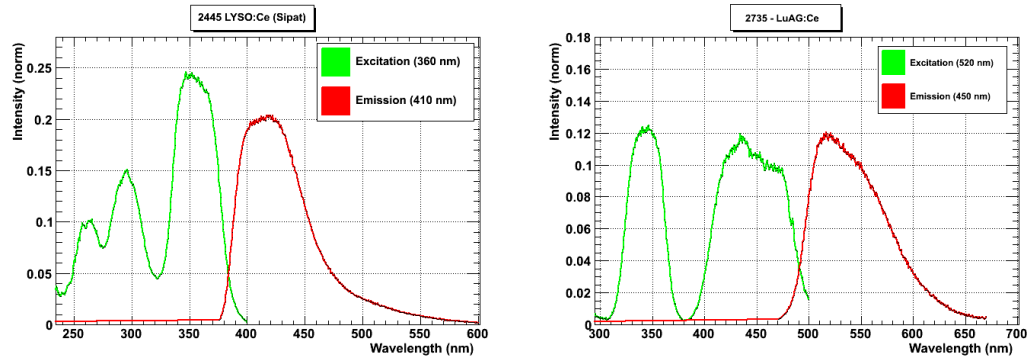


FIGURE 5.12: Measured excitation and emission spectra for LYSO Sipat an LuAG: Ce

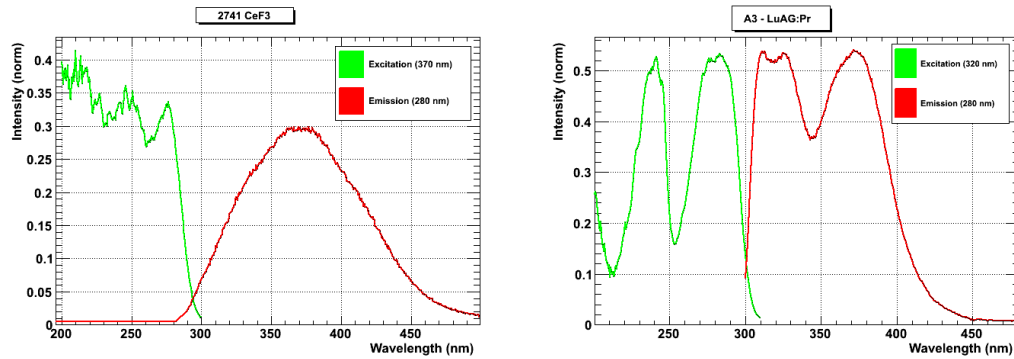


FIGURE 5.13: Measured excitation and emission spectra for CeF<sub>3</sub> an LuAG: Pr

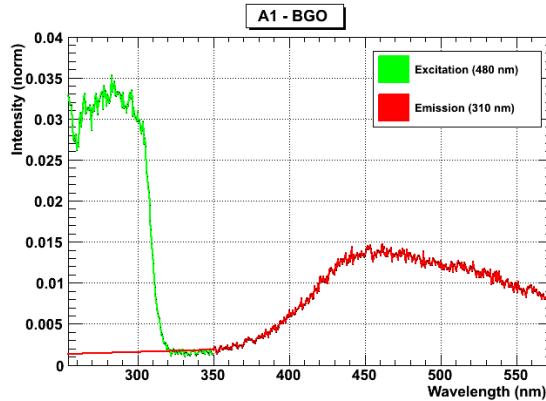


FIGURE 5.14: Measured excitation and emission spectra for BGO

### 5.5.2 Optical transmission

The next parameter analyzed to extract the inputs for the simulations was the light transmission of the samples measured. In order to extract meaningful values transmission spectra were measured for samples of different size, since the error is more significative when dealing with small pixels. The working principle is shown in figure 5.15. The sample is

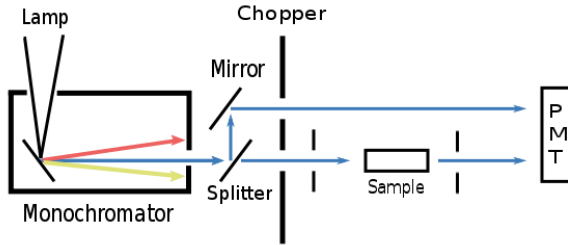


FIGURE 5.15: The setup used to measure the transmission curves of the samples

crossed by a monochromatic beam of light. Before reaching the sample the beam is split, so that at the photodetector it is possible to compute the different intensities. This allows to measure the absorption length of the crystal at the different wavelengths. The measurement determines the strength of the interactions of photons with the crystal. In general they will change the direction of diffusion, isotropically. Therefore, with a pinhole at the exit only non interacting the photons are coupled to the photo detector.

In the case of a perfect crystal, without impurities in the bulk and with perfect surface conditions the theoretical transmission at long wavelength still does not reach 100%. This is due to Fresnel refraction, since at a boundary air-crystal the reflection coefficient is

$$r = \left( \frac{n_1 - n_2}{n_1 + n_2} \right)^2 \quad (5.2)$$

where  $n_1$  and  $n_2$  are the indices of refraction of the two media. The transmission coefficient is defined as  $t = 1 - r$ . So this should be considered in the spectra presented below. Including Fresnel effect is it possible to calculate the theoretical transmission as

$$T_{theory} = \frac{t^2 \exp(-L/\tau_{att})}{1 - r^2 \exp(-L/\tau_{att})} \quad (5.3)$$

where  $L$  is the length of the material and  $\tau_{att}$  is the attenuation coefficient of the medium. Starting from the transmission value measured, we can extract the attenuation values for simulation with the approximation

$$\frac{1}{\tau_{att}} = -\frac{1}{L} \log \frac{T_{meas}}{t} \quad (5.4)$$

and  $t$  is the transmission coefficient.

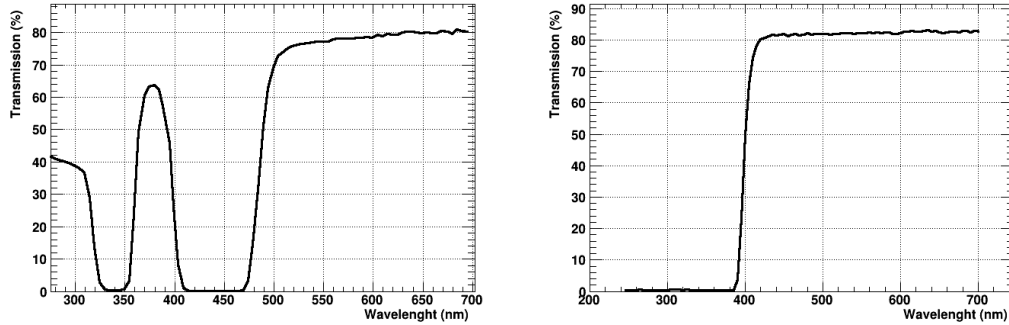


FIGURE 5.16: Transmission curve for a LuAG:Ce (left) and a LSO:Ce (right) sample.

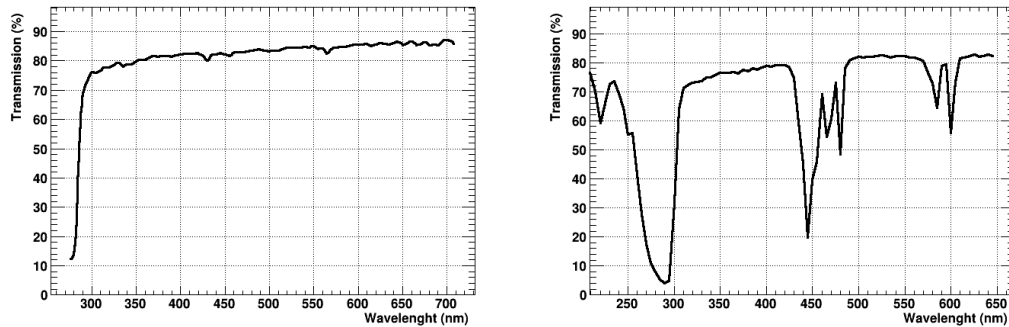


FIGURE 5.17: Transmission curve for a CeF<sub>3</sub> (left) and a LuAG:Pr (right) sample.

### 5.5.3 Light yield

The definition of light yield has been already given in chapter 2, as well as consideration on the difference between absolute light yield and light output in a specific configuration. The setup for light yield measurement is shown in figure 5.18. Teflon tape was used as a reflector,

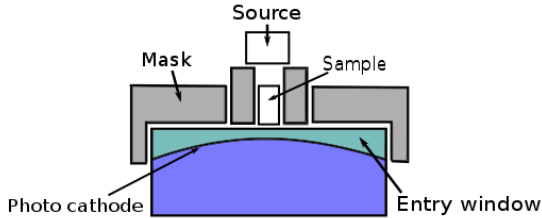


FIGURE 5.18: Set up for the measurement of light yield.

for the case of light yield measurement as well as the  $\gamma$  rise time measurement. The presence of wrapping allows to couple out more photons, and in a few cases this is necessary to infer the light output (given the low intrinsic light yield), at the cost of an inferior repeatability of the measurement. The experimental error was checked with repetition of the measurement, and estimated around 5%. The light output has been measured with a  $^{137}\text{Cs}$  source ( $E_\gamma = 662 \text{ keV}$ ) placed a few millimeters above the crystal. The system crystal-PMT was placed inside a black box, with controlled temperature ( $20^\circ\text{C}$ ) to avoid drift in the system response. Further shielding against background light was ensured by an aluminum cap covering the entry window of a Hamamatsu R2059 PMT. After the collection of the photo electrons at the anode of the PMT, the signal is attenuated, shaped and stored by the DAQ, with a digitizer *CAEN DT5720*.

To measure the light output of sample crystals the number of photo electrons  $N_{pe}$  collected can be used. In particular by computing the area of the scintillation pulse we can obtain the number of photo-electrons collected by comparison with the value of the single electron response (SER). The SER is measured exploiting the dark current of the PMT, caused by thermal emission of electrons from the photo cathode. After multiplication in the dynode system, the charge integrated is the response of the PMT to a single photo electron. The probability to emit two electrons is very low. The number of photo electrons can be calculated by comparing the position of the photo electric peak with the spectrum that characterizes a single photon emission. The number of photo electrons produced per

impinging MeV can be determined as

$$N_{pe}/MeV = \frac{\text{position photo peak}}{\text{position single photo electron peak}} \cdot \frac{A_1}{A_2} \cdot \frac{1}{E_\gamma} \quad (5.5)$$

where  $E_\gamma$  is the energy of the incident  $\gamma$  particle and linearity of the detector response is assumed. A pedestal may be subtracted from the position of the peaks.  $A_1$  and  $A_2$  are the values of the attenuation of the signal in the case of the photo peak and the single electron peak, i.e.

$$A_i = e^{\frac{B_i}{20}} \quad (5.6)$$

and  $B_i$  is the attenuation in dB. In order to extract the position of the photo peak and the resolution on the peak from the charge spectra, the sum of a Gaussian and a Fermi distribution is used for the fit:

$$y(x) = \frac{P}{e^{\frac{x-C}{R}} + 1} + Ae^{-\frac{(x-\mu)^2}{2\sigma^2}} \quad (5.7)$$

where P, C and 1/R correspond to height, position and slope of the Compton edge, A is the height of the photo peak with position  $\mu$  and FWHM width  $2.35\sigma$ . For the single photo electron spectrum a simple Gaussian fit determines the charge for the single photon with sufficient accuracy, at 1.6 pC. An example of the light yield spectrum the single photo electron spectrum are shown in figure 5.19.

At this point the number of photons extracted per MeV can be determined if the quantum efficiency of the photo detector is known:

$$N_{ph}/MeV = \frac{N_{pe}}{QE} \quad (5.8)$$

In order to determine the average quantum efficiency given a certain sample, the emission curve of the sample itself was used, and weighted by the quantum efficiency curve of the PMT (shown in figure 5.20). Finally the integration time was optimised on the time profile of the crystal measured, so that for LSO was set to 400 ns and for LuAG to 4  $\mu$ s.

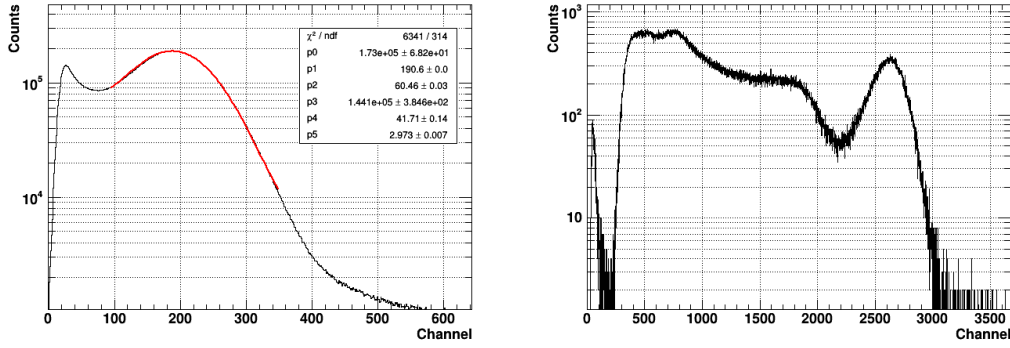


FIGURE 5.19: Spectrum fit with Gaussian for single photo electron peak (left) and  $^{137}\text{Cs}$  spectrum for LSO:Ce crystal (right)

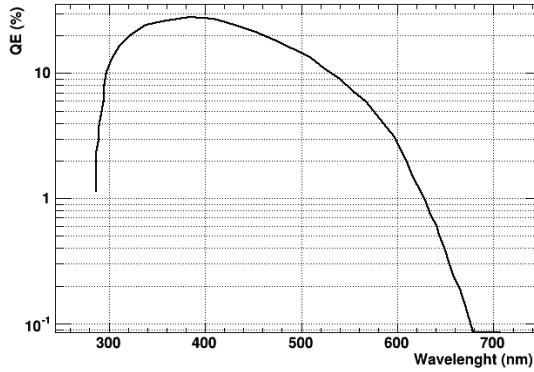


FIGURE 5.20: Quantum efficiency curve for the Hamamatsu R2059 PMT

To correct for long-term variations of the PMT gain and quantum efficiency, the light output of a reference crystal is used. In order to guarantee repeatability the crystal is encapsulated into Teflon to protect it and fix the position with respect to the photocathode and the source. The sample is a  $2 \times 2 \times 10 \text{ mm}^3$  LuAP crystal.

The samples measured and relative size are shown in table 5.5.3 along with the result obtained. Some crystals present such a low light output that it was not possible to infer the photopeak position in a naked configuration. The only available data point is with Teflon wrapping.

Crystal	L0 (Teflon)	Res (Teflon)	LO (naked)	Res(naked)	QE
LSO:Ce,Ca	8536	15	3456	16	0.22
LYSO:Ce (Sipat)	11002	15	4814	16	0.22
LYSO:Ce (Proteus)	13879	12.9	4692	17.3	0.22
LSO:Ce (CTI)	15583	11.9	5200	14	0.22
LGSO:Ce	10255	13.7	3934	14.1	0.22
CeF <sub>3</sub> 2300	26				0.22
LuAG:Ce (0.13%)					0.1
BGO					0.16

# 6

## Methods

### 6.1 Time Correlated Single Photon couting

The time correlated single photon couting (TCSPC) technique, makes use of low-level signals at high repetition rate, with the probability of detecting one photon in one repetition period being very low Becker (2005). It is then sufficient, to determine the time profile of the sample, to measure the time of arrival of single photons and build up a histogram of the photon times. The most common method to perform this measurement is a start-stop setup: some sort of trigger, correlated with the beginning of the excitation process in the sample (start), is measured in coincidence with a stop signal given by the arrival of the optical photon emitted by the sample. Thus the main components of a TCSPC system are

- an excitation system for the sample with an extracted trigger
- a fluorescent sample with a characteristics periodic light emission
- a detection system able to extract the time stamps of the arriving single photons.

The effective resolution of a TCSPC experiment is characterised by its instrument response function (IRF). The IRF contains the pulse shape of the light source used, the temporal dispersion in the optical system, the transit time spread in the detector, and the timing jit-

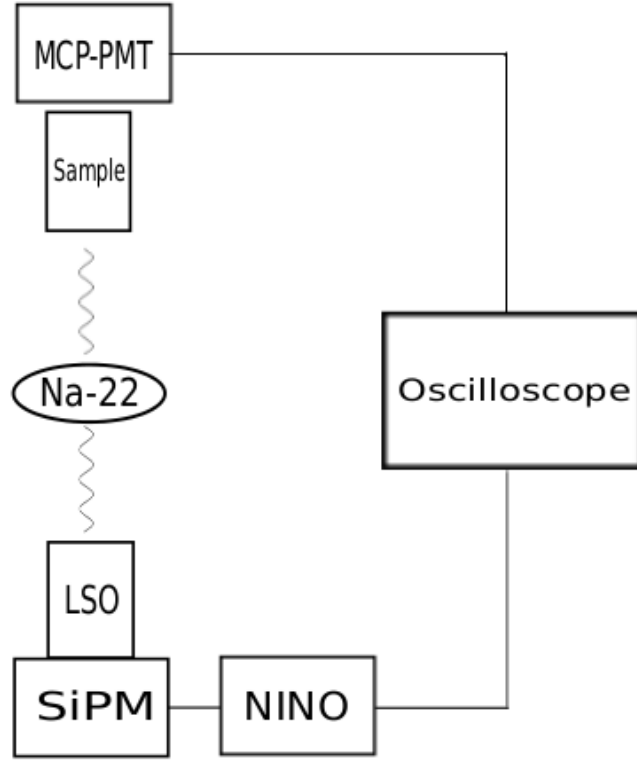


FIGURE 6.1: Principles of time correlated single photon counting (TCSPC)

ter in the recording electronics. The main sources of error and incertitude on the measured curve are presented in this chapter and can be roughly categorized as:

- the time structure of the excitation
- the single photon time resolution of the detection system
- the rate of arrival of optical photons at the stop detector
- the accumulation times: statistics

#### *6.1.1 Excitation*

In an ideal TCSPC experiment, the excitation system has a very narrow distribution in time. That is, the spread of the single particles determining the excitation of the sample is negligible with respect to the time scale of the processes under study. A variety of high time

resolution sources are available for TCSPC. In classical fluorescence studies laser sources (or laser-driven) sources are used and allow for the study of sub-ps dynamics: mode-locked Argon or Nd:YAG lasers, synchronously pumped dye lasers, or Ti:sapphire laser. For the time scales that characterize electron hole thermalization, thus signal formation, thus rise time in scintillating crystals, it is necessary to make use of a ps resolved system.

The main limitation though, comes from the excitation energy of the system, since the level of excitation is crucial in determining the physical processes that concur to give a non zero rise time. As was shown in previous chapter, the multi scattering processes that lead electrons and holes below the ionization threshold, and thus to the accuracy limit of Monte-Carlo simulations, happen on time scales which are an order of magnitude inferior to the thermalization stage. This means that in terms of physical processes not much is added to the study by raising the excitation energy above 10 time the band gap of the sample. Two different phenomena though introduce a non negligible contribution to the time spread of the rise if the signal collected.

The first one is the appearance of Cerenkov photons, above the threshold for the specific materials. Thresholds for Cerenkov effect in heavy scintillating crystals have been briefly summarized in chapter As will be diffusely discussed in this photons, though in a limited number, are concentrated in the very first portion of the time profile. This results in a modification of the rise time towards longer values. In order to disentangle this variety of effect, the sample were measured in different conditions of excitation: at a high harmonics generation facility with a 36 eV VUV radiation and in a experimental bench with a 511 KeV radiation.

A second prominent source of smearing in time profiles is the travel of photon inside crystalline samples Derenzo (2000). Indeed, depending on the type of coupling to the photo detector, photo extraction can be favoured or disfavoured at different angles. Opening this extraction cone accounts for different time profiles: a Teflon diffusive wrapping or coating for example, gives longer rise times. From the point of view of the excitation energy, though, an important difference can be found at 36 eV or 511 KeV. In the first case the

excitation is only on the surface, since the range of VUV photons in a heavy scintillator is In the case of excitation at higher energy, on the other hand, photons may travel longer distances in the lattice, and photons produced in the deep volume of the sample need to be coupled out.

### 6.1.2 Detection

Once the sample has been excited, photons are couple out to the stop detector. Tipically PMTs, MCP-PMTs or single cell APD in Geiger mode are the preferred detectors for their timing characteristics. The crucial parameter in this case is Single Photon Time Resolution (S PTR) for Silicon detectors or Transit Time Spread (TTS) for vacuum detectors. When a photocathode is fully illuminated, the transit time of each photoelectron pulse has a fluctuation. This fluctuation is called TTS (transit time spread). It is clear that in order to extract the most accurate value for the time constants of the samples measured, one should keep the incertitude component due to the detector as low as possible. In this case though, it is customary to make use of detectors optimized for single photon detection, that is with low or no energy resolution and very rapid response. For the study presented MCP-PMTs have been mainly used, since in principle they guarantee the best performance when considering acquisition rates and time resolution. As will be clear in the next chapters, this prerogative of MCPs becomes less and less attractive as the energy of the excitation grows, since it is necessary to cope with non negligible backgrounds due to the high active area. Nevertheless, given the time scale considered in this study, a response of less than 100 ps should be available in order to extract the parameters with a minimum accuracy. As will be presented in the next chapters the photo detectors chosen for this study satisfy this requirement. Many stop detectors, and this is the case of the MCPs used in the next analysis, present important amount of time walk, and often require appropriate corrections. Time walk arises when synchronous signals have different amplitudes. Time pick up methods based on threshold crossing may extract different time stamps and thus introduce a non negligible jitter, as shown in figure ??.

### 6.1.3 Stop rate and bias

When considering the geometry of the experiment, another parameter becomes crucial, the stop rate at the detector. As explained before two opposite effects tend to counteract; ideally we should keep the count rate as high as possible to have reasonable accumulation times, but the increasing of the bias fraction of counts modify the profile measured. Two techniques will be used in this study, employing a conventional TDC and a multi-hit TDC. A conventional TDC can only digitize the arrival time of the first stop signal. Therefore events that have more than one stop pulse will bias the dataset, since the later pulses will not be measured with the same probability. This will be the case of the acquisition setup presented in chapter 7. If we define the probability  $P$  that  $m$  photons are detected after a single excitation, the Poisson distribution gives

$$P(m; \epsilon) = \epsilon^m e^{-\epsilon} / m! \quad (6.1)$$

and  $\epsilon$  is the average number of stop per excitation. The probability to have an unbiased event is

$$Event_{unbias} = U = P(1; \epsilon) = \epsilon e^{-\epsilon} \quad (6.2)$$

and the probability to have a biased event is, assuming  $\epsilon \ll 1$

$$Event_{bias} = B = \sum_{m=2}^{\infty} P(m; \epsilon) \sim \epsilon^2 e^{-\epsilon} / 2 \quad (6.3)$$

The ratio of biased to unbiased event is given by

$$B/U \sim \epsilon/2 \quad (6.4)$$

The factor  $\epsilon$  depends on the combined effect of the geometry of the system, the light yield of the crystal, the quantum efficiency of the detector. In order to improve the ratio, it is

thus necessary to lower the rate at the detector by modifying the position accordingly, at the expense of reduced data collection rates.

On the other hand, in chapter 8 a multi hit approach will be proposed, that is capable of measuring the arrival of  $n$  stop pulses per start pulse. In this configuration the data acquisition rate can be increased, as the probability is:

$$Event_{unbias} = \sum_{m=1}^n mP(m; e) = \sum_{m=1}^n \frac{\epsilon^m e^{-\epsilon}}{(m-1)!} nj \quad (6.5)$$

In particular dead casad

#### *6.1.4 Statistics and accumulation times*

## 6.2 Data analysis techniques

In order to analize the start stop data collected, a classical fitting approach was used, based on maximum likelihood principles. With respect to this statistical and systematic contribution to the error were estimated, based on the previous discussion. In particular the iterative reconvolution approach has been used, being the most powerful and widespread in the field of fluorescence lifetime measurements.

### *6.2.1 Iterative reconvolution*

In time correlated single photon counting experiments the problem at hand is statistically speaking to estimate or more parameters (the lifetimes) from a dataset.

The maximum likelihood method is considered to be the most powerful method of parameter estimation. Consider  $n$  independent observations (counts in this case)  $c_1, \dots, c_n$  and a vector of parameters  $\theta = (\theta_1, \dots, \theta_m)$ . If the probability of having the observation  $i$  is  $p(c_i|\theta)$ , the likelihood function is

$$L(c_1, \dots, c_n | \theta) = \prod_{i=1}^n p(c_i | \theta) \quad (6.6)$$

The Maximum Likelihood method provides then an estimate of the true parameters' value as the vector  $\hat{\theta}$  that maximizes the likelihood function. In the case of time correlated

single photon counting it is natural to assume that the observed counts  $c_i$  follow a Poisson distribution

$$p(c_i|\theta) = \exp(-\langle c_i \rangle) \frac{\langle c_i \rangle^{c_i}}{c_i!} \quad (6.7)$$

where  $\langle c_i \rangle$  is the expected value of the number of counts in the i-channel. This expected value is given by the model taken in to consideration: in this case we can make use of the equations obtained in chapter 3. The pdf for the time stamps is given by

$$p_{t_n}(t|\theta) = A \cdot \sum_i \frac{S_i}{\tau_{d,i} - \tau_{r,i}} \cdot [a_{\tau_{d,i}}(t|\theta) - a_{\tau_{r,i}}(t|\theta)] \quad (6.8)$$

where

$$a_\tau(t|\theta) = \frac{1}{2} \exp\left(\frac{\sigma_{SPTR}^2 - 2t\tau + 2\theta\tau + 2t_{TT}\tau}{2\tau^2}\right) \quad (6.9)$$

$$\cdot \left[ \operatorname{erf}\left(\frac{t - \theta - t_{TT} - \frac{\sigma_{SPTR}^2}{\tau}}{\sigma_{SPTR}\sqrt{2}}\right) + \operatorname{erf}\left(\frac{t_{TT} + \frac{\sigma_{SPTR}^2}{\tau}}{\sigma_{SPTR}\sqrt{2}}\right) \right] \quad (6.10)$$

Thus the expected number of counts for the i-channel is

$$\langle c_i \rangle = \int_{(i-1)\Delta}^{i\Delta} p_{t_n}(t|\theta) dt + b_i = g_i(\theta) \quad (6.11)$$

where  $\Delta$  is the time channel width and  $b_i$  accounts for the average number of dark counts in the channel i. The vector of parameters  $\theta$  is given by the lifetimes  $\tau_i$ , the relative intensities  $S_i$  and a zero time shift  $\delta$ . It is customary to determine the best estimate for  $\theta$  by minimizing the function  $-ln(L)$  since the log-likelihood function attains its maximum for the same value as the likelihood function. In the specific case the function to minimize is

$$-Ln(L) = -\prod_{i=1}^n \exp -g_i \frac{g_i^{c_i}}{c_i!} = \sum_{i=1}^n -g_i + c_i \ln(g_i) - \ln(c_i!) \quad (6.12)$$

which is equivalent to minimizing the Poisson devianceBajzer (1991)

$$f = \sum_{i=1}^n -g_i + c_i \ln(g_i) \quad (6.13)$$

The standard function minimized in standard fluorescence analysis is usually the  $\chi^2$  defined as

$$\chi^2 = \sum_{i=1}^n \frac{[c_i - g_i(\theta)]^2}{c_i} \quad (6.14)$$

or, in the modified least square methodBajzer (1991)

$$\chi_m^2 = \sum_{i=1}^n \frac{[c_i - g_i(\theta)]^2}{g_i} \quad (6.15)$$

When the number of counts is large they are numerically very close, since the Poisson distribution can be approximated by the Gaussian. Nevertheless in the data analysis the maximum likelihood estimator will be used, since it is preferable the more the low-count region of the decay influences the estimated parametersBajzer (1991).

### 6.2.2 Sources of error

## 6.3 Simulations

# 7

## VUV measurement

The measurement performed in this chapter were possible thanks to the network LaserLab, a consortium that brings together thirty institutions in laser-based disciplinary research from sixteen countries. In particular it was granted access to the CELIA beamline in Bordeaux. CELIA (Centre Lasers Intenses et Applications) is a joint unit between the University of Bordeaux, the CEA (Commissariat l'energie atomique et aux nergies alternatives) and the CNRS (Centre national de la recherche scientifique). It provides experimental access to femtosecond lasers at high frequency and VUV harmonics production. The aim of the study is to characterize the rise time profiles of scintillating crystals at VUV energies.

As pointed out in chapter 5, the energy of the excitation of a fluorescent sample strongly influence the processes in the excitation region. At the order of the band gap of the crystal, broadly speaking one photon is able to create a isolated electron hole-pair. As the energy of the excitation grows, more of this holes are created by a single quantum and different processes interact in the formation of the signal, such as electron-electron scattering. As the energy grows above hundreds of electron Volts, mainly core absorption occurs. Above a certain threshold Cerenkov events may allow to collect more photons at the rising edge of the signal. Investigation of interaction mechanisms requires sources with different energies and different geometries. In this chapter a study with VUV radiation is presented. High-

order harmonics generation by interaction of an intense laser field with atoms provides ultrashort pulses (2-3 ps) in the VUV (few tens of eV) region at high frequencies ( $\geq 1$  kHz). Under such pulse energy, a region of high excitation density is created in the crystal, since the photons interact in the first 100 nm of material. Moreover the detector geometry will allow to focus the study on scintillator pulse, excluding any volume effect.

## 7.1 High Harmonic Generation

When an atom is exposed to a strong laser field it can absorb a large number of photons through non linear processes. This energy can be transferred back to the photon field. The phenomenon of high order harmonic generation of a laser field is a nonlinear effect that results in the emission of photons of frequency multiple of the source frequency. For example a rare gas traversed by a sufficiently power laser field may give rise to harmonic generation.

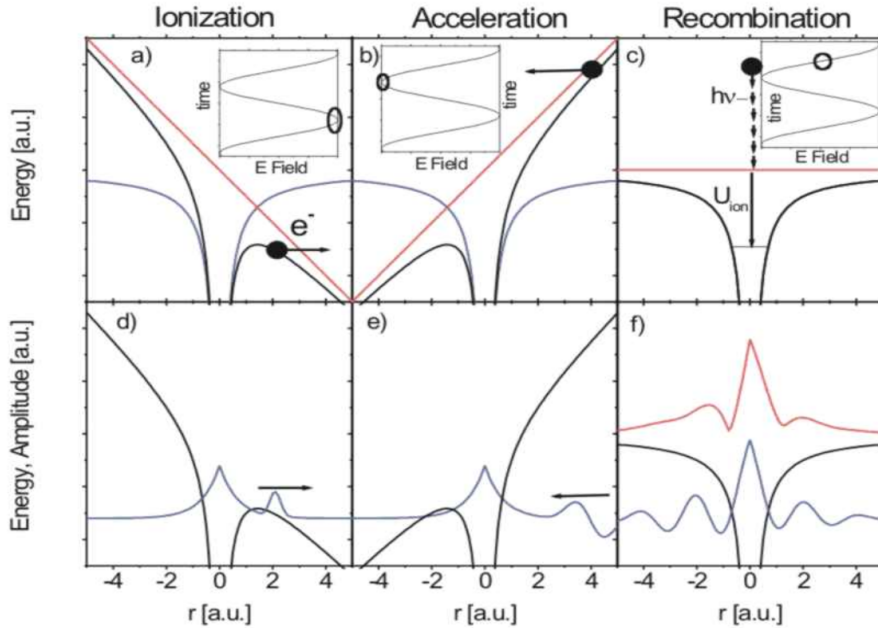


FIGURE 7.1: Phenomenology of High Harmonics Generation in a semi-classical (top) and quantum wave (bottom) approach

In figure 7.1 the main details of the high harmonic generation process are summarized,

in a semi-classical configuration and as a quantum wave process. If the laser field is strong enough ( $\sim 10^{10}$  V/m), it can allow the electron to tunnel through the barrier. The electron itself sits unperturbed in the well until the field of the laser sums to the atom potential bending it. The electron gets accelerated in the laser field and it can recollide with the atom itself. The electron kinetic energy is then transferred into photons. The cut-off energy can be calculated by examining the maximum energy the ionized electron can gain in the electric field of the laser, that is

$$E_{max} = I_p + 3.17U_p \quad (7.1)$$

where  $U_p$  is the ponderomotive energy from the laser and  $I_p$  is the ionisation potential. The recollision leads to the emission of a very broad light spectrum. The ionization and recollision happen on each half cycle of the laser pulse, and the spectra are added coherently. As a consequence the spectrum is structured in odd harmonics. High harmonics constitute a source of soft X-rays that retains the time characteristics of the driving laser, in terms of bunch structure and repetition rate. The harmonic cut off varies with the laser intensity up to saturation. The saturation intensity depends on atomic species of the noble gas used as a medium to produce the harmonics.

## 7.2 Experimental setup

The setup available at CELIA is presented in Martin (2001). it will be briefly described here. The line is organized in two different room. A first room is devoted to the laser amplification system, while in the experimental room the high harmonics are produced.

### 7.2.1 *Laser beamline*

The AURORE beamline is based on a amplified Ti-sapphire femtosecond oscillator. The Ti-sapphire oscillator generates 30 fs pulses, at 1 nJ and a frequency of 80 MHz. Before amplification the pulses are stretched up to 280 ps for optical power reasons. The regenerative pre amplifier brings the energy of the beam to 700 J at 1 kHz. The beam is then amplified in a Ti:sapphire crystal pumped by four synchronised Nd:YLF lasers at 532 nm

and 15 W. At the end of the amplification chain the laser beam delivered has a power of 10 W for 170 ps and it is sent to the experimental room.

### 7.2.2 VUV line

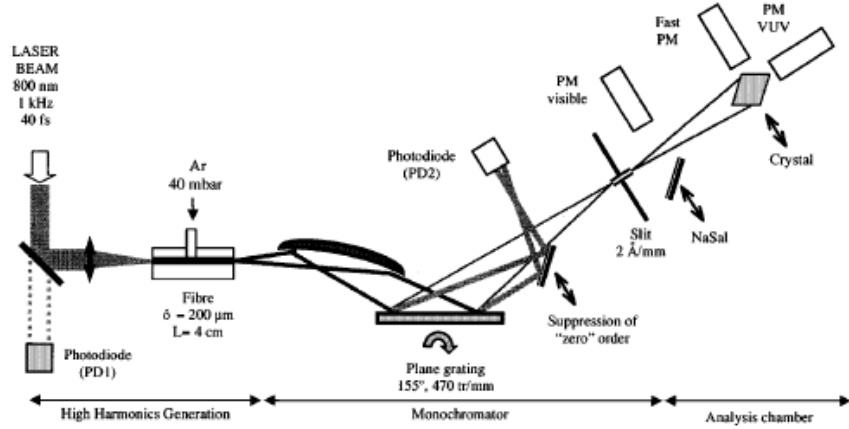


FIGURE 7.2: Schematics of the VUV line at CELIA Bordeaux

Before high harmonic generation the beam is compressed again down to 35 fs, centered around 800 nm at 1 kHz, with an energy of 4 mJ. A schematic of the HH VUV beamline is presented in fig The elements are under vacuum at a pressure of  $10^{-6}$  mbar. The beam is focused in the fiber containing the gas (200 $\mu$ m in diameter and 4 cm length). Depending on the gas used and the pressure condition the energy of the harmonic lines and the efficiency of the process may vary. Tipically in Argon/Neon the energy of the harmonics is between 10 eV and 120 eV. The fundamental beam and the harmonics spread at the exit of the fiber and are sent to the monochromator where a toroidal mirror and a plane grating (470 lines/mm) focuse the selected wavelength on the exit slit. The zero order is suppressed by a plane mirror at an angle tuned on the grating system. The desired VUV-XUV beam selected in energy is then directed to the sample placed in a vacuum chamber. Due to the dispersion by the grating the output pulses are stretched in time, and they have been measured with a VUV-streak camera to be 2-3 ps FWHM.

### 7.2.3 Detection system

The light produced by the luminescent sample hit by the VUV-XUV radiation is collected by an optical fibre visible-UV of 0.6 mm diameter mounted on a side of the chamber and connected to a monochromator (TRIAX Jobin-Yvon 130) by a focalisation system. The monochromator is equipped with three diffraction gratings, one with 1200 lines/mm and the others with 300 lines/mm. This allows to cover a spectral range between 200 nm and 1000 nm.

The photon counting device is a Hamamatsu MCP-PMT R3809U-52 model. The DAQ system is shown in figure 7.3. The signal from the laser trigger is routed into a Ortec Pico Timing Discriminator (model 9307). A first output is directed to a Ortec Time to Analog Converter (model 9308). A second output is directed to a Lecroy Quad Coincidence Unit (model 622). The MCP-PMT signal is preamplified by a ORTEC 1-GHz preamplifier (model 9306) with a gain of 100 and then sent to a second Pico Timing Discriminator. One output is sent to the Lecroy Quad Coincidence Unit and a second one delayed by 60 ns and sent to the TAC. The last unit is required since the laser trigger has a fixed delay. A third output is sent to a SR400 Gated Photon Counter (Stanford Research System) along with the output of the Lecroy coincidence unit. The SR400 Gated Photon Counter allows to determine the rate of counts at the MCP detector, to keep under control the fraction of biased events. The TAC guarantees a 16-bit digital resolution in the range 0-325 s down to a binning of 1.22 ps and its signal is sent to a computer for the software system to finally determine the delay between the MCP and the laser trigger.

## 7.3 Preliminaries

Three parameters have to be kept under control during the irradiation, as they influence the sistematics of the system:

- energy of the excitation
- impulse response function of the system

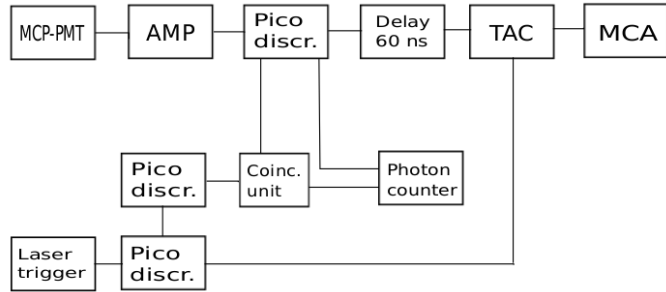


FIGURE 7.3: Schematics of DAQ system

- laser stability and photon counts

#### 7.3.1 VUV spectrum

The spectra of six harmonics in Argon (40 mbar) between 28 and 47 eV are shown in figure 7.4. The difference in the shape of the peak is given by the different intensities of the laser beam, fixed respectively, at 1, 2, and 4 mJ. As the intensity of the laser increases, the emission is characterized by broader peaks, and the presence of a large pedestal. Moreover relevant overlappings start to appear. This is due to the electron trajectories of each excited argon atom with different return time. It is possible to quantify this effect, as a narrow peak can be attributed to the emission of electrons with return time of less than half a laser period. On the other hand, the large pedestal can be related to the emission of electron with return time close to a full period of the laser field. Therefore the emission spectrum becomes a quasi-continuous one.

#### 7.3.2 IRF measurement

The Impulse Response Function (IRF) is the response of the DAQ system to a narrow excitation in time. This is usually measured at the beginning of the campaign and checked for stability at regular intervals. In this specific setup the width of the exctitaion pulse can be substantially neglected, being an order of magnitude below the typical scale of the physical processes involved. Thus the main sources of fluctuations in the timing response are the TTS of the photo detector and the electronics.

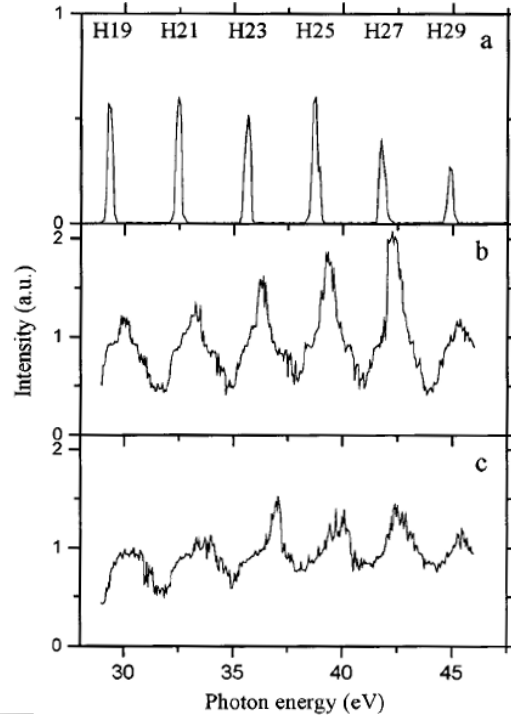


FIGURE 7.4: Schematics of the VUV line at CELIA Bordeaux Martin (2001)

In order to quantify the IRF, the standard procedure is to directly hit the photodetector with the laser light and measure the delay spectrum with respect to the trigger signal of the laser. If we consider the jitter on the trigger negligible, as it is in most cases, the only parameter to keep under control is the number of counts of the photo detector. In order to retain a low probability for pile up, the SR400 Gated Photon Counter was kept under control, well below 100 counts on a 1-second gated window. The IRF for the system is shown in figure 7.5. The IRF of the system, modeled with a multi Gaussian with tail towards high times due to ion feedback, gives  $\sigma_{IRF} = 30$  ps. In particular two parameters should be considered in terms of degradation of resolution: the width of the response under the first tailed Gaussian, and the ratio between the first peak and the ion feedback delayed one (in this case this delay amounts to  $\sim 350$  ps). In this case two order of magnitude separates the main and the secondary peaks. As shown in figure 7.5 the IRF shows a reflection, which is not eliminable because the setup could not be modified for logistics

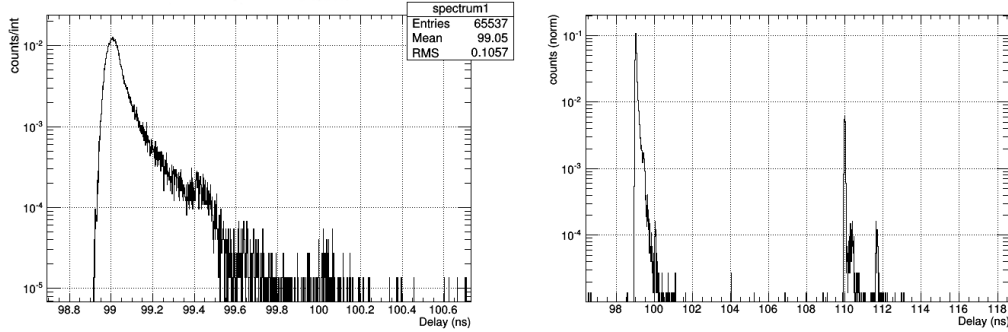


FIGURE 7.5: Impulse Response Function of the system excitation VUV - MCP-PMT.

reasons. This is never a nuisance for very fast kinetics, but it makes accurate decay time measurements for long decays not feasible. For rise time measurement this is not limiting, since the range can be safely tuned to extract the parameters, as will be shown below.

The measured IRF is deconvoluted from the measured signal via the method described in the previous chapter. This value accounts for three effects which can not be disentangled: the noise level of the instrumentation with respect to the height of the signal, the TTS of the detector and the time walk of the detector itself. As will be shown in the next chapter Hamamatsu MCPs present a large amount of time walk jitter, which can not be corrected in this setup. Considering a signal that ranges from 5 mV to 50 mV for single photons, and the amplification gain of the Ortec pre amplifier ( $\sim 100$ ), the signal from the Ortec pico timing discriminator suffers from a  $\geq \pm 20$  ps shift in the timing output for the range considered. This is in agreement with the data from the producers, since the time walk corrected MCP nominal  $\sigma_{SPTR}$  is  $\sim 20$  ps and the laser contribution (2-3 ps FWHM) can be neglected.

### 7.3.3 Control of the bias fraction

As discussed in the previous chapter, the count rate at the stop detector bias the measurement at high pile up probability. In the case of a MCP-PMT the probability of pile up is still very low at the typical time constants of the samples measured, since the dead time of the detector is less than 1 ns.

There is no direct way to store the actual pulse that is fed to the electronics in this setup, so it is necessary to completely rely on the values given by the SR400 Gated Photon Counter. This device allows to control dynamically the number of pulses fed to the electronics on a given time window, which is usually set to 1 s. Knowing the typical time constants of the sample in exam, or checking it with a quick preliminary measurement, allows to choose an appropriate number of counts per second, which is for all the samples measured between 100 and 200 Hz. In the case of rise time, as shown in the previous chapter the effect of high count rates is less pervasive on the parameter extracted, and at the rates considered in this VUV setup does not affect the values obtained significatively.

#### 7.4 Data analysis

The samples measured present different size and surface condition in terms of polishing and depolishing. These aspects can be neglected, given the excitation energy and the geometry of the setup. Indeed photons in the VUV range, as already discussed, can travel for very short distances in a heavy scintillator, in the range of 100 nm. This means that the excitation takes place on the surface of the crystal. If, on the contrary, the radiation came on the opposite side of the detection system, one could not neglect transit time effect of photon extraction. The geometry of the system is shown in figure 7.6: an optical fiber is able to collect photons coming directly from the excitation point on the surface, that is photon extracted at higher angle and thus rebounced at the lateral faces will be highly suppressed at the detector. The samples measured were:

FIGURE 7.6:

- LSO:Ce,Ca (2x2x3 mm<sup>3</sup>)
- LSO:Ce (CTI, 2x2x3 mm<sup>3</sup>)
- LYSO:Ce (Proteus, 2x2x3 mm<sup>3</sup>)

- LYSO:Ce (Sipat, 2x2x3 mm<sup>3</sup>)
- LGSO:Ce (2x2x3 mm<sup>3</sup>)
- CeF<sub>3</sub> (2x2x3 mm<sup>3</sup>)
- LuAG:Ce (0.13%, 2x2x3 mm<sup>3</sup>)
- LuAG:Ce (0.08%, 2x2x3 mm<sup>3</sup>)
- LuAG:Ce (0.5%, 2x2x3 mm<sup>3</sup>)
- LuAG:Ce (0.44%, 2x2x3 mm<sup>3</sup>)
- LuAG:Pr (1.5x1.5x3 mm<sup>3</sup>)
- BGO (3x3x5 mm<sup>3</sup>)

Due to time constraints, measurements were performed at a 1 ps TDC binning for crystals with high light yield. For crystals with low light yield (almost all the Garnets), the binning was increased to 10 ps, at the expenses of limited accuracy.

## 7.5 Fit procedure

The fit procedure has been presented in the last chapter and it consists in the minimization of the function  $-\log L$ , where the likelihood function  $L$  has been defined in the previous chapter and is given by the convolution of the model and the IRF. The function used for the fit is a simple multi-exponential model for n decay component as

$$p(t) = \sum_{i=1}^n \frac{P_i}{\tau_{d,i} - \tau_{r,i}} \left( e^{-\frac{t-t_{shift}}{\tau_d}} - e^{-\frac{t-t_{shift}}{\tau_r}} \right) + C_{bg} \quad (7.2)$$

where  $\tau_{shift}$  is the turn-on of the scintillation pulse and  $C_{bg}$  is the background level. The software used for minimization is Matlab.

In order to determine the confidence interval on the parameters it is necessary to consider the influence of three parameters on the fit results, that is the rise time, the decay

time and the range of the fit. The number of counts collected for the spectrum is about 1.6 millions, which is the case for most of the samples measured. We consider here only the case for one single component, in the case of rise time is usually enough to consider the first component, especially if it is significantly longer than the rise time constant. This is the case for most of the samples measured: as an example the LSO Cerium doped compounds present a rise time of the order of  $\sim 50$  ps and a decay time of the order of  $\sim 40$  ns. In order to quantify the effect of mutual variation of fit parameters, a simple toy model was used with the shape described above. The analysis was then performed over the samples measured for parameters estimation.

The range of the fit systematically influences the time constants extracted. As the range considered is enlarged, the decay part of the spectrum becomes more relevant, and the artefacts in the IRF influence the parameters extracted. It is then necessary to restrain the range of the fit, since the IRF measured for the setup presents reflections at longer times. On the other hand restricting the range entails a loss of information for what concerns the decay part of the curve. In a first time we are not interested in defining the decay time with the best possible accuracy, so we chose a range that optimizes the rise time determination.

The toy model used presents in this case a rise time of 36 ps and a decay time of 33 ns. In order to quantify the effect of range variations on the fit, we let the range itself free over significative bins, that is starting from the rise of the scintillation pulse. In figure 7.7 is shown the influence of range variation on the extracted parameters from the fit routine. For what concerns the decay time, as soon as the range starts to comprehend a larger fraction of the decay of the pulse, the value stabilizes and the change is contained in less than 5 ns variation which is optimal considering the likelihood confidence level. There is a systematic under estimation of the value, though, since the loss of information on the last part of the pulse biases the dataset, as shown in previous chapter. The same goes for the rise time in terms of comparison with the likelihood confidence level, therefore the optimal range was chosen to be over bin 15000. In this configuration the influence of the range is

limited to a few ps.

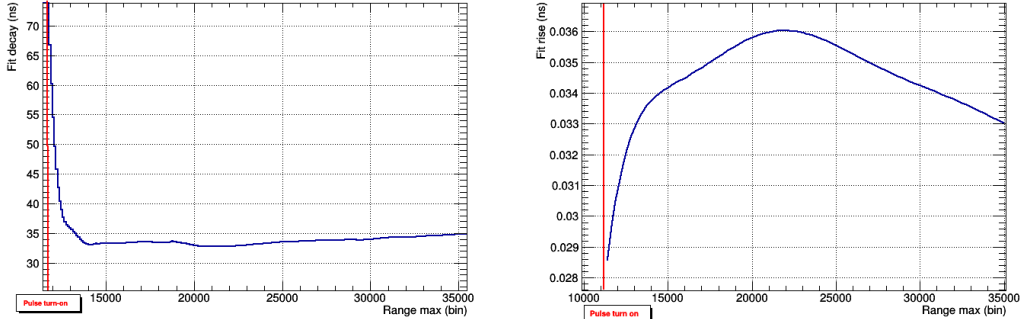


FIGURE 7.7: Range influence on the parameters extracted for decay time (left) and rise time (right) for a toy model ( $\tau_r = 36$  ps,  $\tau_d = 33$  ns)

For what concerns the confidence level on the parameters extracted from the fit, we profiled the two dimensional likelihood over the parameters optimized, that is rise time and decay time, as shown in figure 7.8 for different number of counts collected for the rise time. In this case a binned likelihood approach requires a determination of a confidence interval based on a asymmetric likelihood. At the best fit point the function to minimize  $-2 \ln L$ , tends to a chi-squared distribution for (n-2) degrees of freedom. In this case it is customary to define a confidence level the interval  $(min_L, min_L + \frac{1}{2})$  since in the limit of normally distributed data for large counts it translates to a 95% confidence level. In this case the likelihood is close to this approximation, therefore this convention will be used for confidence intervals.

As an example in figure 7.9 the case for a LSO Sipat crystal is shown. In this case, for a bi exponential fit with one component decay, we will quote the values, with relative asymmetric confidence level  $\tau_r = 36_{-30}^{+27}$  ps and  $\tau_d 40.5_{-0.9}^{+0.7}$ .

## 7.6 Results

### 7.6.1 Data

The results obtained for the sample measured can be broadly divided in two groups: a first group contains the LSO type crystal, the CeF<sub>3</sub> and the BGO and they present very

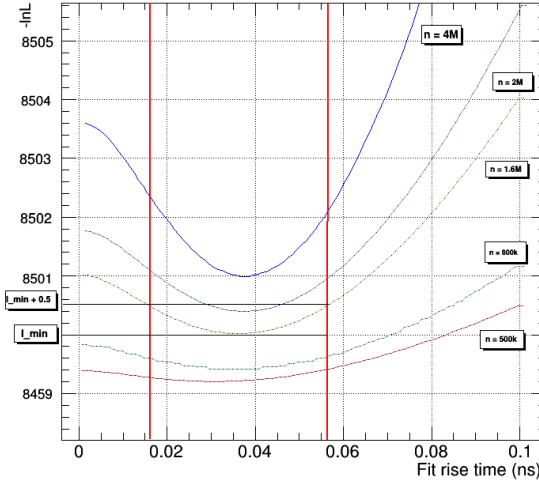


FIGURE 7.8: The statistics collected is varied from 100000 to 4000000 and the influence on the likelihood for extracted rise time is shown/

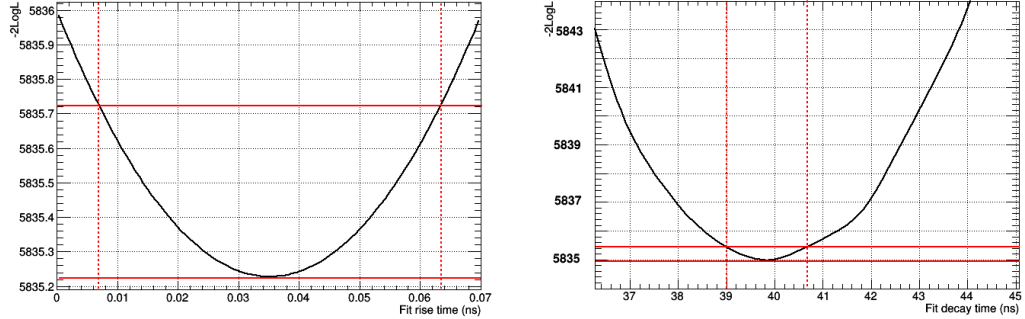


FIGURE 7.9: The likelihood for rise time (left) and decay time (right) is shown for LYSO Sipat dataset, with relative confidence level.

fast rise times ( $< 40$  ps). The group of the Garnets, on the other hand, with different dopings (Ce and Pr), presented slower rise times ( $>150$  ps). Plots for the different samples measured are shown in the figures of this section. On the top of each figure, the deviance residuals obtained for likelihood estimation are reported, to graphically show large bias in the fit data if present. This residuals are defined as

$$R_i = \sqrt{2 \left[ c_i \log \frac{c_i}{g_i} - c_i + g_i \right] \text{sign}[c_i - g_i]} \quad (7.3)$$

and  $c_i$  and  $g_i$  are respectively the counts and the model expectations in channel i. The values obtained for the decay time, as discussed in the previous section, should be considered carefully. Since our main interest does not lie in the decay time and given the problems related to the IRF, the range of the fit was restricted. This leads to a systematic under estimation of the decay time. For the case of Sipat LYSO, Proteus LYSO, CTI LSO and LGSO, the parameters were extracted considering a one component decay. For what concerns CeF<sub>3</sub> and LSO:Ce,Ca the fit was performed for a two decay component curve. This is in agreement with measurement performed in this study (see next chapter), in Gundacker (2014), and in ?. It is worth to underline that in this case, as the first fit component is quite fast (<10 ns) the value is more accurate, since accuracy benefits from a larger time window. Results are shown in table 7.6.1.

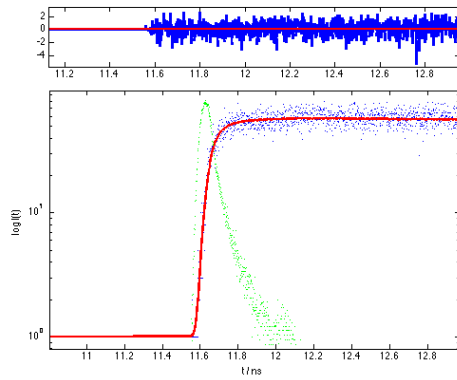


FIGURE 7.10: Fit data and likelihood residuals for LYSO Sipat and LYSO Proteus.

Crystal	$\tau_r$	$\tau_{d,1}$	$\tau_{d,1}$
LYSO Sipat	$36^{+30}_{-27} ps$	$40.5^{+0.9}_{-0.7} ns$	
LYSO Proteus	$26^{+30}_{-26} ps$	$39^{+0.9}_{-0.7} ns$	
LSO CTI	$23^{+20}_{-18} ps$	$37^{+0.8}_{-0.8} ns$	
LSO:Ca	$23^{+22}_{-19} ps$	$10^{+0.4}_{-0.3} ns$	$30^{1.0}_{-0.8} ns$
LGSO	$27^{27}_{-15} ps$	$38^{+0.8}_{-0.8} ns$	
CeF <sub>3</sub>	$22^{30}_{-15} ps$	$5^{+0.4}_{-0.2} ns$	$18^{+0.8}_{-0.5} ns$
BGO	$30^{35}_{-25} ps$	$10^{+0.4}_{-0.2} ns$	long

As briefly explained before, the measurements for some LuAG samples were performed

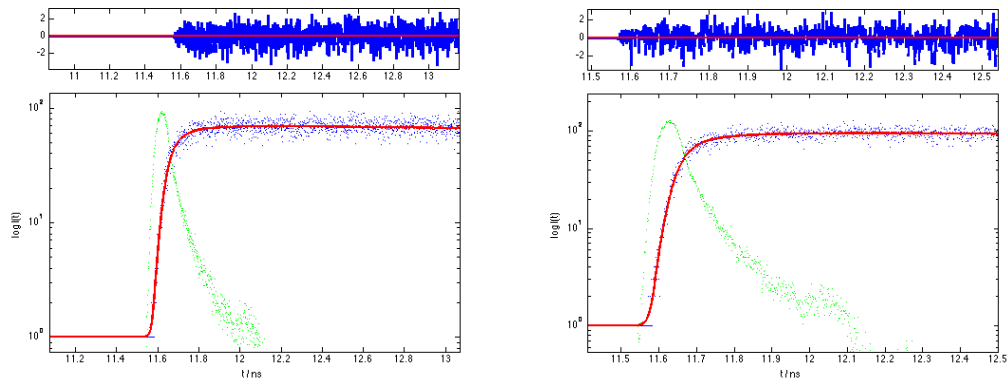


FIGURE 7.11: Fit data and likelihood residuals for LSO CTI and LSO:Ce,Ca.

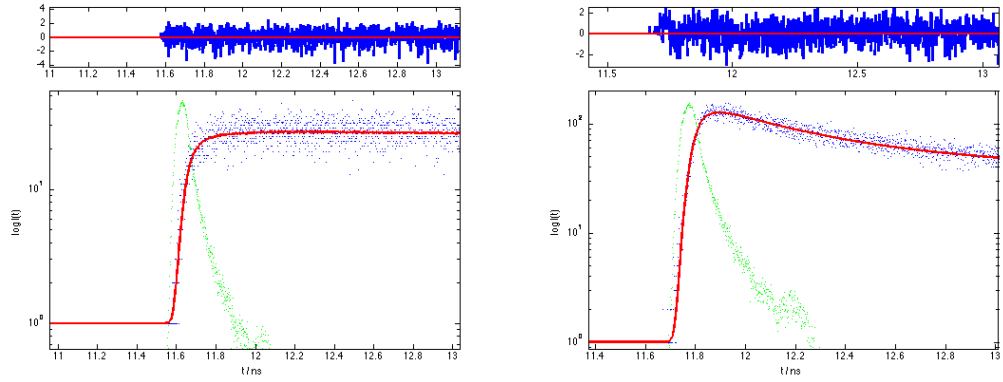


FIGURE 7.12: Fit data and likelihood residuals for LGSO and CeF<sub>3</sub>.

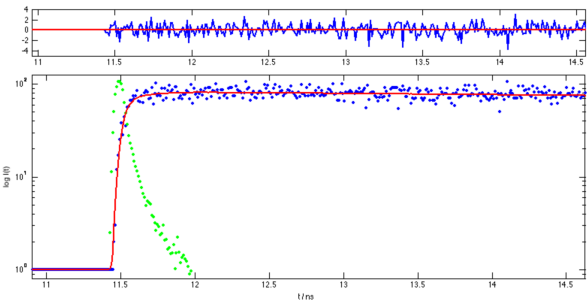


FIGURE 7.13: Fit data and likelihood residuals for BGO.

with a different TDC binning, due to the scarce light yield that implied very long accumulation times. In these cases the TDC binning is 10 ps. As shown previously this influences the error on the rise time, which for these samples is more pronounced. The Garnets show different time constants, and can vary very much based on the doping concentration, the purity of the sample, the energy of the excitation. Since the measurements are performed on a limited time window, the decay time can be quite biased towards fast constants, and very low decay times can be indistinguishable from background. This is also the reason for a large uncertainty on the fit decay time. Results are shown in table 7.6.1.

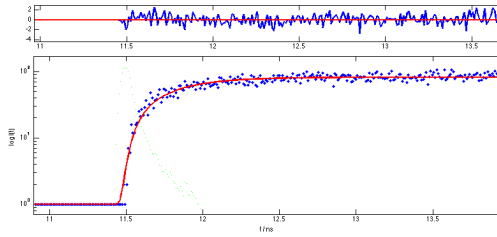


FIGURE 7.14: Fit data and likelihood residuals for LuAG:Ce (0.08%).

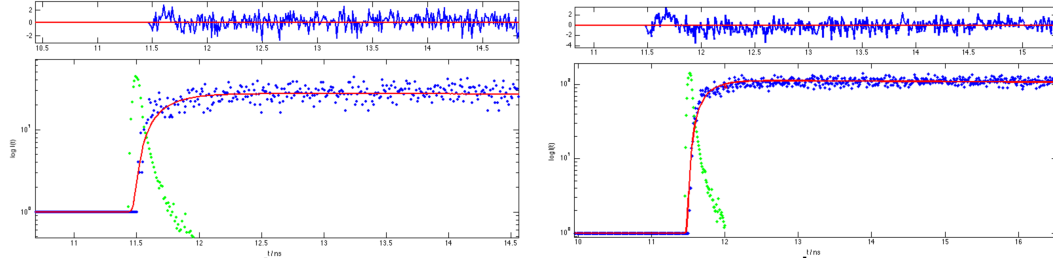


FIGURE 7.15: Fit data and likelihood residuals for LuAG:Ce (0.5%) (left) and LuAG:Ce (0.44%) (right).

Crystal	$\tau_r$	$\tau_{d,1}$	$\tau_{d,2}$
LuAG:Ce (0.08%)	$280^{+52}_{-51}\text{ps}$	$65^{+2.6}_{-2.1}\text{ns}$	longer
LuAG:Ce (0.13%)	$270^{+54}_{-54}\text{ps}$	$60^{+2.5}_{-2}\text{ns}$	longer
LuAG:Ce (0.44%)	$190^{+45}_{-40}\text{ps}$	$58^{+2.3}_{-2}\text{ns}$	longer
LuAG:Ce (0.5%)	$212^{+45}_{-45}\text{ps}$	$56^{+2.4}_{-1.8}\text{ns}$	longer
LuAG:Pr	$190^{+50}_{-50}\text{ps}$	$28^{+2.3}_{-2.1}\text{ns}$	

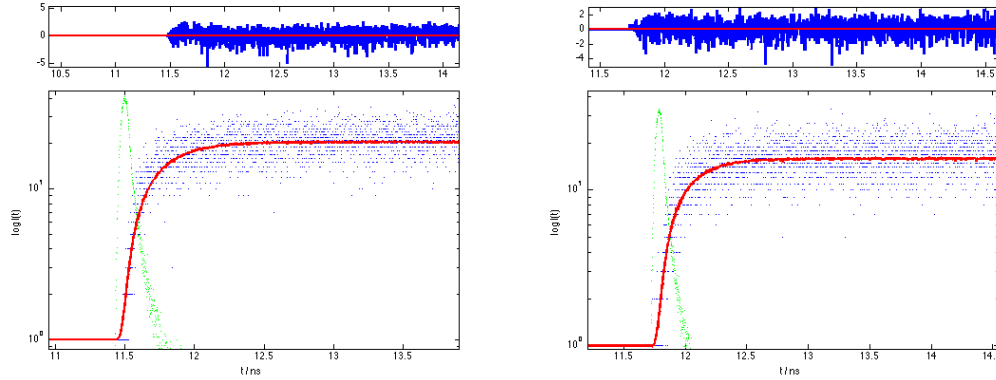


FIGURE 7.16: Fit data and likelihood residuals for LuAG:Ce (0.13%) (left) and LuAG:Pr (right).

### 7.6.2 Limitations

The setup is limited due to the following constraints: the time resolution of the detection system and accumulation times. These two problems are intimately related on one side, since given a certain time resolution, it is necessary to accumulate for longer times to reduce the incertitude on the extracted parameter. This is not always possible for crystals used in high energy and medical physics, because the long values of time constants requires longer time windows and bigger binnings. Moreover attention should be paid in the case of very fast rise times, if the constant extracted is close to the measured response, as it is the case for many samples object of this study. In this case deconvolution is less reliable.

This goes for the statistical error, but the limited resolution of the detection system influences the way the time profiles can be extracted. Indeed, as briefly explained in the previous chapter, the way parameters are extracted in canonical fluorescence analysis are strictly model dependent. That is, accurate distinction between one or multi component exponential can be hard. This means that only qualitative analysis can be done, comparing rise times of different samples in different condition, obtaining effective parameters usually sufficient for any practical application. More difficult is define quantities related to specific processes in the lattice, unless a thorough wavelength analysis is performed, see for example et al. (2013).

A third limitation is the excitation energy. As explained in the previous chapter there is a non negligible contribution coming from high energy excitation, especially form Cerenkov photons collected. With VUV excitation this information is not accessible. On the other hand in this geometry it is possible to neglect the spread given by photon extraction, and compare this with respect to higher energy excitation.

### 7.6.3 Discussion

As already stated, the crystal measured can be grossly divided in two groups. The first contains BGO and  $\text{CeF}_3$ , that is two intrinsic and self activated scintillators and lutetium ortho silicate with Cerium doping. They have fast ( $<40$  ps) rise times, indicating that the excited states are rapidly created after an ionization event. A second group contains the doped Garnets, LuAG:Ce and LuAG:Pr. They have slower rise times due to processes that delay the transport of charge carriers to the activator atom.

Considering the limits of the setup presented before, these results are not trivial to interpret. It is possible to consider two lines of analysis to explain the results

- dopant concentration
- competitive processes due to lattice characteristics

A first look at the result may suggest a correlation between dopant concentration and rise time. In particular more available cerium sites for scintillation entail faster transfer to excited states and thus faster rise times, save quenching effects.

No information about Cerium concentration in the LSO samples measured was available. Nevertheless considering the standard dopant concentration for industrial crystal from manufacturers, the concentration is likely to be around 1%. Intrinsic scintillators seem to show a faster rise times, indicating that the transfer efficiency at the level of rise time to the luminescence centers is fast. For example in the case of  $\text{CeF}_3$  the molar concentration of Cerium centers is 1. Based on the data obtained, though, there is no evidence that intrinsic scintillator are faster than extrinsic in the LSO group, which could be ex-

pected based on a dopant concentration dependance. It should be noted that this values are at the very limit of the detection system, so statistically less accurate.

On the other hand perfectly known is the Cerium concentration for the Garnet samples. The Garnet samples belong to different batches, so caution should be considered when a comparative analysis is performed, since growth parameters can differ significantly. Based on the error of the measurement though it is not possible to conclude that crystals with low percentage of doping show slower rise times, even if the trend deserves a better understanding. Indeed the 0.08% and the 0.13 % Cerium doped samples present the slower rise times for the Garnet group, and a measurement campaing changing the dopant concentration over a wide range of dopings could be resolute, see also the non conclusive study made on  $\text{LaBr}_3$  in et al. (2004b).

It is necessary to consider also a "horizontal" analysis based on the very different lattices, dopants and scintillation mechanism of the samples measured. In LuAG crystals, for example, an important role is played by excitonic transition and only a wavelength based analysis can reveal possible differences, see for example et al. (2013). It is clear that differences between Cerium doped LSO and LuAG samples can not be explained solely based on dopant concentration difference.

#### 7.6.4 Perspectives

Intrinsic limitations of the setup do not allow for a definitive assessment of rise time properties. Given the high error associated with measurement, the biggest effort should be reserved to the improvement of the accuracy.

In order to achieve that, a first idea is to tackle the statistical limitations due to the number of samples analyzed. An extensive campaign should be performed with different crystal species, alternating combinations of lattice, dopants and concentration. This would be very time-demanding.

Time constraints are the main limitations for a complete wavelength analysis, especially in the case of crystals with different scintillating components. This is interesting for

Garnets, for example, LaBr<sub>3</sub> or more complex insulators like LiYF<sub>4</sub>.

The most important improvement could come from the detection method. There are two ways of achieving this: improving the IRF of the detection system or exploit a classical approach of fluorescence analysis, frequency mixing. The IRF of the detection system depends mainly on the stop detector and it has some lower limit at a few tens of ps. This makes the analysis of processes at the pico second scale not possible. Frequency mixing approach on the other hand relies on second order processes in non linear crystals, so to rely less on read out electronics. The problems concerns mainly feasibility for slow crystals, since these techniques require fast and bright emissions.

In order to cope with all the issues presented the method would benefit from the use of a streak camera ?, which would allow for shorter accumulation times, wavelegnth based analysis and high resolution ( $\sim 20$  ps FWHM).

# 8

## Na-22 measurement

In a PET system the excitation energy of the incident  $\gamma$  is 511 KeV. As stated previously, at this energy a series of different processes intervene and contribute to the time resolution measured. Three elements should be considered, when comparing time profiles to the one measured with VUV radiation:

- production of Cerenkov photons
- volume excitation (and so transit time spread in the bulk)
- de excitation down to the thermalization region

The relative strengths of these phenomena have already been compared in chapter 6, and the possibility of measuring at high energy allows to physically quantify these effects. In particular a TCSPC system based on a  $^{22}\text{Na}$  source has been implemented, using a tagging crystal and a SiPM as a start signal and a MCP-PMT as a stop signal.

### 8.1 Phenomenology

The physics of  $\gamma$  photon interaction have been already introduced in chapter 2. In order to build a time correlated single photon counting experiment two time signals are necessary,

a start signal and a stop signal. A simple way to obtain this is to use a  $\beta^+$  active isotope, such as  $^{22}\text{Na}$ . This isotope emits a positron according to the decay reaction  $^{22}\text{Na} \rightarrow ^{22}\text{Ne} + \beta^+ + \nu_e + \gamma$ . The positron yield is relatively high, 90.4%, and competitive processes are electron capture (EC) and direct transition to the Ne ground state. In the positron emission case the Ne ground state is reached after 3.7 ps by emission of a  $\gamma$  quantum of 1.274 MeV. The half life of the isotope is 2.6 years. It is worth to note that, as outlined

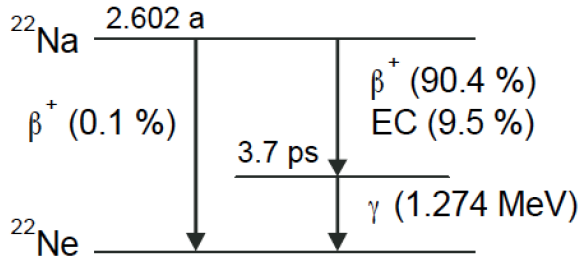


FIGURE 8.1: Decay scheme of  $\text{Na}^{22}$

in chapter 2 the Cerenkov threshold for heavy scintillators is below the energy of the annihilation  $\gamma$  produced by the isotope.

## 8.2 Experimental setup

The scheme of the setup is shown in figure 8.2. The tagging crystal used in this configuration is a  $2 \times 2 \times 5 \text{ mm}^3$  LSO:Ce,Ca pixel, readout by a SiPM board amplified by a NINO chip. The SiPM mounted on the board is a  $3 \times 3 \text{ mm}^2$  Hamamatsu MPPC S10931-050P with  $50 \mu\text{m}$  cell size. Its signal is then fed in to the NINO chip described in chapter 3. The NINO technology, thanks to the time-over-threshold technique, collects time and energy information at the same time, thus allowing for a complete cut analysis. The SiPM was biased through the board at 72.5 V, and the NINO at the nominal working voltage of 2.5 V. Moreover a potentiometer installed in the board allows to set up the lower and higher threshold for the NINO chip, as will be discussed in the following paragraph. The signal is directly coupled to a high-bandwidth oscilloscope, able to digitize the pulses, a LeCroy

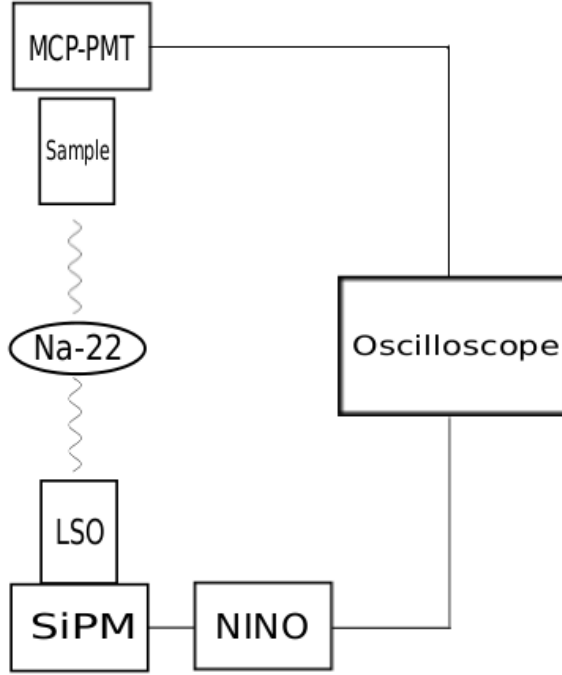


FIGURE 8.2: The setup and DAQ for the  $\gamma$  measurement is shown.

DDA 735Zi (10 GS/s). A sample of the NINO signal is shown in figure 8.3. The stop

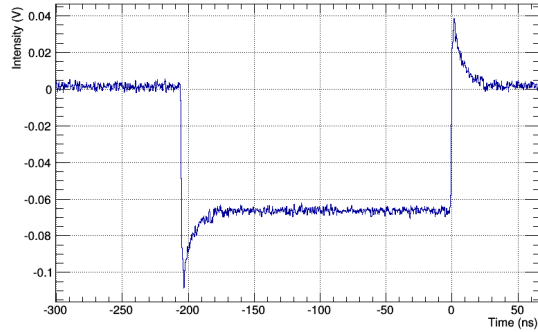


FIGURE 8.3: Example of NINO output from SiPM signal.

signal is directly routed in to the oscilloscope without amplification. The stop detector is a Hamamatsu R3809U-50 MCP-PMT. The signal of the MCP is very fast, as can be seen in figure 8.4, since it is almost completely contained in 1 ns. This allows for a multi photon detection setup. Indeed the two signal lines from the oscilloscope were saved for

offline analysis, acting as a completely digitalization of the signal. The components of

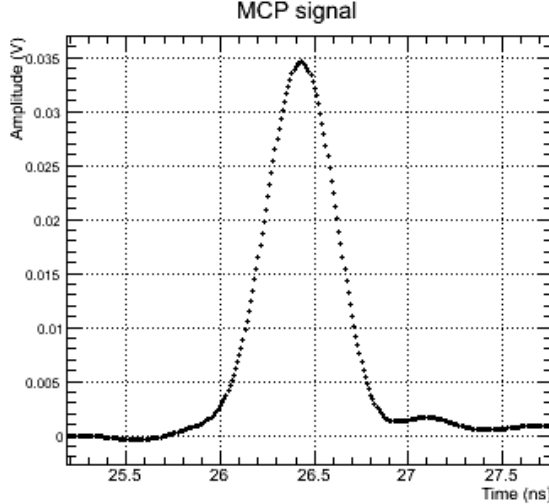


FIGURE 8.4: Example of Hamamatsu MCP-PMT output.

the apparatus were placed in a cooled light-tight box, and the temperature held at 20 °C with a degree tolerance. Cooling is necessary to maintain the performance of SiPM. Indeed the number of thermal electrons that give rise to dark counts in the detector is strongly dependant on the temperature. In the setup presented, as already pointed out, the accumulation times can be quite slow. It is necessary to keep the number of detected photon low, so that no significant bias is introduced in the measurement. The number of starts is thus much bigger than the number of stop at the acquisition. In order to gather data for a reasonable accumulation time, it is essential to reduce to the minimum the time the acquisition system (i.e. the oscilloscope) is busy. The MCP benefits from temperature stability as well, and for the same reasons, but the noise level is negligible if compared to the SiPM. Moreover the threshold set for the SiPM plays an important role on the DCR level of the device: in this case the DCR at 200 mV threshold is 0.88 Mcps (for complete discussion see Gundacker (2014)).

## 8.3 Preliminaries

In order to extract the parameters leading to the determination of rise time values and to critically analyze the impulse response function measured, the properties of the start and stop detectors were separately measured. In a second phase, the impulse response function was measured, without the sample, as it is a crucial part for the iterative deconvolution routine. Finally the bias fraction for an optimal count rate for the sample measured was assessed.

### 8.3.1 Characteristics of the start signal

As already outlined, the start signal originates in a tagging crystal. The crystal is a 2x2x5 mm<sup>3</sup> LSO:Ce, Ca pixel, glued to the SiPM. Between 4500 and 5000 photons are collected at the photodetector, already corrected for the quantum efficiency. The working point for the NINO chip, biased at 2.5 Volts, was set via a potentiometer on the board, at 200 mV. In order to estimate the contribution of the start signal to the total IRF the board was measured in CTR along with a reference board. The setup for CTR measurement is a simple start-stop configuration with two similar boards and a <sup>22</sup>Na source. The reference board was measured separately and details will not be given here, for a complete discussion see Gundacker (2014). The CTR on the reference arm is  $\sim 105$  ps FWHM, measured after selection at the photopeak on both arms, as shown in figure 8.5. In the same figure the <sup>22</sup>Na spectrum in LSO is shown, with the single photon signal at the beginning of the range. Non linearity due to the time over threshold technique are present, although not taken into account separately. Since the best time resolution is delivered in the photopeak region, the influence of non linearity in the energy spectrum is negligible.

The electronics contribution depends on the data acquisition electronics and its noise level. This contribution can be estimated as

$$\sigma_{noise} = \frac{RMS_{noise}}{dV/dt} \quad (8.1)$$

where the RMS of the noise is determined from the pedestal of the signal and  $dV/dt$  is the

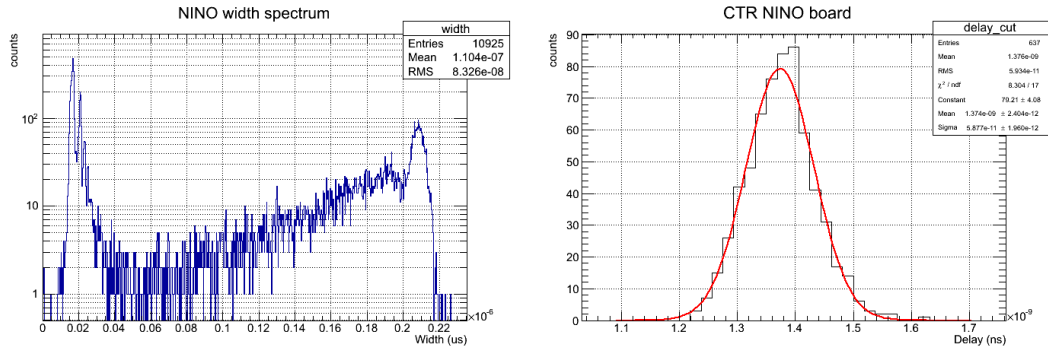


FIGURE 8.5: Example of start spectrum (left) and measured CTR at the photopeak (right).

slew rate. In this case it can be estimated at 37 ps (for a complete discussion see Gundacker (2014)).

### 8.3.2 Characteristics of the stop signal

The stop signal is a Hamamatsu R3809U-50 MCP-PMT. In order to estimate the contribution of the stop signal to the total IRF the MCP time response was measured with the aid of a high resolution laser. The setup is composed by a Picosecond Diode Laser-Pilas head and a series of optical filters to reduce the light intensity hitting the photodetector down to less than one photon per excitation. The two signal are then routed to a LeCroy Oscilloscope LeCroy DDA 735Zi (10 GS/s) and data analysis is performed offline. In order to measure the MCP S PTR a high resolution laser is needed, matching the wavelength of emission of the scintillator measured in TCSPC, if possible. The Pilas laser delivers a 28.9 ps pulse (FWHM) at a frequency of 100 kHz and a wavelength of 419 nm. The rising edge of the laser trigger is shown in figure 8.6. To extract the time difference between the laser trigger and the MCP signal, an offline analysis was performed. The digitized pulses were saved and analyzed with the software package ROOT. A threshold for trigger was set at 5 mV on the MCP and the time difference was calculated in the interpolated signal. Therefore the sampling of the signal goes from 10 GS/s to 100 GS/s. As shown in figure 8.7, the amplitude of the MCP varies considerably on the range considered, that is between 5 mV and 50 mV, where most of the signals lie. A saturation effect due to

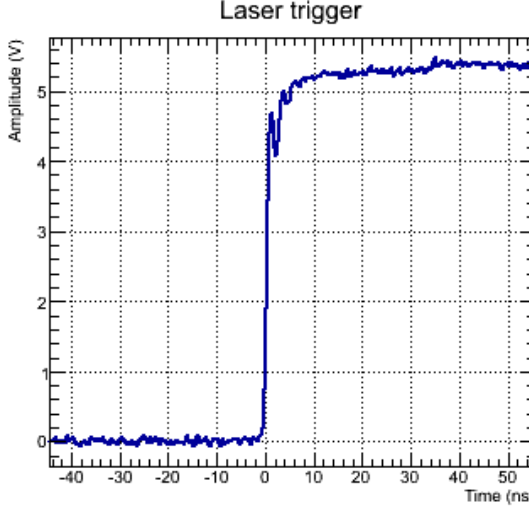


FIGURE 8.6: Rising edge of the laser trigger.

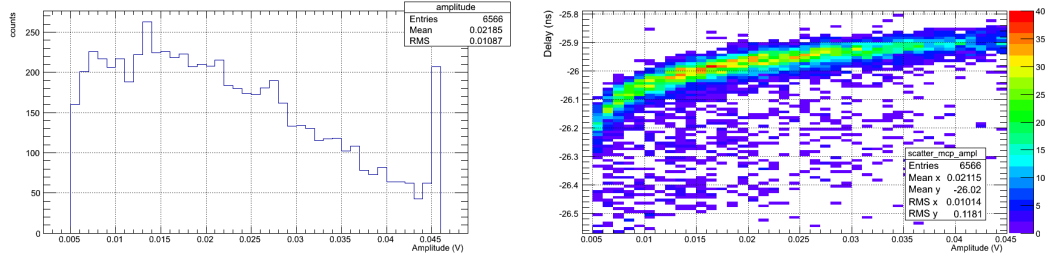


FIGURE 8.7: Amplitude spectrum for the MCP-PMT (left) and scatter plot amplitude - delay (right).

the limited amplitude window of the oscilloscope is also present, but cut in data analysis. This variation makes the stop detector prone to important time walk. The possibility of storing separately the digitized pulses allow for a complete selection and correction of these events. The scatter plot in figure 8.8 is corrected through a simple time walk correction. If we define the real time stamp brought by the signal as  $t_{real}$ , the threshold crossing time  $t_{measured}$  and the jitter given by the time walk we can write

$$t_{ideal} = t_{measured} - t_{walk} \quad (8.2)$$

and we can extract the walk correction as

$$t_{walk} = A + B \cdot E^C \quad (8.3)$$

where  $E$  is a measure of the charge collected. In this case it will be the amplitude of the MCP-PMT signal. At this point the spread on the time difference spectrum shown in

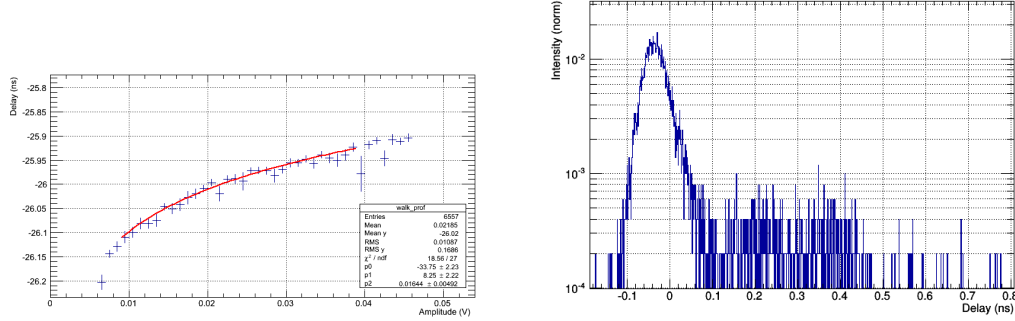


FIGURE 8.8: Time walk correction on the spectrum profile, MCP-PMT against laser trigger (right) and resulting corrected response (right).

figure 8.8 is given by four phenomena:

- width of the laser signal
- jitter on the laser trigger
- S PTR of the detector
- electronics noise

It is natural to consider this processes uncorrelated so to concur to the smearing of the time distribution as

$$\sigma_{TOT}^2 = \sigma_{S PTR}^2 + \sigma_{laser}^2 + \sigma_{trigger}^2 + \sigma_{noise}^2 \quad (8.4)$$

The laser width was taken from the datasheet, and amounts to 30 ps FWHM. The laser trigger can be substantially neglected as it amounts for  $\sim 4$  ps FWHM. Given the slew rate of the signal the  $\sigma_{noise}$  amounts to  $\sim 10$  ps.

The spectrum measured can be grossly modeled as a Gaussian with a tail towards high delays. We notice from figure 8.7 that ion feedback modifies the signal at higher times but it is almost two order of magnitude lower than the peak, as it is expected from a Chevron configuration. Considering the Gaussian peak we find  $\sigma_{TOT} = 25$  ps, so that we can infer  $\sigma_{S PTR} = 18$  ps, given that  $\sigma_{noise}^2$  amounts to 10 ps and  $\sigma_{laser}^2$  to 13 ps.

### 8.3.3 IRF measurements

The last step is the measurement of the impulse response function (IRF), that is global variance on the estimate of the time stamps given by the combined effect of the start and stop uncertainties. This time spectrum needs to be deconvolved from the time spectrum of the sample measured in order to extract the parameters of the fluorescence. In order to estimate the impulse response function, the set up presented in the previous section was used without the scintillation sample. The start signal retains the same characteristics, but the stop signal is given by a direct interaction in the MCP-PMT. This allows to disentangle the measured curve from the effect of the crystal, time constants and travel spread of the photons.

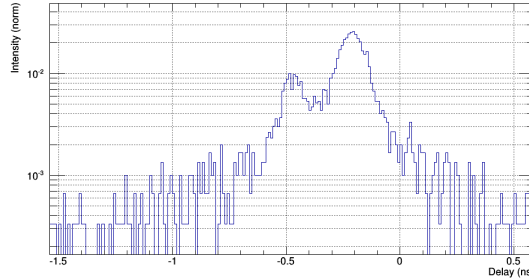


FIGURE 8.9: Measured response of the stop signal (MCP) against start signal (SiPM).

The time walk corrected time spectrum is shown in figure 8.9. Two separable components are present, separated by  $\sim 300$  ps. In this configuration, The processes that concur to the time spectrum are:

- Cerenkov photons produced by  $\gamma$  photons impinging in the entry window of the

## MCP-PMT

- direct interaction of the  $\gamma$  photons in the MCP stack

The delay of the two processes is contained in a time window of  $\sim 300$  ps. Given the large variation in the output signal of the MCP it is not possible to select event by event with a pulse shape rejection method. Using a simple Geant4 simulation it is possible to show that Cerenkov photons produced in the window need to interact in the photocathode and then allow time for the produced photo electron to travel in the electric field to the MCP stack. On the left side of figure 8.10 the times of Cerenkov production in the entry window and the time of a  $\gamma$  photon interaction in a MCP stack is shown. It is then necessary to add the

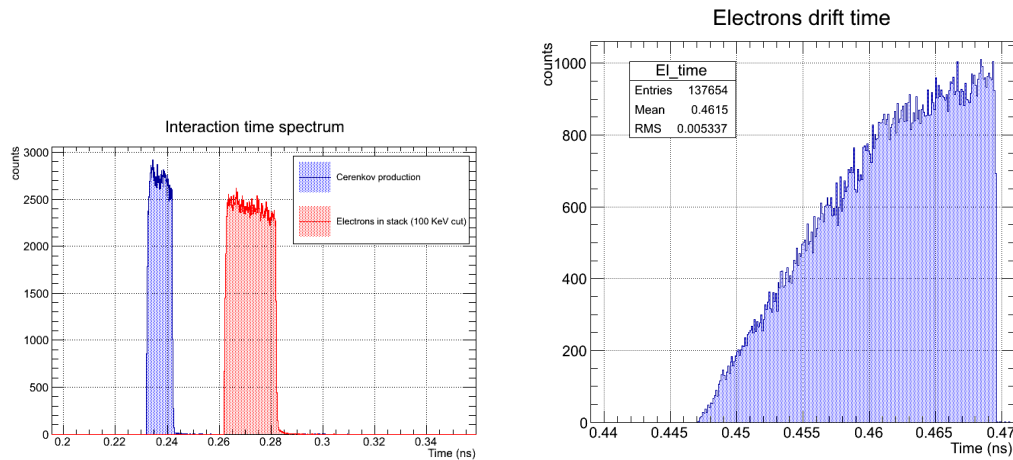


FIGURE 8.10: Time of interaction simulate for MCP stack and entry window Cerenkov photons (left) and drift time of electrons after the photocathode (right).

drifting time of the electrons between the photocathode and the first MCP stack, based on the geometry of the detector. The drifting electric field by design is given by the voltage divider of the detector, and amounts to 310 kV/m. As shown on the right side of figure 8.10 the drifting time of the electrons matches the time difference in the two components present in the measured IRF, and small deviations can be ascribed to partial knowledge of the detector materials and geometry of the electric field in the drifting region.

This phenomenon can be experimentally shown by selectively suppress one of the two processes. The setup was then slightly changed by tilting the MCP-PMT with respect to the start-source system. Then a lead screen was placed in between and two set of

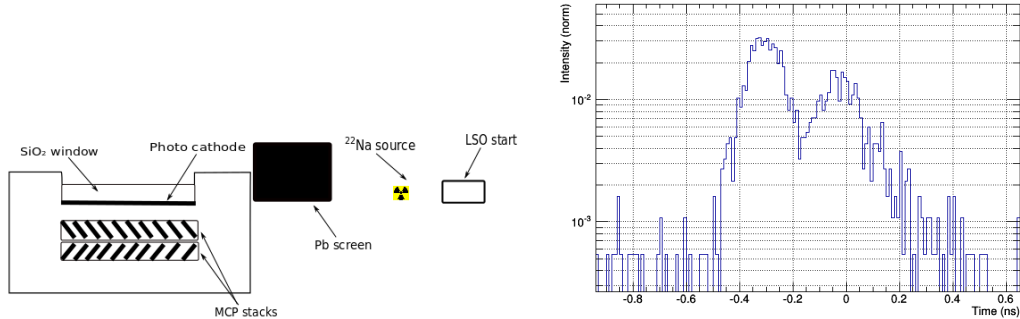


FIGURE 8.11: Setup for  $\gamma$  interaction in stack (left) and spectrum recorded (right)

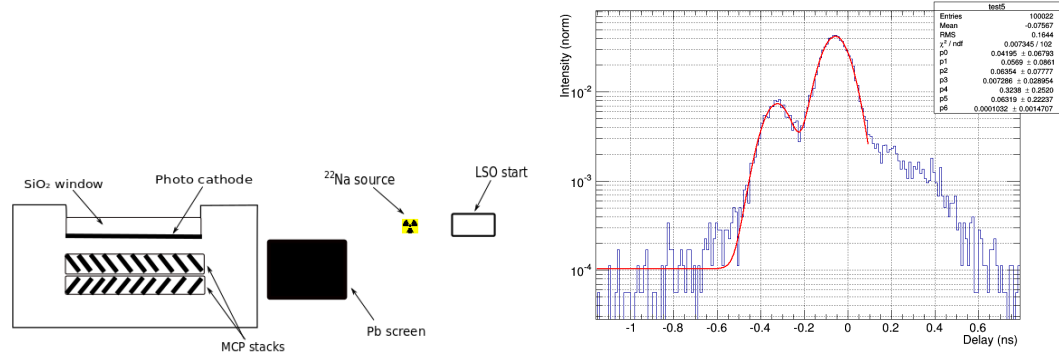


FIGURE 8.12: Setup for Cerenkov production in window (left) and spectrum recorded (right)

measurements was performed, as shown in figure 8.12:

- a first one with the screen covering the direct line of interaction between the source and the position of the MCP stack deduced from the design of the detector
- a second one with the screen covering the section of the entry window

It was then possible to suppress, respectively, the direct  $\gamma$  interaction in the stack and the Cerenkov production in the window. The relative intensity of the two peaks is reversed, as

shown in figure 8.11. The final time resolution can be inferred from the last figure, since the IRF to be deconvolved is composed only by the part of the spectrum related to photo electrons. As will be explained below, the direct interaction of  $\gamma$  photons in the stack brings additional spurious background to the spectrum, but it is not related to the scintillation pulse. Nevertheless the two peaks show similar width, and this is due to the fact that the resolution is dominated by the start signal, which is far worse and the slight difference given by the electron drift is negligible. As a consequence, we cut on the Cerenkov part of the IRF spectrum, and extract the width as a  $\sigma_{IRF} = 73$  ps. This is in substantial agreement with the discussion of the previous section since  $\sigma_{IRF}^2 = \sigma_{stop}^2 + \sigma_{start}^2 + \sigma_{noise}^2$ , where  $\sigma_{start} = 62$  ps,  $\sigma_{noise} = 37$  ps and  $\sigma_{stop} = 18$  ps.

### 8.3.4 Control of the bias fraction

The main advantage of using the available oscilloscope as a digitizer of the pulses for offline analysis is the possibility of extracting multi time stamps. This allows for a multi-hit TDC approach. Thanks to the fact that signals from MCP-PMT are very fast, i.e. completely contained in 1 ns, the dead time is very low and so it is the biased fraction of events. Starting from the considerations previously stated in chapter 6, it is possible to control this fraction by counting the number of pulses per event. Usually the biased fraction is qualitatively controlled by calculating the geometric factor of the setup and by keeping the number of counts well below one per start signal. This was also the approach used in the case of VUV measurement, where no multi hit TDC was available. In the case of the  $\gamma$  setup, also given the low number of counts and the difficulties in collecting a high statistics, it is necessary to keep the rate as high as possible, while still being sure not to introduce significative bias in the measurement. In this setup it is possible to control in real time the number of pulses per event that should follow a Poisson distribution, as shown in figure ?? for a LSO:Ce, Ca crystal. The extraction of the average allows to completely control the bias fraction, and this was done for all the samples measured.

### 8.3.5 Background

In the measurement campaign conducted two separate background processes intervene:

- random coincidences
- direct interaction of a  $\gamma$  in the detector

For what concerns random coincidences they should be kept at a low level, in order not to worsen the uncertainty on the parameter extraction at the fit level. Indeed the important parameter is the signal to noise ratio and this aspect depends strongly on the light yield of the crystal measured, and on the geometry of the system. Nevertheless this kind of event is taken into account in the fit procedure, and in principle the only disadvantage is the necessity for higher statistics to be collected.

The direct interaction of a  $\gamma$  in the detector, on the other hand, could severely bias the measurement, in the time window where the rising edge of the crystal lies. The active area of the MCP is quite large, given the size of the entry window, with a diameter of 11 mm. This makes direct interaction in the detector quite likely. This is easily taken in to account in the case of 511 KeV  $\gamma$ , since they are emitted back to back. In this case it is sufficient to tilt the stop detector with respect to the sample to measure, with an angle of 90 °C.

As previously explained, in addition to the 511 KeV  $\gamma$  photons produced by the annihilation of the positron, the  $^{22}\text{Na}$  de-excite to the  $^{22}\text{Ne}$  ground level by emitting a 1.274 MeV  $\gamma$ . The de-excitation  $\gamma$  is emitted isotropically and can interact in the detector after a gate is open on the start arm, unrelated to any scintillation event in the sample. As shown in ?? this events happen exactly on the rise time of the signal, since the delay introduced by the geometry is negligible. It is not possible to select on a pulse shape basis since the MCP amplitude largely varies, and there is no separable difference between signals coming from a 1.274 MeV event and a photo electron event.

Thus in order to restrict the influence of this events, which become less and less problematic as light yield of the sample measured increase, two approaches are possible:

- screen the detector from the source
- optically delay the scintillation light in order to easily cut spurious events from direct interaction.

The first solution was chosen for time constraints, but the optical delay will be implemented in the future. In particular 5 cm of lead blocks were positioned in between, that allow to stop 95% of the incoming  $\gamma$  photons (density and stopping power taken from Berger (2005)).

## 8.4 Data analysis

Due to time constraints not all the samples measured in VUV could be measured with the  $\gamma$  setup, though the proof of concept was delivered for future completion of the study. The samples measured in the  $\gamma$  setup were

- LYSO 2737
- LGSO
- CTI 2408
- CeF<sub>3</sub>
- LSO Ca Ce
- LuAG

The data extracted were analyzed offline for cuts and time walk correction. The rise time parameter was extracted with the iterative deconvolution algorithm presented in chapter 6, and the error was evaluated as confidence interval on the  $\Delta$ Likelihood.

### 8.4.1 Cuts and background estimation

The IRF measurement was performed at the beginning of the campaign and repeated at regular intervals to correct for eventual drifts, but no significant drift was observed. On the data collected for offline analysis the first cut performed is the photopeak selection on

the start signal, that for the NINO signal happens between 200 and 220 ns, at the 511 KeV peak of the  $^{22}\text{Na}$ .

For the MCP data two set of manipulations were performed: on the amplitude of the MCP to avoid saturation effect and for time walk correction. The MCP signal was cut between 10 and 40 mV, which is the interval that contains the 70% of the pulses collected. At this point the signal was corrected for time walk.

As previously explained, the background can play an important role in the measurement, especially in the case of crystals with low or very low light yield, which is the case of  $\text{CeF}_3$  for example. In order to control this a lead screen was positioned between the source and the MCP to suppress the count rate from direct interaction in the stack. Additionally a quick background measurement was performed, to ensure that the background count rate could be neglected.

#### *8.4.2 Fit procedure*

#### *8.4.3 Results*

#### *8.4.4 Summary*



# **9**

## Conclusions



# Bibliography

- Amaldi, B. (2011), “Present challenges in hadrontherapy techniques,” *The European Physical Journal Plus*, pp. 70–85.
- Anghinolfi, J. e. a. (2004), “NINO: An Ultrafast Low-Power Front-End Amplifier Discriminator for the Time-of-Flight Detector in the ALICE Experiment,” *IEEE Transactions on Nuclear Science*, 51, 1974–1978.
- Bajzer, T. e. a. (1991), “Maximum likelihood method for the analysis of time-resolved fluorescence decay curves,” *European Biophysics Journal*, 20, 247–262.
- Becker (2005), *Advanced Time-Correlated Single Photon Counting Techniques*, Springer.
- Berger, C. e. a. (2005), “Stopping-Power and Range Tables for Electrons, Protons, and Helium Ions,” .
- Crespo, S. e. a. (2007), “Direct time-of-flight for quantitative, real-time in-beam PET: a concept and feasibility study,” *Physics in Medicine and Biology*, pp. 6795–6811.
- Cucciati (2013), “Optimization and Characterization of PET Scanners for Medical Imaging,” Ph.D. thesis, University of Milano-Bicocca.
- Derenzo, W. e. a. (2000), “Measurements of the Intrinsic Rise Times of Common Inorganic Scintillators,” *IEEE Transactions on Nuclear Science*.
- Dolgoshein, F. e. a. (2003), “Silicon photomultiplier and its possible applications,” *Nuclear Instruments and Methods in Physics Research A*, 504, 48–52.
- Durante, L. (2010), “Charged particles in radiation oncology,” *Nature Reviews Clinical Oncology*, pp. 37–43.
- Enghardt, C. e. a. (2004), “Charged hadron tumour therapy monitoring by means of PET,” *Nuclear Instruments Methods in Physics Research A*, pp. 284–288.
- et al., A. (2003), “Geant4 - a Simulation Toolkit,” *Nuclear Instruments and Methods in Physics Research A*, 506, 250–303.
- et al., A. (2009), “LuAG Material for Dual Readout Calorimetry at Future High Energy Physics Accelerators,” *2009 IEEE Nuclear Science Symposium Conference Record*, pp. 2245–2247.

- et al., B. (2013), "Estimation of the Electron Thermalization Length in Ionic Materials," *The Journal of Physical Chemistry Letters*, 4, 3534–3538.
- et al., B. (2014), "Studies on the Cerenkov Effect for Improved Time Resolution of TOF-PET," *IEEE Transactions on Nuclear Science*, 61, 443–447.
- et al., K. (2004a), "Crystal growth and properties of LuAG," *Journal of Crystal Growth*, 260, 159–165.
- et al., M. (2004b), "Effects of Ce concentration on scintillation properties of LaBr<sub>3</sub>:Ce," *Nuclear Science Symposium Conference Record*, pp. 998–1001.
- et al., P. (2012), "Effect of Aspect Ratio on the Light Output of Scintillators," *IEEE Transactions on Nuclear Science*, 59, 2340–2345.
- et al., S. (2002), "Experimental Benchmarks of the Monte Carlo Code Penelope," *Nuclear Instruments and Methods in Physics Research B*, 207, 107–123.
- Ferlay, S. e. a. (2012), *Cancer Incidence and Mortality Worldwide: IARC CancerBase No. 11*, International Agency for Research on Cancer.
- Fiedler, C. e. a. (2006), "The Feasibility of In-Beam PET for Therapeutic Beams of He," *IEEE Transactions in Nuclear Science*, 53, 2252–2260.
- Gentit (2002), "Litran: a General Purpose Monte-Carlo Program Simulating Light Propagation in Isotropic or Anisotropic Media," *Nuclear Instruments and Methods in Physics Research A*, 486, 35–39.
- Gundacker (2014), "Time resolution in scintillator based detectors for positron emission tomography," Ph.D. thesis, Technischen Universitat Wien.
- Hamamatsu (2006), *Photomultiplier Tubes - Basic and Applications*, Hamamatsu.
- Hyman, Schwarcz, S. (1963), "Study of High Speed Photomultiplier Systems," *The Review of Physical Instruments*, 35, 393–406.
- Jellison, S. e. a. (2012), "Spectroscopic Refractive Indices of Monoclinic Single Crystal and Ceramic Lutetium Oxyorthosilicate from 200 to 850 nm," *Journal of Applied Physics*, 112.
- Karp, S. e. a. (2008), "The benefit of time-of-flight in PET imaging: Experimental and clinical results," *Journal of Nuclear Medicine*, 49, 462–470.
- Knoll (2000), *Radiation Detection and Measurement*, Wiley.
- Lecoq, A. e. a. (2006), *Inorganic Scintillators for Detector Systems*, Springer.
- Linz (2012), *Ion Beam Therapy*, Springer.
- Martin, B. e. a. (2001), "Time-Resolved Studies of Scintillation Materials with VUV Harmonic Ultrashort Pulses Laser Source," *IEEE Transactions on Nuclear Science*, 48, 1137–1143.

- Parodi (2004), “On the feasibility of dose quantification with in-beam PET data in radiotherapy with C and proton beams,” Ph.D. thesis, Technischen Universitat Dresden.
- Pizzichemi, D. V. e. a. (2012), “Ray Tracing Simulations in Scintillators: a Comparison between SLitrani and Geant4,” *2012 IEEE Nuclear Science Symposium and Medical Imaging Conference Record (NSS/MIC)*.
- Rodnyi (1997), *Physical Processes in Inorganic Scintillators*, CRC Press.
- Schardt, S. e. a. (2007), “Precision Bragg-Curve Measurements for Light-Ion Beams in Water,” *GSI Scientific Report*.
- Seifert, Schaart, v. D. (2012), “The Lower Bound on the Timing Resolution of Scintillation Detectors,” *Physics in Medicine and Biology*, pp. 1797–1814.
- Shao (2006), “A new timing model for calculating the intrinsic timing resolution of a scintillator detector,” *Physics in Medicine and Biology*, pp. 1103–1117.
- Thompson, A. e. a. (2009), *X-Ray Data Booklet*, Lawrence Berkeley National Laboratory, University of California.
- Vasilv, G. (????), “Multiscale Approach to Estimation of Scintillation Characteristics,” *IEEE Transaction on Nuclear Science*.
- Va’vra (2004), “Ion feedback suppression using inclined MCP holes in a Single-MCP + Micromegas + Pads detector,” *Proceeding of Nuclear Science Symposium Conference Record*, 2, 1142–1146.
- Wilson (1946), “Radiological use of fast protons,” *Radiology*, pp. 487–491.